Part I: 3DPTV: Advances and Error Analysis
Part II: Extension of Guderley's Solution for Converging Shock Waves

Thesis by

Nicolas F. Ponchaut

In Partial Fulfillment of the Requirements

for the Degree of

Doctor of Philosophy

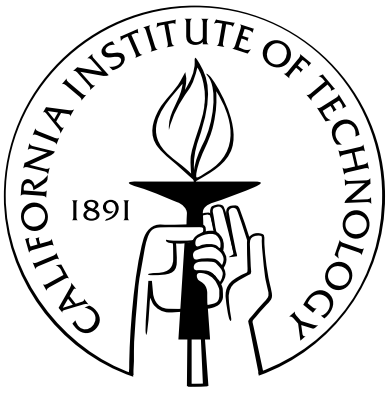

California Institute of Technology

Pasadena, California

2005

(Defended May 31, 2005)

To my parents

Acknowledgements

First, I would like to thank my advisor, Dr. Hans Hornung, for letting me work on this project and helping make it realizable. He has always been an incredible source of knowledge, inspiration, and motivation. His professional advice, availability, and kindness created an incredible work environment to achieve my research goals.

A lot of thanks is also due to Christopher Mouton. The numerous conversations we had, were always very interesting, whether they were about science, politics or society. He was always available and if the English in this thesis is comprehensible, it is for the most part thanks to him. He was a real pleasure to work with and a true friend.

I would also like to thank Bahram Valiferdowsi and Keisuke Fujii. Bahram's knowledge about practical implementations was extremely useful. His kindness and his eternal optimism were big sources of encouragement. Keisuke has always been available, dropping anything to help others.

In addition, I would like to thank Dr. J. Schmisseur from the Air Force Office of Scientific Research for trusting us in the development of the 3-D particle tracking velocimetry setup. Thanks also to Dr. Dana Dabiri for allowing us to use his water tunnel facility at the University of Washington, in Seattle, as well as for his help and advice that led to the publication of the results.

I'm also very appreciative of the numerous suggestions provided by Dr. Dale Pullin on the imploding shock problem. The regular meetings with him helped me to progress in the right direction. I'm also grateful for Dr. Joseph Shepherd's guidance when mentoring was needed.

I acknowledge the members of my committee: Dr. Hans Hornung, Dr. Dale Pullin, Dr. Joseph Shepherd, Dr. Anthony Leonard, and Dr. Tim Colonius, for their time and

assistance in finalizing my thesis.

Finally, and very importantly, I thank my parents for their constant support in all my aspirations; my sisters and my brother for the big laughs we always have and for the continual motivation and strength they provide; my friends, for making my experiences at Caltech enjoyable and memorable; and last but not least, my warmest thanks go to Amel.

أمال، أشكركي جدّاً لحبّكي ولدعمكي المستمر خلال دراستي.

Abstract

This work is divided into two unrelated parts. In the first part, a full three-dimensional particle tracking system was developed and tested. Three images, from three separate CCDs placed at the vertices of an equilateral triangle, permit the three-dimensional location of particles to be determined by triangulation. Particle locations measured at two different times can then be used to create a three-component, three-dimensional velocity field. Key developments are the ability to accurately process overlapping particle images, offset CCDs to significantly improve effective resolution, treatment of dim particle images, and a hybrid particle tracking technique ideal for three-dimensional flows when only two sets of images exist. An in-depth theoretical error analysis was performed, which gives the important sources of error and their effect on the overall system. This error analysis was verified through a series of experiments, and a vortex flow measurement was performed.

In the second part, the problem of a cylindrically or spherically imploding and reflecting shock wave in a flow initially at rest was examined. Guderley's strong shock solution around the origin was improved by adding two more terms in the series expansion solution for both the incoming and the reflected shock waves. A series expansion was also constructed for the case where the shock is still very far from the origin. In addition, a program based on the characteristics method was written. Thanks to an appropriate change of variables, the shock motion could be computed from virtually infinity to very close to the reflection point. Comparisons were made between the series expansions, the characteristics program, and the results obtained using an Euler solver. These comparisons showed that the addition of two terms to the Guderley solution significantly increases the accuracy of the series expansion.

Contents

List of Figures

Part I

3DPTV: Advances and Error Analysis

This part was done jointly with Christopher A. Mouton. The data analysis software was designed by both of us, working in collaboration. My primary focus was the development of the peak searching, the ray tracing, and the particle tracking algorithms whereas Chris took care of the corresponding peak algorithm and of the assembly of the different functions into a big software, usable through a graphical user interface. I also carried out the complete error analysis. Our particular camera was designed by Chris and me, and was constructed and manufactured by Bahram Valiferdowsi. The timing software that allowed for accurate triggering of the CCDs and the lasers was entirely written by Chris. Finally, all the results were taken jointly.

Nomenclature

Roman characters, lower case

d	side length of test volume
d_{C}	distance between CCDs and lens plane
$\boldsymbol{e}_i$	unit vector along the ith ray
k_i	ith calibration constant
r	radius of lens center positions
r_{b_i}	blur radius of particle image i
t_{s}	time separation between frames
x	x-coordinate in camera axes
$\overline{x}$	corrected x-coordinate in CCD space
x_i	x-coordinate of particle image i in CCD space (expressed in pixels)
y	y-coordinate in camera axes
$\overline{y}$	corrected y-coordinate in CCD space
y_i	y-coordinate of particle image i in CCD space (expressed in pixels)
z	z-coordinate (along camera axis)

Roman characters, upper case

A_i	intensity amplitude of particle image i
B_i	calibration constant
E_{r}	estimation of particle position error
$\boldsymbol{I}$	identity matrix
$\boldsymbol{I}_i$	coordinates of a particle image on the CCD i (expressed in pixels)
L	distance from camera to target

$\boldsymbol{M}_i$	matrix used to obtain the ith particle position
N	number of particle images
$\boldsymbol{P}_i^0$	coordinates of a point on the ith ray
$\boldsymbol{P}_i^{\mathrm{C}}$	position of target plane center image on CCD i
$\boldsymbol{P}_i^{\mathrm{l}}$	position of the ith lens
$\boldsymbol{P}^{\mathrm{P}}$	particle position
S	square pixel side length
$\boldsymbol{U}$	velocity vector
X_0	x-coordinate of the lens optical center projection on a CCD
Y_0	y-coordinate of the lens optical center projection on a CCD

Greek characters

$\Delta\boldsymbol{U}$	error on velocity
$\langle\epsilon\rangle_{90}$	90% confidence interval of peak searching accuracy
λ_i	parametric coordinate on ray i

Superscripts

C	relative to CCDs
c	relative to calibration
l	relative to lenses
P	relative to particle position
p	relative to peak searching

Introduction

The ability to accurately map fluid velocity fields in three dimensions would provide researchers with a much greater understanding of a wide variety of flows. A particularly promising technique for velocity measurements is particle velocimetry. With this technique, images of particles are taken at different times, and based on their displacements and the time separation, the velocity of these particles can be calculated. Unfortunately, three-component three-dimensional velocimetry systems have lagged substantially behind their two-dimensional counterparts. To remedy this situation, some researchers have developed methods using a single charged coupled device (CCD) [1] or several CCDs (generally three or four) using either the epipolar technique [2, 3, 4, 5] or ray tracing [6, 7] for finding corresponding peaks of intensity in particle images. Others are using a holographic system, which although complicated, appears promising [8, 9]. Of particular interest is the work done by Pereira *et al.* [3, 10] in developing a digital defocusing particle image velocimetry (DDPIV) system. Their system uses three individual CCDs placed at the vertices of an equilateral triangle, with all three CCDs having overlapping fields of view. The test section can be placed anywhere in this overlap region. An image of every particle in the test section is projected onto each CCD. When the CCD images are overlayed, the three images of a particle will be located at the three corners of an equilateral triangle. One thing that sets DDPIV apart from many other techniques is that the entire camera system is encased in a single unit and can therefore be moved from facility to facility without any need for realignment or recalibration. The DDPIV system uses the size and position of the image triangle to determine the three-dimensional position of the corresponding particle. Subpixel accuracy of a particle image location is obtained by having the particle image span more than one pixel. With subpixel accuracy the overall resolution of the system is drastically

improved.

In the present work, we first revisited the design choices made by Pereira *et al.* and then improved upon some of them. Also, a new and robust software package was developed. The software that will be described is significantly different and improved from that of Pereira *et al.*, and is discussed in detail in Chapter 2. In particular, a ray tracing rather than a defocusing algorithm is implemented in order to find the three-dimensional position of the particles. These improvements provide increased accuracy of results. Furthermore, while Pereira *et al.* used a three-dimensional correlation over voxels, we pursue direct particle tracking using a hybrid technique. The system developed is referred to as three-dimensional particle triangulation velocimetry (3DPTV) [5, 11].

It is essential for any experiment to have an estimate of the errors that can arise from the system, both from the hardware and from the software. This work will present both theoretically and experimentally the errors one can expect when using 3DPTV, in Chapters 3 and 4. First, a thorough theoretical error analysis will be performed, followed by a comparison of these error estimates with experimental results.

Lastly, in Chapter 4, are the results of experimental measurements of a sonic jet, and of the flow around a delta wing at an angle of attack. The results show the ability of the 3DPTV system to make measurements of interesting flows with a relatively large range of velocities.

Chapter 1

Principle

Both the hardware setup of Pereira *et al.* [3, 10] for DDPIV and the hardware setup of 3DPTV consist of a camera comprising three separate CCDs, which all view the same test volume from different angles. The front plate of the camera consists of a mask, three lenses, and three apertures. Behind each lens-aperture combination, there is a CCD. The need for more than two CCDs and the suggestion that with three cameras, an equilateral triangle is the optimum configuration, is discussed by Maas *et al.* [2]. The setup of Pereira *et al.* is such that the center of a target plate is projected onto the center of each CCD. Figure 1.1 shows this for one of the CCDs. In this arrangement, the image of the test volume does not fill the frame of the CCD; this is clearly sub-optimal. In order to make full use of all the pixels of the CCD, 3DPTV uses offsets, in which the CCDs are moved away from the lens and away from the camera axis as shown in Figure 1.1. Since, with these offsets, the image of the test volume covers more pixels, the system will have higher overall accuracy and improved resolution.

The purpose of the lens is to give an acceptable range of particle image blur; therefore, different focal lengths are used for the offset and no offset configurations. Since 3DPTV does not rely on the defocusing principle, the restriction that the target plane be in focus, as with DDPIV [3, 10], is not required.

It is important to note that the lens is not parallel to the target plane or to the CCDs. The reason for that is to avoid lens aberrations as much as possible. Future camera designs should have the lens axis intersect the center of the test volume to further reduce coma aberration in the test volume.

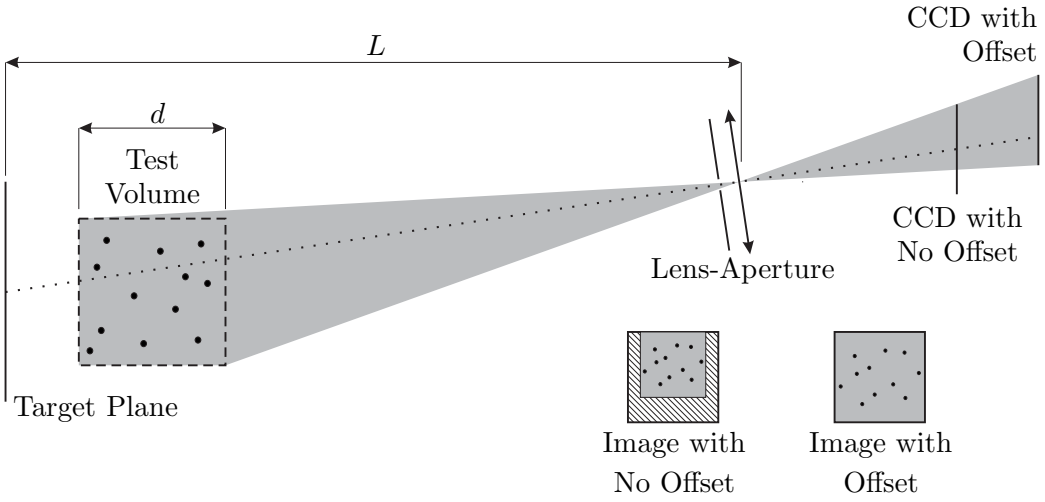

Figure 1.1: Maximum CCD utilization using offsets. The dashed out area of the CCD image with no offset shows the area of the CCD not utilized.

In practice it is impossible to place the CCDs at their exact theoretical locations; therefore, careful alignment followed by calibration is required. In order to do this, a well designed target is needed in addition to calibration software. Therefore, a target with 100 equally spaced dots per square inch was designed. With this target placed at the target plane, the CCDs should be aligned as carefully as possible. The calibration software, discussed further in Section 2.3, then compares the measured and known dot locations and creates a mapping to correct for errors in CCD placement as well as for lens aberrations and other effects. The benefits of this calibration technique is the simplicity and speed at which an accurate calibration can be made.

Once the camera has been aligned and calibrated, the images of a particle in the test volume will appear at the vertices of an equilateral triangle on the overlayed CCD images. The formation of triangles on the overlayed images is shown in Figure 1.2. It is only a matter of ray tracing, as discussed in Section 2.4, to transform a triangle on the CCDs to a particle location.

Particle tracking is done using a hybrid technique. Once all of the three-dimensional positions are known, all that is required to determine the three components of the velocity of the particles is to find corresponding particles in two successive frames separated by a known time interval. This is discussed in detail in Section 2.6. The remainder of this section will present the geometry of the 3DPTV system and the current camera system.

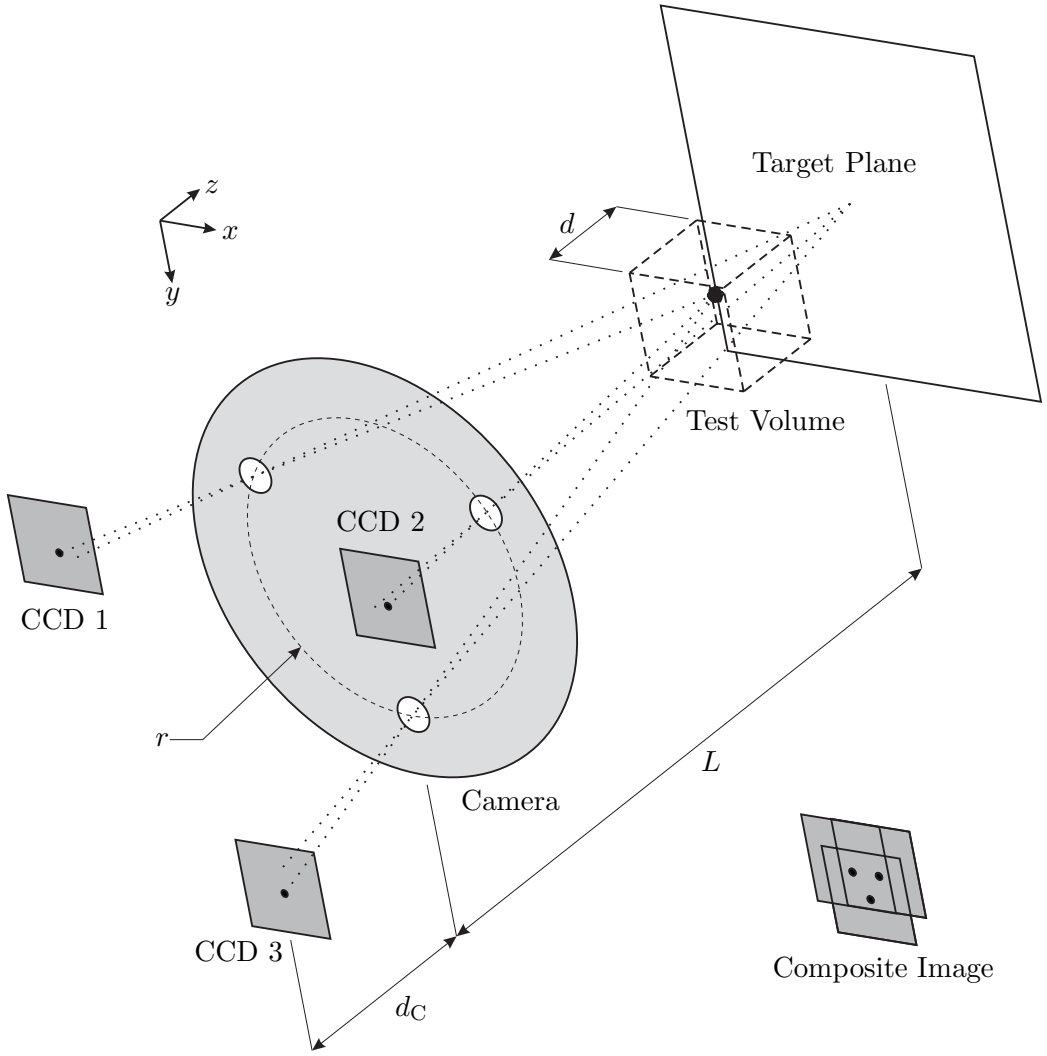

Figure 1.2: Projection of a particle onto the CCDs. The composite image is formed by overlaying the CCD images with correct offsets. The origin of the coordinates is at the centroid of the three lenses.

1.1 3DPTV Geometric Description

The design of the 3DPTV system involves many related parameters. Choosing the best parameters for a set of particular requirements is truly a design exercise. That is to say, there is no objective function that has to be maximized and compromises have to be made between accuracy, test volume size and external size of the system, while satisfying numerous practical constraints. The governing equations used in this design are presented in this section.

1.1.1 Alignment

As explained before, the camera is composed of three CCDs placed at the vertices of an equilateral triangle. The distance between the CCDs and the plane of the lenses, d_{C}, and placement of each CCD are chosen so that the projection of the test volume fills the entire CCD. Let the coordinates of the projection of the center of the target plane onto the ith CCD be $\boldsymbol{P}_i^{\mathrm{C}}$. Each of the CCDs views the test volume through its own lens, which is located at $\boldsymbol{P}_i^{\mathrm{l}}$. Note that the focal length of the lenses does not enter into any equations presented in this paper and there is no constraint requiring that the target plane be in focus. The focal length of the lenses will only change the degree to which particle images are blurred on the CCDs and therefore should be chosen so that images of particles within the test volume appear on the CCDs with an acceptable range of blur radii. Three-dimensional vector positions $\boldsymbol{P}$ are measured with respect to the geometric center of the three lenses.

One possible lens configuration is

$$\boldsymbol{P}_1^{\mathrm{l}} = (0, r, 0)\,, \tag{1.1}$$

$$\boldsymbol{P}_2^{\mathrm{l}} = \left(\frac{\sqrt{3}\,r}{2}, \frac{-r}{2}, 0\right), \tag{1.2}$$

$$\boldsymbol{P}_3^{\mathrm{l}} = \left(-\frac{\sqrt{3}\,r}{2}, \frac{-r}{2}, 0\right), \tag{1.3}$$

where r is the radius of the circle on which the centers of the lenses lie. If the camera is perfectly aligned, the position of the projections of the target plane center onto the CCDs

for this lens configuration will be

$$\boldsymbol{P}_1^{\mathrm{C}} = \left(0, \frac{r}{L}\left(L + d_{\mathrm{C}}\right), -d_{\mathrm{C}}\right), \tag{1.4}$$

$$\boldsymbol{P}_2^{\mathrm{C}} = \left(\frac{\sqrt{3}}{2L}\left(L + d_{\mathrm{C}}\right), -\frac{r}{2L}\left(L + d_{\mathrm{C}}\right), -d_{\mathrm{C}}\right), \tag{1.5}$$

$$\boldsymbol{P}_3^{\mathrm{C}} = \left(-\frac{\sqrt{3}}{2L}\left(L + d_{\mathrm{C}}\right), -\frac{r}{2L}\left(L + d_{\mathrm{C}}\right), -d_{\mathrm{C}}\right). \tag{1.6}$$

1.1.2 2-D Projections

Suppose that a particle is at position (x, y, z) with respect to the geometric center of the three lenses. Using geometric optics it is possible to find the pixel coordinates, $\boldsymbol{I}_i$, of the particle image on CCD i, given $\boldsymbol{P}^{\mathrm{l}}$ and $\boldsymbol{P}^{\mathrm{c}}$:

$$\boldsymbol{I}_1 = \left(-\frac{x}{Sz}d_{\mathrm{C}}, \frac{r\left(L - z\right) - Ly}{SzL}d_{\mathrm{C}}\right), \tag{1.7}$$

$$\boldsymbol{I}_2 = \left(\frac{-2Lx + \sqrt{3}\,r\left(L - z\right)}{2SzL}d_{\mathrm{C}}, \frac{-r\left(L - z\right) - 2Ly}{2SzL}d_{\mathrm{C}}\right), \tag{1.8}$$

$$\boldsymbol{I}_3 = \left(\frac{-2Lx - \sqrt{3}\,r\left(L - z\right)}{2SzL}d_{\mathrm{C}}, \frac{-r\left(L - z\right) - 2Ly}{2SzL}d_{\mathrm{C}}\right), \tag{1.9}$$

where S is the side length of a square pixel. $\boldsymbol{I}$ is measured in pixels in the plane of each individual CCD with respect to the point where the center of the target plane is projected onto the respective CCD. Using these coordinates, the side length, s, of the equilateral triangle formed by corresponding particle images on the overlayed CCD images is given by

$$s = \frac{\sqrt{3}\,r\left(L - z\right)}{SzL}d_{\mathrm{C}}. \tag{1.10}$$

1.1.3 CCD Offsets

Offsetting the CCDs significantly improves the accuracy of the 3DPTV system. The increase in the useful area can be calculated by looking at the additional area covered in the offset

configuration, as seen in Figure 1.1. This calculation will produce a ratio of useful CCD surface area between the system with and without offsets that is given by

$$\frac{s_{\text{offset}}}{s_{\text{no offset}}} = \left(\frac{2\left(Ld + 2r(L-z)\right)(d+z)}{Ld\left(d+2(r+z)\right)} \right)^2 . \tag{1.11}$$

This formula supposes that the test volume is a cube with side-length d and it assumes a limited range of values for r, d, L and z. For other value ranges similar formulas can be found. Note that by offsetting the CCDs, the projection of the center of the target plane onto the CCDs no longer corresponds to the middle pixels, as is seen in Figure 1.2. Clearly, this increased useful area will result in an improved accuracy over that without offsets.

1.2 Current Camera Configuration

The camera used in the experiments is designed to investigate a $50 \times 50 \times 50$ mm^3 test volume. Each sensor is composed of 1024×1024 px, each pixel is square with a side length of 6.45 μm. Three lenses are placed at the corners of an equilateral triangle inscribed in a circle of radius of 42.5 mm. The target plate used for alignment was placed 625 mm from the camera. The z-range of the test volume is 517 mm to 567 mm from the camera. Equation 1.11 shows that because of offsets there is a 58% increase in the number of pixels used relative to the setup without the offsets.

Chapter 2

Data Processing Program

The data processing program was written to convert a set of three images into 3-D positions and, when required, to compute a velocity field from these results. To achieve this, several computational routines are performed. First, the images are preprocessed to remove noise. Next, a peak searching algorithm looks for peaks in each image by performing a least-squares curve fit. This least-squares fitting allows for both overlapping particle images and sub-pixel accuracy. Once the peaks in each image have been found, an epipolar search is employed to find corresponding peaks. The locations of the peaks are then used to calculate the three-dimensional particle position by ray tracing, whereas DDPIV uses the defocusing principle [3, 10]. With particle positions known in two successive frames, particle tracking can be performed.

2.1 Image Pre-Processing

The images have both systematic noise, that is to say noise at specific spatial frequencies, and random noise. To remove the systematic noise, the images are Fourier transformed, spatial frequencies of noise inherent to the camera system are removed, after which an inverse Fourier transform is performed. From this point on, the images are stored as a matrix of double precision numbers so that minimum additional discretization error is introduced. In order to remove random noise, a smoothing filter Gaussian blurs the images. By performing a Gaussian blur a particle image with a Gaussian distribution will remain Gaussian, whereas the random noise will be reduced. Because of the details of the current 3DPTV

program the additional Gaussian blur reduces the error associated with the algorithm; this is discussed further in Section 2.2.

2.2 Peak Search

The two most critical parts of the 3DPTV program are the peak search, which finds the location of each particle image, and the calibration subroutines. In fact, since they are the only two subroutines that deal with actual images and noise, the accuracy of the results depends on the robustness of these two subroutines. Searching for peaks can be very time-consuming when the particle density is high. Because of the computation time and importance of this subroutine, it must be both robust and efficient.

When investigating a three-dimensional volume, the total number of illuminated particles should be high. However, as more particles are introduced into the volume, finding individual particles becomes increasingly difficult, especially when the particle images are blurred. Three possible solutions to this problem are listed here. All three involve surface fitting of a function in order to obtain sub-pixel accuracy. One solution to this problem is to reduce the total number of particles to a point where virtually no particle images overlap, in which case all that is required is to find all the local maxima and fit a single surface around each maximum. This solution gives excellent image location accuracy, but produces only a small number of particle images. A second solution is to have a relatively high number of particles, while still just finding local maxima and fitting a single surface around each maximum. This solution essentially ignores particle image overlapping and therefore results in some particles being located with excellent accuracy, while others are located with virtually no accuracy; however, this provides for a larger number of total particle images than the first solution. The third solution, which is implemented here, is to have a relatively high number of particles, but not to rely on local maxima. This solution calls for a least-squares optimization of a number of surfaces and provides very good accuracy for a large number of particles. The reason that a least-squares optimization is the best solution is that when the particle density is high, two distinct particle images often overlap. In this case, two particle images do not necessarily create two local maxima and the local maximum that is formed

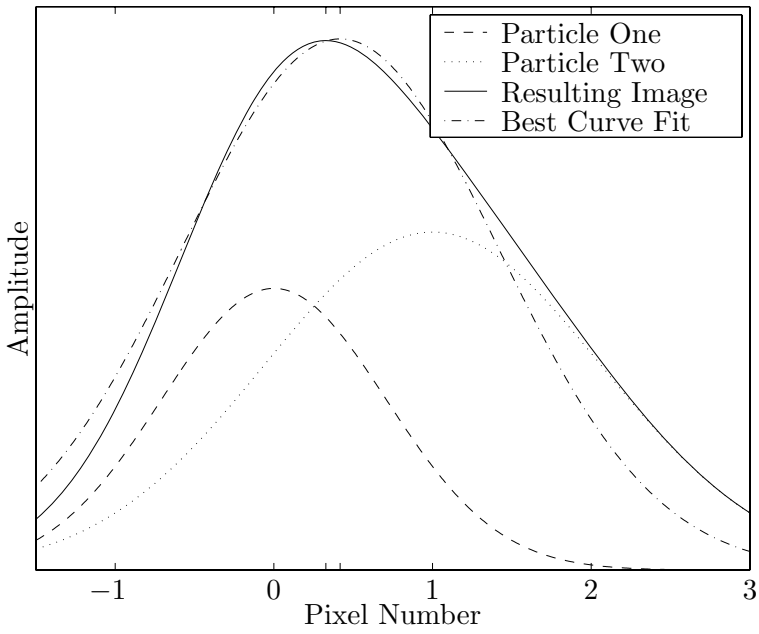

Figure 2.1: Overlapping particles.

is not, in general, at a particle position. The example in Figure 2.1 shows that using local maxima as a criterion, as in the second solution, will often produce very inaccurate results. In the figure, one particle is centered at 0 px and one at 1 px, while the best Gaussian curve fit is centered at 0.42 px. This clearly shows that when particle images overlap, the number of local maxima is not the number of particles and that the position of a local maximum is not directly related to particle positions.

From this discussion, we see that we cannot draw many conclusions from the number of local maxima. For the purposes of the current theoretical and experimental results, a Gaussian intensity distribution is used. If there are N particle images, the intensity distribution on the CCD, A_t, is

$$A_\mathrm{t}(x,y) = \sum_{i=1}^{N} A_i \, F(\bar{r}) \,, \tag{2.1}$$

where

$$\bar{r}^2 = \frac{(x-x_i)^2 + (y-y_i)^2}{r_{\mathrm{b}_i}^2}. \tag{2.2}$$

In this expression, A_i and (x_i, y_i) are the intensity maximum and the center position of the

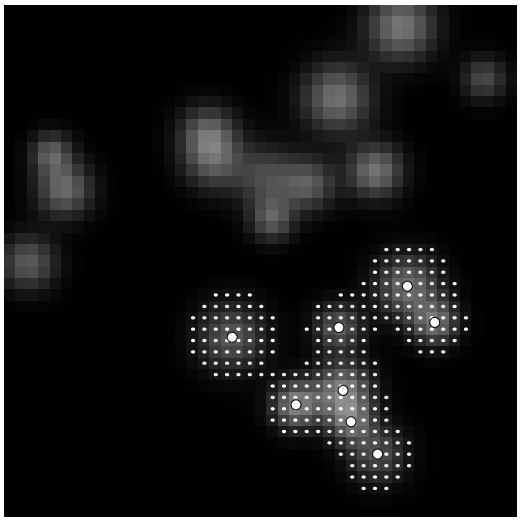

Figure 2.2: Blob selection. The white dots represent the blob pixels and the white dots with black circles show the centers of the particle images.

ith particle image on the CCD, respectively. The blur radius, r_{b_i}, is defined as the radius at which the intensity reaches 10% of its maximum value. In experiments, the intensity distribution is known and all the variables subscripted with i are unknown. This forms a system of size $4N$ that needs to be solved, with N also being unknown. Typically, N is on the order of 10,000, which gives about 40,000 variables to solve for simultaneously, while solving for N itself. The purpose of the peak search algorithm is to solve for N, x_i, y_i, A_i, and r_{b_i}, where, for most applications, x_i, y_i, and N are the variables of interest. By adopting this method, the particle image positions of two or more overlapping particle images can be calculated, whereas solution two would simply find one incorrect particle image position.

Since, in fact, real particle images do not have an exact Gaussian intensity distribution, the fitting function, $F(\bar{r})$, can easily be changed from a Gaussian to a more complicated function. However, for most applications simply using a Gaussian function is sufficient since particle images are near Gaussian.

To increase the speed of the program, the problem is split into a set of uncoupled smaller problems. To do that, the concept of a blob is introduced. In this thesis, a blob is defined as the set of all pixels that have an intensity level higher than a given threshold and that

are connected (*i.e.*, are neighbors). If this threshold is sufficiently small, blobs can be considered as separate problems (*i.e.*, particles in one blob do not influence the intensity of other blobs). The concept of a blob is illustrated by example in Figure 2.2. In this figure, all the pixels marked with a white dot belong to the same blob, and the white dots with black circles correspond to particle image locations. The definition of a blob used here varies from that used by Stüer *et al.* [12] and Kieft *et al.* [4] in the fact that the current authors allow a blob to contain more than one particle image. Maas *et al.* [2] allow for multiple particle images in a blob; however, the method they use to find the particle image centers is significantly different.

Inside each blob, the program tries to find the exact number and the position of the particle images. For a given blob, there are N_b particle images, for which the initial guess is based on the number of local maxima above a certain threshold, N_m, and the position of these local maxima. It is clear that if the noise has a relatively small amplitude, $N_\mathrm{m} \leq N_\mathrm{b}$. The program was written so that the guessed number of particles, N_g, can only increase, if needed, to reach N_b. Therefore, the subroutine must ensure that the guessed number of particles never becomes higher than N_b (*i.e.*, $N_\mathrm{m} \leq N_\mathrm{g} \leq N_\mathrm{b}$).

Particles are added if the least-squares surface fit of the sum of N_g surfaces leads to relatively large errors. A particle is added where the error is a local maximum. However, to keep $N_\mathrm{m} \leq N_\mathrm{b}$, two particles cannot be added at the same iteration if they are closer than a given distance, usually three times the maximum blur radius.

Because it is so critical to ensure that the number of local maxima is indeed below the number of true particle images in a given blob, it is important to remove local maxima associated with noise. To do this, a Gaussian blur is applied during the image pre-processing. The Gaussian blur is useful because local maxima due to noise are leveled out, while Gaussian image distributions remain Gaussian.

To further decrease the processing time for large particle image densities, large blobs are split into smaller overlapping ones. The purpose of this splitting is not to isolate individual particle images, but rather to decouple the problem into a set of smaller problems. Therefore, this splitting is unrelated to the blob splitting of Maas *et al.* [2]. To avoid

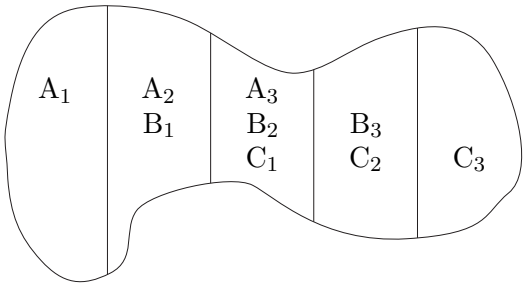

Figure 2.3: Blob splitting to minimize calculation time. This blob is split into three overlapping parts (A, B, and C). In part A, only the results from subparts 1 and 2 are kept; in B, only the results in 2 are kept; and in C, only the results in 2 and 3 are kept. This method splits the problem into three subproblems that are smaller than the original one. Note that the splitting on this figure is done only in one direction; it can also be done in the other direction or in both at the same time.

inaccuracies due to cropped data, only the particle images that are found in the center part of the split blobs are recorded as explained in Figure 2.3. The split blobs are overlapped in such a way as to ensure that their center parts will cover the entire blob.

To increase the computation speed even further, regions of a blob where the error is very low are locked and only the other regions of the blob where the error is still important are recalculated. Again, a minimum distance is used; that is to say, the error surrounding a particle must not only be low at the particle location but also low within this given minimum distance.

2.3 Calibration

The calibration process is a very important part of the program, as it drastically reduces the errors in the measurements. All the relations that were derived in previous sections assume that the camera is exactly aligned. For example, for the alignment error to be of the same order as the error associated with peak searching, each CCD, in our current camera configuration and without calibration, would have to have pitch and yaw angles of $0°\pm0.5°$, a roll angle of $0°\pm0.0025°$, and a position in z and in x, y that is accurate within $1\,\mu$m and 100 nm, respectively. This accuracy is not feasible in practice. Furthermore, the lens aberrations create errors that are 100 times larger than the errors in peak searching. For all these reasons, a calibration correction is essential.

The concept of the calibration is that using a target placed at a well-known position, a mapping from the actual CCD locations to virtual CCD locations can be created. Since the positions of all the dots on the target are assumed to be exactly known, the exact image positions on the virtual CCDs can be computed using ray tracing with theoretical lens and CCD locations. By identifying all the dots on the real CCDs, a mapping is created from each real CCD to each virtual CCD.

Typically, the target is a flat plate containing a grid of more than 500 dots. The mapping is created by fitting functions of several variables. These functions are chosen to be able to represent any kind of rotation and translation, and to correct for the main errors that appear due to lens aberrations.

For the camera misalignment, three possible rotations and three possible displacements have to be corrected. Only six variables are therefore needed [13, 6]; however, it is much easier to compute the calibration mapping by introducing 2 additional non-physical fitting parameters. The six variable mapping function [13, 6] can then be written as

$$X = \frac{B_1 + B_2 x + B_3 y}{1 + B_7 x + B_8 y}, \tag{2.3}$$

$$Y = \frac{B_4 + B_5 x + B_6 y}{1 + B_7 x + B_8 y}, \tag{2.4}$$

where X, Y denote the mapped location, and x, y the actual locations. Note that the individual coefficients are not directly related to those of the previous authors [13, 6]. In addition to this, radial distortion is assumed due to lens aberrations. Two additional constants (X_0 and Y_0), not related to B_1 through B_8, are introduced to locate the projection of the optical center of the lens onto the CCD, and six to create a mapping based on radius (k_i). The corrected locations finally become

$$\overline{x} = X + (X - X_0) \sum_{i=1}^{6} k_i R^i, \tag{2.5}$$

$$\overline{y} = Y + (Y - Y_0) \sum_{i=1}^{6} k_i R^i, \tag{2.6}$$

where $\overline{x}$ and $\overline{y}$ are the final corrected values on the virtual CCD and where

$$R = \sqrt{(X - X_0)^2 + (Y - Y_0)^2}. \tag{2.7}$$

Similar mapping functions have been used by other researchers [13, 6].

2.4 Epipolar Search and Ray Tracing

The three CCDs are equally spaced along the circumference of a circle and view the same volume. This means that one particle is projected onto a different location on each of the CCDs, since each CCD images the particle from a different location. If the three CCD images are overlayed, as shown in Figure 1.2, the three particle images will form the corners of a near-equilateral triangle [3, 10]. Complications will clearly arise when the image contains many thousands of particles, and it is no longer obvious which three peaks correspond to a specific particle. In order to find these corresponding peaks, a search algorithm using epipolar lines is employed [2, 3, 4], then ray tracing is used to find the point of closest intersection of the three rays and the RMS distance from the rays to this point. Consider a ray originating from the ith CCD, which is given by $\boldsymbol{P}_i = \boldsymbol{P}_i^0 + \lambda_i \boldsymbol{e}_i$, where $\boldsymbol{P}_i^0$ is the center of the ith lens, $\boldsymbol{e}_i$ is the unit vector pointing from the particle image to the lens center of the ith CCD, and λ_i is a scalar. The estimated position, $\boldsymbol{P}^{\mathrm{p}}$, of the particle is given by minimizing the function

$$\sum_{i=1}^{3} \left(\boldsymbol{P}_i - \boldsymbol{P}^{\mathrm{p}}\right)^2 \tag{2.8}$$

over all possible λ_i, which gives an optimum $\lambda_i = \left(\boldsymbol{P}^{\mathrm{p}} - \boldsymbol{P}_i^0\right) \cdot \boldsymbol{e}_i$. The RMS error, E_{r}, associated with this λ_i and the three rays is

$$E_{\mathrm{r}}^2 = \frac{1}{3} \sum_{i=1}^{3} \left\{ \left(\boldsymbol{P}^{\mathrm{p}} - \boldsymbol{P}_i^0\right)^2 - \left(\left(\boldsymbol{P}^{\mathrm{p}} - \boldsymbol{P}_i^0\right) \cdot \boldsymbol{e}_i\right)^2 \right\}. \tag{2.9}$$

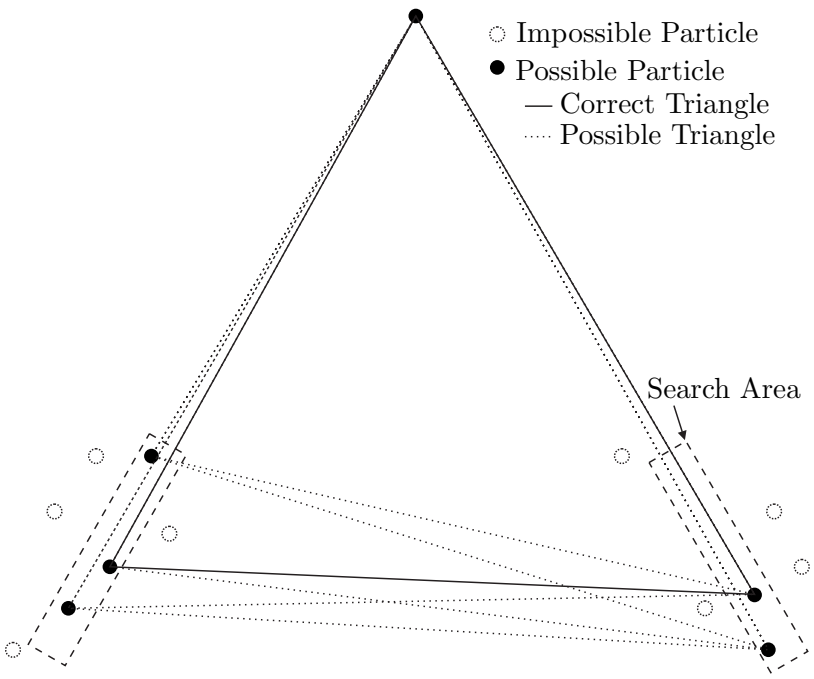

Figure 2.4: Triangle formation by searching on epipolar lines. Selecting a particle image on the first CCD, possible corresponding particle images are selected on the other two CCDs by defining search areas. Among all the possible triangles that can then be found with the selected particle images, the only one that is kept is the one leading to the minimum error as defined by Equation 2.9.

Minimizing the error with respect to the particle position, $\boldsymbol{P}^{\mathrm{P}}$, produces a linear system,

$$\left(\sum_{i=1}^{3} \boldsymbol{M}_i\right) \boldsymbol{P}^{\mathrm{P}} = \left(\sum_{i=1}^{3} \boldsymbol{M}_i \boldsymbol{P}_i^0\right), \tag{2.10}$$

where

$$\boldsymbol{M}_i = \boldsymbol{e}_i \otimes \boldsymbol{e}_i - \boldsymbol{I}, \tag{2.11}$$

$\boldsymbol{I}$ being the identity matrix and the symbol $\otimes$ representing the outer product. The point of closest intersection of the three rays, $\boldsymbol{P}^{\mathrm{P}}$, can then easily be solved for. Substituting this point back into equation 2.9 gives the error associated with the three rays.

Since any one particle image may have multiple possible corresponding particle images, the combination that has the lowest RMS error, *i.e.*, the one for which the three rays come closest to intersecting, is considered the correct one. In addition, no particle image may be part of more than one set of corresponding particle images. The process is shown in

Figure 2.4.

If different media are involved, the rays are traced toward the test volume and are deflected each time the refractive index changes. Equations 2.8 to 2.10 are still valid provided that $\boldsymbol{e}_i$ is the direction of the ray in the test volume and $\boldsymbol{P}_i^0$ is the position of one of the points of the ray in the test volume.

2.5 Peak Level

A key enhancement of the system is the ability to include hard-to-detect particle images. These are images that are so weak that the signal-to-noise ratio of the particle image intensity is close to one. Rather than ignoring these peaks, as they may indeed correspond to particles, they are recorded as weak peaks. Peaks that are above the given threshold are simply recorded as strong peaks. A peak may also be recorded as a weak peak if the blob to which it belongs is very crowded. Because weak peaks may not correspond to real particles, they may only belong to an equilateral triangle whose other vertices are formed by strong peaks. Since the sub-pixel accuracy of weak peaks is in general much less than that of a strong peak, they are not considered when converting from triangles to 3-D positions. In this case, the particle location is simply the point of closest intersection of the rays emanating from the two strong peaks.

2.6 Particle Tracking

The DDPIV technique developed by Pereira *et al.* [3, 10] performs 3-D cross correlations on interrogation voxels in order to construct the velocity field. This technique was not chosen for two reasons. The primary reason is that the density of particles is very low in 3-D, even with 8,000 particles in the test volume, very large correlation volumes would be required. To illustrate this, in 2-D, 8,000 particles would represent about 90 particles in each direction; whereas in 3-D, they represent only 20 particles in each direction. In addition, PIV produces an average velocity in interrogation regions; therefore, flow features can be lost in regions of high velocity gradients. This and other benefits of PTV are discussed by Kim *et al.*

[14]. One of the general limitations of PTV is that it requires accurately locating individual particle images; however, in 3DPTV this does not present any additional problems since these particle image locations must be computed in order to find the three-dimensional particle positions.

In the current data processing program, the final velocity field is constructed using a particle tracking method. Since only one set of particle pairs is considered, trajectories cannot be used to help find corresponding pairs as is done by Malik *et al.* [15], Stüer *et al.* [12], and Willneff [16]. The current particle tracking algorithm uses a hybrid process similar to the two-dimensional process used by Kim *et al.* [14]. First, a rough velocity field is built using a 3-D correlation. The domain is divided into small correlation voxels that overlap. The correlation voxel from one frame is offset by the local displacement in the second frame. The resulting vector is the one that gives the best correlation between the original correlation box and the offset box. At the same time, simple direct particle tracking is performed for particles that have only one possible corresponding particle in the other frame. A weighted average between the correlation and the simple direct particle tracking is then evaluated. Appropriate weights are assigned to all the vectors so that the correlation approach has more influence where it is more accurate (*i.e.*, where the particle density is high) and the simple particle tracking has more influence where the density is low. This hybrid approach is only used to form a first guess of the actual velocity field. Using this average field as a first guess, a complete particle tracking is performed. The program iterates the velocity field several times. In each iteration bad vectors are suppressed and good ones are added. Specifically, a vector is considered good if it is within a certain number of standard deviations of the surrounding vectors. If it is outside this range, the vector is considered bad. It is important to note that the final velocity field is formed only by particle tracking.

Chapter 3

Theoretical Error Analysis

Without a thorough understanding of the errors associated with 3DPTV, the results have very little meaning. Because of this, a detailed error analysis was performed, both theoretically and experimentally. The error can be broken up into two uncorrelated parts. The first part is the error due to inaccuracies in calibration and in construction. The second part is the error due to the fact that peak searching is performed on discretized images. In this section the theoretical error analysis is presented. All calculations have been done assuming that the measurements have a Gaussian distribution. Note that the errors are estimated using a 90% confidence limit. The 90% confidence limit of g is denoted $\langle g \rangle_{90}$. Specifically for a sample with average γ, 90% of the observations will be within the interval $[\gamma - \langle g \rangle_{90}, \gamma + \langle g \rangle_{90}]$.

3.1 Calibration Error

As discussed earlier, calibration is a key step in 3DPTV. Without calibration the CCDs must be placed with an unattainable accuracy. Of course, the calibration is not exact either. Errors in calibration arise from several sources. These include residual lens aberrations and the imperfect placement of the test target. There are also errors due to imprecision in the placement of the lenses. Since these errors cannot be measured, it is not necessary to derive the exact effect of these errors on velocity measurements. Rather, it is useful to understand the form of the measurement errors.

The errors in calibration will produce errors in the position of a particle, ΔP_i^c. We can

then write the errors in velocities due to calibration errors as

$$\Delta U_i^{\mathrm{c}} = \frac{\partial \Delta P_i^{\mathrm{c}}}{\partial x} U_x + \frac{\partial \Delta P_i^{\mathrm{c}}}{\partial y} U_y + \frac{\partial \Delta P_i^{\mathrm{c}}}{\partial z} U_z, \tag{3.1}$$

where i is either x, y, or z. This can be written more simply as

$$\Delta U_i^{\mathrm{c}} = |U|\, F_i \left(\frac{U_x}{U_z}, \frac{U_y}{U_z}, x, y, z, \Lambda \right), \tag{3.2}$$

where Λ is the set of all parameters that describe the camera and the calibration setup. F_i is a dimensionless function that describes the effect of the imprecisions of the camera construction and of the calibration setup on the measured velocities. It is important to note that the error on measured velocities is proportional to the magnitude of velocity.

In order to compare with experiments, which were done using a plate in the x–y plane, the error, ΔU_i^{c}, is integrated over a x–y plane in the test volume to form the plate-averaged error, $\overline{\Delta U_i^{\mathrm{c}}}$. The bar denotes a plate-averaged value defined as

$$\overline{g} = \frac{1}{d^2} \int_{-d/2}^{d/2} \int_{-d/2}^{d/2} g \, dx \, dy \,, \tag{3.3}$$

where d is the side length of the test volume. The experiments were done by translating a plate. This means that the velocities were the same for all points on the plate. We can therefore write the plate-averaged error, $\overline{\Delta U_i^{\mathrm{c}}}$, as

$$\mu_i^{\mathrm{c}} = \overline{\Delta U_i^{\mathrm{c}}} = |\boldsymbol{U}|\, \overline{F_i} \left(\frac{U_x}{U_z}, \frac{U_y}{U_z}, d, z, \Lambda \right). \tag{3.4}$$

Since F_i is a function of x and y, we can measure the amount that individual points vary from the plate-averaged value, $\left(\Delta U_i^{\mathrm{c}} - \overline{\Delta U_i^{\mathrm{c}}}\right)$. We then define σ_i^{c} to be the range in which 90% of the variances fall. From the definition of σ_i^{c}, we see that it will also be proportional to $|\boldsymbol{U}|$.

3.2 Peak Searching Error

A 2-D error analysis for DDPIV was done by Pereira *et al.* [3, 10]; however, since their analysis is only two-dimensional it cannot be applied directly to the actual three-dimensional system. Pereira *et al.* [10] begin their error analysis by considering an error in particle placement and its effect on the images. Because of this difference, the results of the current error analysis are significantly different from those of Pereira *et al.*.

We consider here the three-dimensionality of the system and accurately analyze the errors caused by the peak searching algorithm. To start with, the peak searching algorithm has a limited accuracy with which it can find the centroid of a blurred particle. This causes an error in the image position. The 90% confidence limit of particle image location is $\langle\epsilon\rangle_{90}$ in both the x- and y-directions. In order to find the errors in the particle position due to errors in particle image positions, a particle in 3-D space is projected onto each CCD. Errors are then added to the x and y placement of these images. This is to say, using the equations in Section 1.1.2, we have

$$\boldsymbol{I}_1 = \left(-\frac{x}{Sz} d_{\mathrm{C}} + \Delta x_1, \frac{r\,(L-z) - Ly}{SzL} d_{\mathrm{C}} + \Delta y_1 \right), \tag{3.5}$$

$$\boldsymbol{I}_2 = \left(\frac{-2Lx + \sqrt{3}\,r\,(L-z)}{2SzL} d_{\mathrm{C}} + \Delta x_2, \frac{-r\,(L-z) - 2Ly}{2SzL} d_{\mathrm{C}} + \Delta y_2 \right), \tag{3.6}$$

$$\boldsymbol{I}_3 = \left(\frac{-2Lx - \sqrt{3}\,r\,(L-z)}{2SzL} d_{\mathrm{C}} + \Delta x_3, \frac{-r\,(L-z) - 2Ly}{2SzL} d_{\mathrm{C}} + \Delta y_3 \right), \tag{3.7}$$

where Δx_i and Δy_i have the same 90% confidence interval ($\langle\Delta x_i\rangle_{90} = \langle\Delta y_i\rangle_{90} = \langle\epsilon\rangle_{90}$). Then the particle images, with error added, are projected back into three-dimensional space and the point of closest ray intersection is considered the particle position. The error in particle position is then the distance from the original particle position to the particle position found after errors were added. To simplify the results obtained, several assumptions were made: $r^2 \ll z^2$, $x^2 \ll z^2$, and $y^2 \ll z^2$. For our system, the ratios $\frac{r^2}{z^2}$, $\frac{x^2}{z^2}$, and $\frac{y^2}{z^2}$ are

less than 1%. To first order, this gives the following errors

$$\Delta P_x^{\mathrm{p}} = \frac{-zS}{3d_{\mathrm{C}}}\left((\Delta x_1 + \Delta x_2 + \Delta x_3) + \frac{\sqrt{3}\,x}{2r}(\Delta x_2 - \Delta x_3) + \frac{x}{2r}(2\Delta y_1 - \Delta y_2 - \Delta y_3)\right), \tag{3.8}$$

$$\Delta P_y^{\mathrm{p}} = \frac{-zS}{3d_{\mathrm{C}}}\left((\Delta y_1 + \Delta y_2 + \Delta y_3) + \frac{\sqrt{3}\,y}{2r}(\Delta x_2 - \Delta x_3) + \frac{y}{2r}(2\Delta y_1 - \Delta y_2 - \Delta y_3)\right), \tag{3.9}$$

$$\Delta P_z^{\mathrm{p}} = \frac{-z^2S}{3d_{\mathrm{C}}r}\left(\frac{\sqrt{3}}{2}(\Delta x_2 - \Delta x_3) + \frac{1}{2}(2\Delta y_1 - \Delta y_2 - \Delta y_3)\right). \tag{3.10}$$

The distribution of the particle position errors, ΔP_i^{p}, is unbiased, *i.e.*, $\mu_i^{\mathrm{p}} = 0$. Again, i is either x, y, or z. The 90% confidence limits of particle locations can then be evaluated and are

$$\langle \Delta P_x^{\mathrm{p}} \rangle_{90} = \frac{z\sqrt{r^2 + x^2}}{\sqrt{3}\,d_{\mathrm{C}}r} S \langle \epsilon \rangle_{90}\,, \tag{3.11}$$

$$\left\langle \Delta P_y^{\mathrm{p}} \right\rangle_{90} = \frac{z\sqrt{r^2 + y^2}}{\sqrt{3}\,d_{\mathrm{C}}r} S \langle \epsilon \rangle_{90}\,, \tag{3.12}$$

$$\langle \Delta P_z^{\mathrm{p}} \rangle_{90} = \frac{z^2}{\sqrt{3}\,d_{\mathrm{C}}r} S \langle \epsilon \rangle_{90}\,. \tag{3.13}$$

In the case of velocimetry, the 90% confidence limits of velocities are simply

$$\langle \Delta U_x^{\mathrm{p}} \rangle_{90} = \frac{\sqrt{2}}{t_{\mathrm{s}}} \langle \Delta P_x^{\mathrm{p}} \rangle_{90} = \frac{z\sqrt{2\,(r^2 + x^2)}}{\sqrt{3}\,t_{\mathrm{s}}d_{\mathrm{C}}r} S \langle \epsilon \rangle_{90}\,, \tag{3.14}$$

$$\left\langle \Delta U_y^{\mathrm{p}} \right\rangle_{90} = \frac{\sqrt{2}}{t_{\mathrm{s}}} \left\langle \Delta P_y^{\mathrm{p}} \right\rangle_{90} = \frac{z\sqrt{2\,(r^2 + y^2)}}{\sqrt{3}\,t_{\mathrm{s}}d_{\mathrm{C}}r} S \langle \epsilon \rangle_{90}\,, \tag{3.15}$$

$$\langle \Delta U_z^{\mathrm{p}} \rangle_{90} = \frac{\sqrt{2}}{t_{\mathrm{s}}} \langle \Delta P_z^{\mathrm{p}} \rangle_{90} = \frac{z^2\sqrt{2/3}}{t_{\mathrm{s}}d_{\mathrm{C}}r} S \langle \epsilon \rangle_{90}\,. \tag{3.16}$$

It is assumed that there is negligible error associated with the time separation, t_{s}, which for modern timing systems is true. The ratios of these confidence limits take a very simple

form:

$$\frac{\langle \Delta U_z^{\mathrm{p}} \rangle_{90}}{\langle \Delta U_x^{\mathrm{p}} \rangle_{90}} = \frac{\langle \Delta P_z^{\mathrm{p}} \rangle_{90}}{\langle \Delta P_x^{\mathrm{p}} \rangle_{90}} = \frac{z}{\sqrt{r^2 + x^2}}, \tag{3.17}$$

$$\frac{\langle \Delta U_z^{\mathrm{p}} \rangle_{90}}{\langle \Delta U_y^{\mathrm{p}} \rangle_{90}} = \frac{\langle \Delta P_z^{\mathrm{p}} \rangle_{90}}{\langle \Delta P_y^{\mathrm{p}} \rangle_{90}} = \frac{z}{\sqrt{r^2 + y^2}}. \tag{3.18}$$

If we integrate the errors in a x–y plane contained in the test volume, which will be useful for comparisons with experiments, we find that the 90% confidence limit of plate-averaged velocities due to peak searching, σ^{p}, are

$$\sigma_x^{\mathrm{p}} = \sigma_y^{\mathrm{p}} = \left\langle \overline{\Delta U_x^{\mathrm{p}}} \right\rangle_{90} = \left\langle \overline{\Delta U_y^{\mathrm{p}}} \right\rangle_{90} = \frac{z\sqrt{12r^2 + d^2}}{3\sqrt{2}\, t_{\mathrm{s}} d_{\mathrm{C}} r}\, S \left\langle \epsilon \right\rangle_{90}, \tag{3.19}$$

$$\sigma_z^{\mathrm{p}} = \left\langle \overline{\Delta U_z^{\mathrm{p}}} \right\rangle_{90} = \frac{z^2\sqrt{2/3}}{t_{\mathrm{s}} d_{\mathrm{C}} r} S \left\langle \epsilon \right\rangle_{90}, \tag{3.20}$$

where d is the side length of the test volume. The ratios of these confidence intervals are

$$\frac{\sigma_z^{\mathrm{p}}}{\sigma_x^{\mathrm{p}}} = \frac{\sigma_z^{\mathrm{p}}}{\sigma_y^{\mathrm{p}}} = \frac{2\sqrt{3}\, z}{\sqrt{12r^2 + d^2}}. \tag{3.21}$$

These ratios are typically of order 15. The errors in positions and ratios of errors in Equations 3.19 through 3.21 will be assumed to be the errors over the entire x–y plane for simplicity. This assumption will result in a maximum relative difference between Equations 3.17 and Equation 3.21 in the test volume of

$$1 - \sqrt{\frac{12r^2 + d^2}{12r^2 + 3d^2}}, \tag{3.22}$$

which for the current situation is approximately 9%.

One can expect the error to decrease if the time separation increases. However t_{s} is limited because the particles must not leave the test volume between frames and, because, if the corresponding particles are separated by a large distance, it can be difficult to get these corresponding particles back, and if we do, the velocity obtained will just be a time-integrated average.

3.2.1 Best Linear Unbiased Estimate (BLUE)

It is interesting to examine the algorithms used by DDPIV and 3DPTV to determine particle position, in particular, whether or not these algorithms produce the best linear unbiased estimates (BLUE) of the actual particle position. Kajitani *et al.* [17] perform an error analysis independent of any particle locating algorithm. First, they consider how a small perturbation of the particle position will affect its image locations. To do that, they let $(\Delta x,\ \Delta y,\ \Delta z)$ be the perturbation of the particle position and they let $(\Delta x_i,\ \Delta y_i)$ be the perturbation of its image on CCD i. The following equation can then be written for $i = 1, 2, 3$:

$$(\Delta x_i, \Delta y_i) = \frac{\partial \boldsymbol{I}_i}{\partial x}\Delta x + \frac{\partial \boldsymbol{I}_i}{\partial y}\Delta y + \frac{\partial \boldsymbol{I}_i}{\partial z}\Delta z, \tag{3.23}$$

where $\boldsymbol{I}_i$ is the coordinate of the particle image on CCD i and is given in Section 1.1.2. This leads to the following system:

$$\begin{pmatrix} \Delta x_1 \\ \Delta y_1 \\ \Delta x_2 \\ \Delta y_2 \\ \Delta x_3 \\ \Delta y_3 \end{pmatrix} = \frac{d_{\mathrm{C}}}{z^2 S} \begin{pmatrix} -z & 0 & x \\ 0 & -z & y - r \\ -z & 0 & x - \frac{\sqrt{3}}{2}r \\ 0 & -z & y + \frac{1}{2}r \\ -z & 0 & x + \frac{\sqrt{3}}{2}r \\ 0 & -z & y + \frac{1}{2}r \end{pmatrix} \begin{pmatrix} \Delta x \\ \Delta y \\ \Delta z \end{pmatrix}. \tag{3.24}$$

Now, they assume the opposite—they have perturbations of $(\Delta x_i,\ \Delta y_i)$ and they would like to find what perturbations this induces on the particle position. The system 3.24 is overdetermined and an optimal solution in the least square sense can be obtained. It can be shown that a linear overdetermined system of the form $\boldsymbol{A}\boldsymbol{x} = \boldsymbol{b}$ has an optimal solution in the least-square sense of the form

$$\boldsymbol{x} = \left(\boldsymbol{A}^{\mathrm{T}}\boldsymbol{A}\right)^{(-1)} \boldsymbol{A}^{\mathrm{T}}\boldsymbol{b}, \tag{3.25}$$

where the superscripts $^{\mathrm{T}}$ and $^{(-1)}$ correspond to the transpose and the inverse of a matrix [18]. Applying this to their system, they get

$$\begin{pmatrix}\Delta x\\ \Delta y\\ \Delta z\end{pmatrix} = \frac{-zS}{3rd_{\mathrm{C}}}\begin{pmatrix} r & x & r+\frac{\sqrt{3}}{2}x & -\frac{1}{2}x & r-\frac{\sqrt{3}}{2}x & -\frac{1}{2}x \\ 0 & r+y & \frac{\sqrt{3}}{2}y & r-\frac{1}{2}y & -\frac{\sqrt{3}}{2}y & r-\frac{1}{2}y \\ 0 & z & \frac{\sqrt{3}}{2}z & -\frac{1}{2}z & -\frac{\sqrt{3}}{2}z & -\frac{1}{2}z \end{pmatrix}\begin{pmatrix}\Delta x_1\\ \Delta y_1\\ \Delta x_2\\ \Delta y_2\\ \Delta x_3\\ \Delta y_3\end{pmatrix}. \tag{3.26}$$

Assuming that Δx_i and Δy_i are errors that have a 90% confidence interval $\langle\epsilon\rangle_{90}$, we can find the 90% confidence interval of the particle positions

$$\langle\Delta U_x\rangle_{90} = \frac{\sqrt{2}}{t_{\mathrm{s}}}\langle\Delta x\rangle_{90} = \frac{z\sqrt{2\left(r^2+x^2\right)}}{\sqrt{3}\,t_{\mathrm{s}}d_{\mathrm{C}}r}S\langle\epsilon\rangle_{90}\,, \tag{3.27}$$

$$\langle\Delta U_y\rangle_{90} = \frac{\sqrt{2}}{t_{\mathrm{s}}}\langle\Delta y\rangle_{90} = \frac{z\sqrt{2\left(r^2+x^2\right)}}{\sqrt{3}\,t_{\mathrm{s}}d_{\mathrm{C}}r}S\langle\epsilon\rangle_{90}\,, \tag{3.28}$$

$$\langle\Delta U_z\rangle_{90} = \frac{\sqrt{2}}{t_{\mathrm{s}}}\langle\Delta z\rangle_{90} = \frac{z^2\sqrt{2/3}}{t_{\mathrm{s}}d_{\mathrm{C}}r}S\langle\epsilon\rangle_{90}\,. \tag{3.29}$$

These results do not consider any particular algorithm to find the position of a particle knowing its image positions on the CCDs. This means that, unlike what is claimed by Kajitani *et al.* [17], these results are not necessarily the errors of DDPIV or 3DPTV, but they are the errors in the least-square sense that one can obtain with the best possible algorithm. In this case, the best possible algorithm refers to the algorithm that will lead to the minimum least-square error in particle position, given errors on the particle images. Comparing these results with ours, we see that we have the exact same expressions, which means that our ray tracing algorithm is BLUE under these conditions. Note that although Kajitani *et al.* didn't prove it, the algorithm used by DDPIV is also BLUE.

3.3 Combined Error

The error due to peak searching and calibration can then be joined to form a combined error. From Section 3.2 we see that the expected value of the velocity error due to peak searching algorithm is zero; therefore, the expected value of the total error, μ_i, is just that due to calibration error, *i.e.*, $\mu_i = \mu_i^{\mathrm{c}}$. Since calibration error is proportional to velocity, the combined mean error will also be proportional to velocity. Both calibration and peak searching contribute to the deviation error. Because the errors due to peak searching and calibration are uncorrelated, the combined 90% confidence limit of plate-averaged velocity deviation, σ_i, is

$$\sigma_i = \sqrt{(\sigma_i^{\mathrm{c}})^2 + (\sigma_i^{\mathrm{p}})^2}\,, \tag{3.30}$$

where i is x, y, or z. If the medium surrounding the camera does not have a constant index of refraction, the combined error is slightly different. However, the error is of the same order.

Chapter 4

Results

In this section, several results will be presented. The first two of these are theoretical results to examine the highest accuracy that can be obtained using our data analysis program (Sections 4.1 and 4.2). A movable plate is then examined to experimentally determine the errors in displacements (Section 4.3). A slightly less serious but quite impressive result is then presented, which shows, using a doll face, how well a surface can be represented in a single measurement (Section 4.4). A supersonic flow result will then be presented (Section 4.5). Finally, measurements of the vortex generated by the tip of a delta wing, conducted in a water tunnel, are presented in Section 4.6.

4.1 Peak Searching

A synthetic image containing 10,000 particles with known positions was created. Each particle had a Gaussian intensity distribution. In this paper, a particle image radius is defined as the radius at which the intensity of the image reaches 10% of its maximum. The particle image radii in the test of the peak searching algorithm varied between 2 px and 4 px. The intensity, position, and radius of each of the particle images were completely random, within the constraint range. Because there were 10,000 particle images distributed over 1 Mpx many of the particle images overlapped.

The program successfully identified 9,911 particles out of 10,000. The missing particles are mostly those with neighbors within 0.5 px, that is to say, they are so close that they are virtually indistinguishable. For each of the particles that were found, the closest real

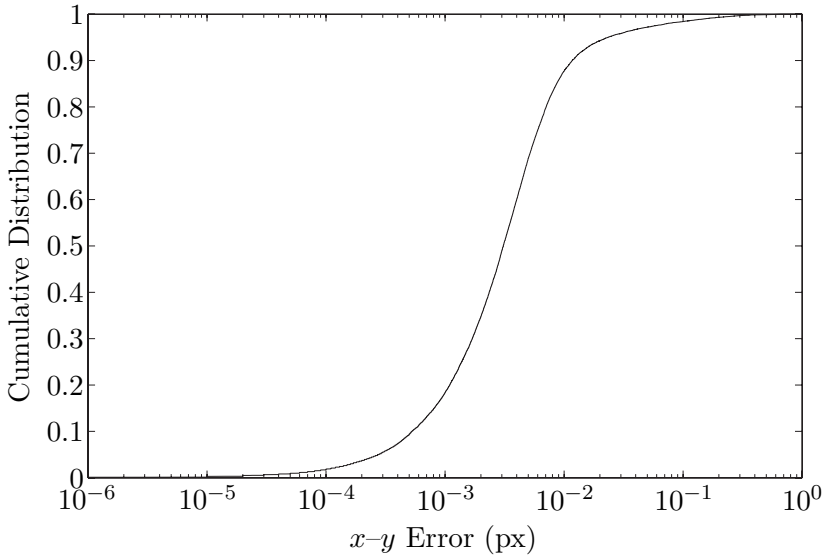

Figure 4.1: Cumulative distribution function of particles.

particle was selected in order to evaluate the errors. These results are shown in Figure 4.1. The error is smaller than 0.01 px in each direction for most of the peaks (87.7%) and for the vast majority (94.3%), is closer than 0.02 px to their actual location. The 90% confidence limit is 0.0117 px (which corresponds to $\langle\epsilon\rangle_{90}$ in Equations 3.19 and 3.20), while the mean error is 0.00926 px. It is also interesting to note that only 8,446 local maxima exist on the image. This means that routines using simple local maxima fitting would find at most 6,892 correct particle images. The remaining local maxima will contain two or more particle images, which cannot be computed correctly using local maxima fitting. The key to getting accurate results is having a good fitting function. For these theoretical results, a Gaussian fitting function was used in the peak searching routine, and each particle image was given a Gaussian distribution; therefore, these results represent the best possible accuracy of the peak searching algorithm.

4.2 Synthetic Images

An important test of the 3DPTV system was the processing of synthetic images. These images allow for a complete testing of the program, including triangle formation and trian-

gulation calculations.

The domain was divided into 21 planes perpendicular to the camera axis. In each of these planes, 400 particles were randomly distributed and their images were added to form the synthetic images. Therefore, each synthetic image contained 8,400 particle images. Each particle image was Gaussian blurred with a 10% blur radius of approximately 3 px. A total of 300 sets of images were created and then processed. In each of the planes, the results were averaged to evaluate the errors (*i.e.*, each symbol on Figures 4.2 and 4.3 represents an average of 120,000 results).

As expected, the mean error tends to zero. In each of the planes, the mean error is less than 0.005 μm in the x- and y-directions, and less than 0.05 μm in the z-direction.

The 90% confidence limit was also evaluated and is shown in Figure 4.2. As expected, this error varies according to Equations 3.19 and 3.20. The $\langle\epsilon\rangle_{90}$ value was set to 0.05. This value is a little larger than expected in Section 4.1. Two reasons can be found to explain that difference. First, in Section 4.1, the density of particle images is constant over the entire CCD; however, for this test case, the density of particles is constant in the test volume and hence the particle image density is not constant. The second reason is that in Section 4.1, to create the synthetic images, the pixel intensity level was determined by the value of each Gaussian surface at the center of the pixel; however, in this section, the pixel intensity level was obtained by integrating the Gaussian surface over the entire pixel. It is important to note that in actuality, the pixel level is somewhere between these two cases. The actual intensity of each pixel is given by

$$A_\mathrm{t} = \int_{-S/2}^{S/2}\int_{-S/2}^{S/2} W(x,y)\, A(x,y)\; dx\, dy, \tag{4.1}$$

where A_t is the intensity of the pixel, $A(x,y)$ is the intensity distribution of the light hitting the pixel, and $W(x,y)$ is the sensitivity distribution of the pixel. This sensitivity distribution is higher at the center of the pixel and decreases toward the edges. The two extreme cases are $W(x,y) = K\delta(x,y)\,\delta(x,y)$ and $W(x,y) = K/S^2$, where K is a constant. These two cases correspond to the results in Section 4.1 and in this section, respectively. If we can assume a Gaussian distribution of light and no noise, one can expect that the actual

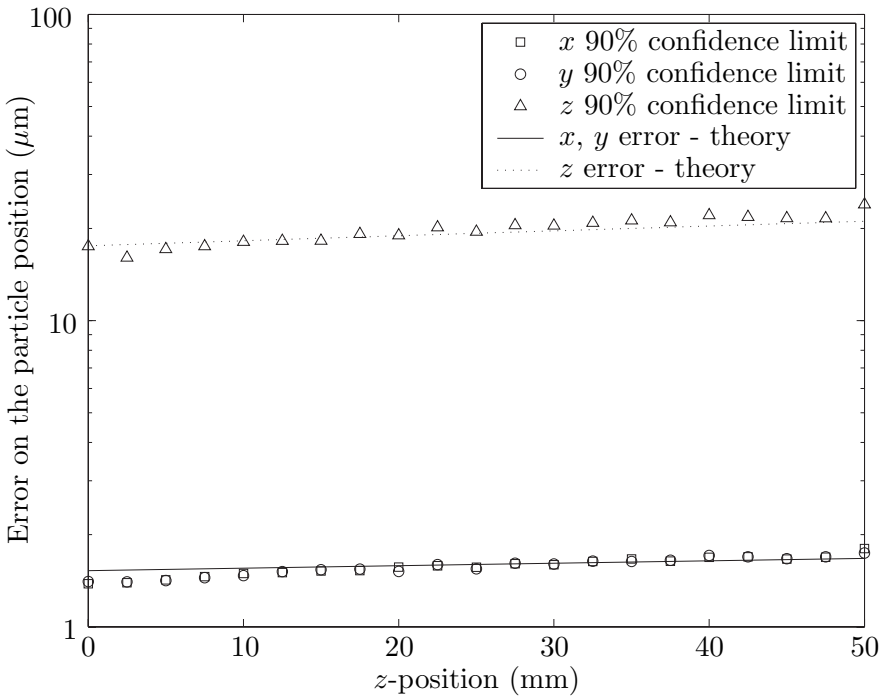

Figure 4.2: 90% confidence limit of particle positions from synthetic images.

pixel sensitivity distribution will lead to errors that are between these two extremes.

The ratio of the 90% confidence limit of the positions was also evaluated, as is shown in Figure 4.3, and shows a very good agreement with the trend line obtained theoretically from Equation 3.21.

4.3 Experimental Verification

A movable plate test case was performed using a flat plate with an array of white dots on a black background. There were 100 dots per square inch. The plate was placed at z-positions of 469, 494, 519, 529, 539, 549, 559, 569, 594, and 619 mm from the camera. The plate was then moved in three equal increments of 2.54 mm in the y-direction for each of the z-locations, which resulted in a total of six displacement vectors for each z-position (three displacements of 2.54 mm, two displacements of 5.08 mm, and one displacement of 7.62 mm). Similarly the plate was moved in three equal increments of 2.54 mm in the z-direction for each z-position.

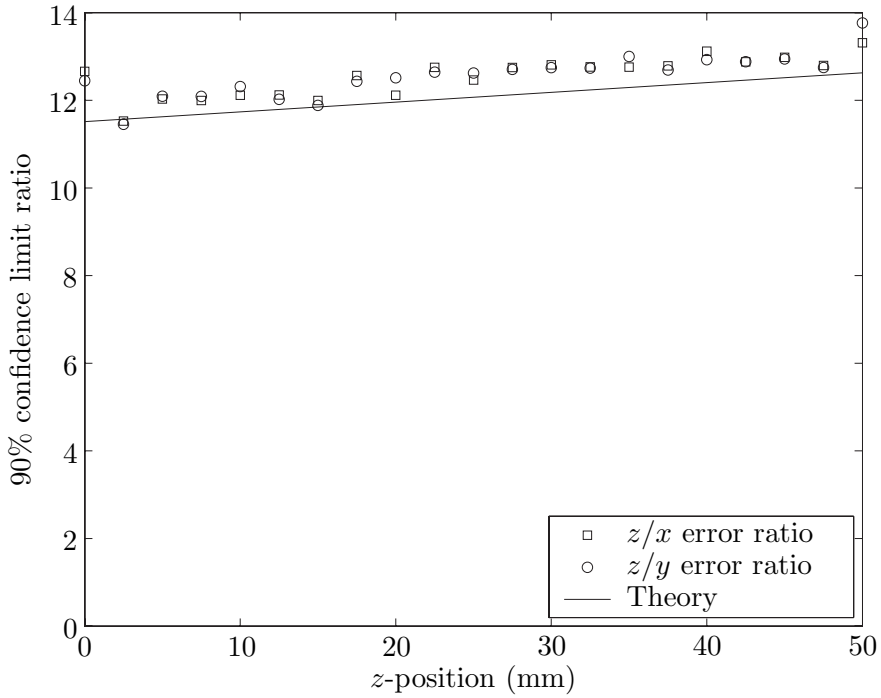

Figure 4.3: Ratio of the 90% confidence limits of particle positions from synthetic images.

First, the mean error was evaluated, and as expected is proportional to the displacement as shown in Equation 3.4. Figure 4.4 shows the relative mean error obtained for 2.54 mm and 5.08 mm displacements; each data point is an average of three and two values, respectively. In this plot, the 7.62 mm results are not shown since they correspond to the average of the three 2.54 mm results.

Even though the mean errors are very small, all within 2%, they are larger than expected. One reason for some of the inaccuracy, besides the camera system itself, is lack of precision in the testing setup. In particular, the precision with which the testing target could be moved was on the order of the mean errors.

The 90% confidence limit of the displacements was also evaluated. The results are plotted in Figure 4.5. Each symbol is the average of the 90% confidence limits from three and two data sets in the 2.54 mm and the 5.08 mm cases, respectively.

One can directly note that the results depend on the displacement distance of the plate. Our theory tells us that error due to peak searching (Section 3.2) does not depend on the displacement, whereas the error due to calibration (Section 3.1) is proportional to the

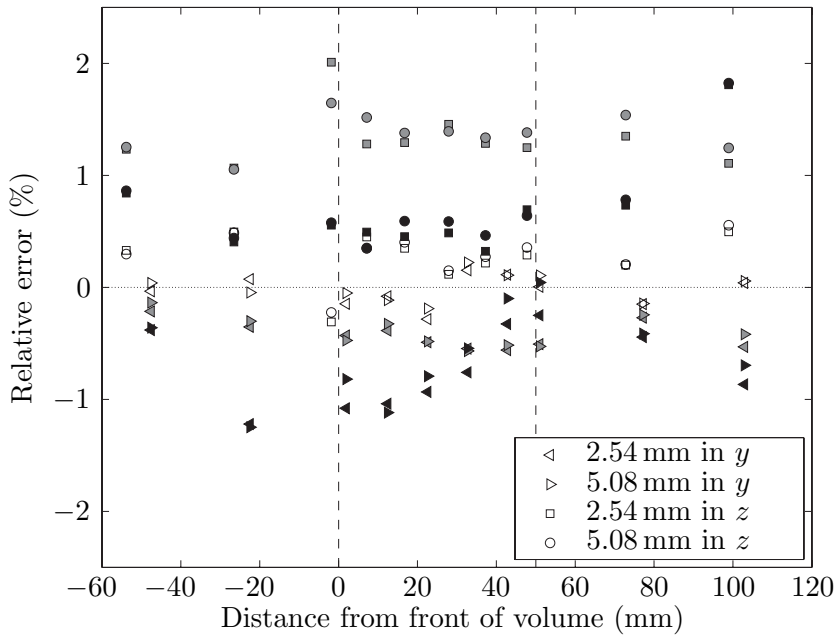

Figure 4.4: Plate-averaged displacement errors. White, grey, and black symbols refer to the errors in the x-, y-, and z-directions, respectively. The 2.54 mm and the 5.08 mm cases are the average of three and two data points, respectively.

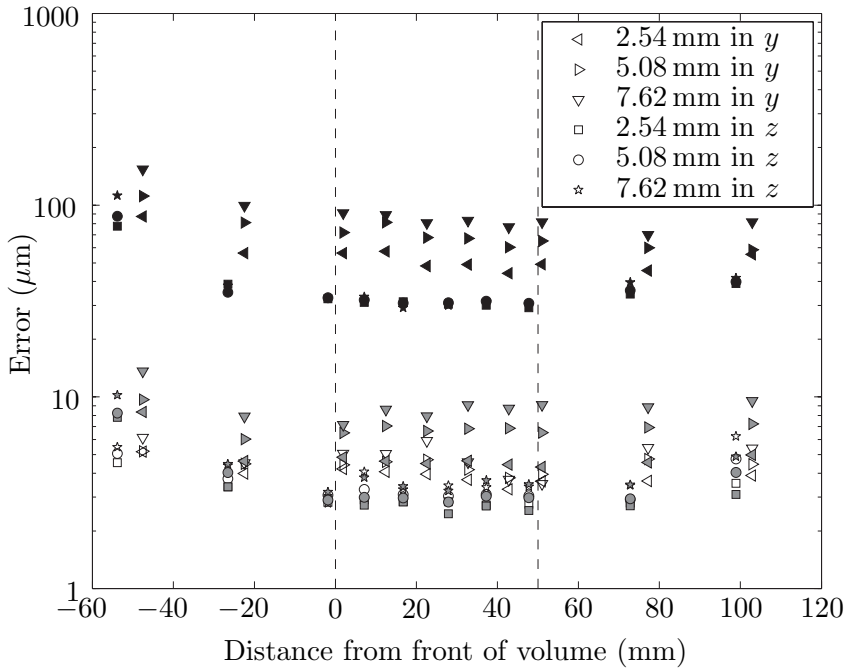

Figure 4.5: 90% confidence limits of plate-averaged displacements. White, grey, and black symbols refer to the errors in the x-, y-, and z-directions, respectively. The 2.54 mm and the 5.08 mm cases are the average of three and two data points, respectively.

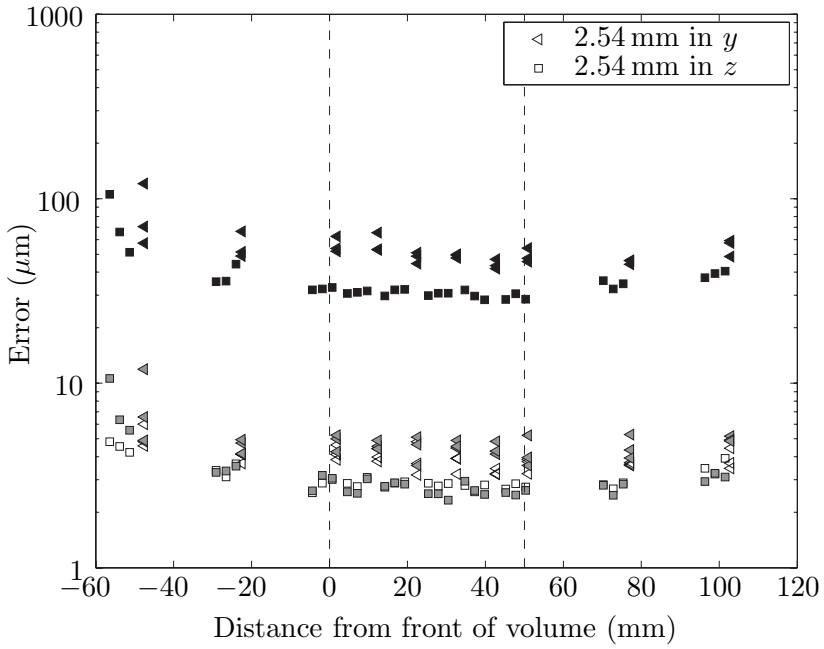

Figure 4.6: 90% confidence limits of plate-averaged displacements. White, grey, and black symbols refer to the errors in the x-, y-, and z-directions, respectively.

velocity (or, for a given time separation, the displacement). As Equation 3.30 shows, the combined 90% confidence limit of plate-averaged displacement, $\langle\overline{\Delta D_i}\rangle_{90}$, can be written as

$$\langle\overline{\Delta D_i}\rangle_{90} = t_{\mathrm{s}}\sqrt{(\sigma_i^{\mathrm{c}})^2 + (\sigma_i^{\mathrm{p}})^2}\,. \tag{4.2}$$

Since, for most flow measurements, the displacement of the particles will be smaller than 2.54 mm, it is interesting to analyze the results for this particular displacement, as this represents the worst case scenario. Figure 4.6 therefore gives an upper bound for the 90% confidence limit one can expect with the 3DPTV setup. According to these results, the 90% confidence limit in the test volume remains under 5.2 μm in the x- and y-directions, and under 66 μm in the z-direction.

To be able to compare with some of the results obtained previously, it is necessary to separate the constant part of the 90% confidence limit from its varying part, as in Equation 4.2. Using the results shown in Figure 4.5, one can obtain these two terms.

The constant part of the 90% confidence limit of displacement can be obtained theoretically from Equations 3.19 and 3.20. Both the theoretical values and the experimental data

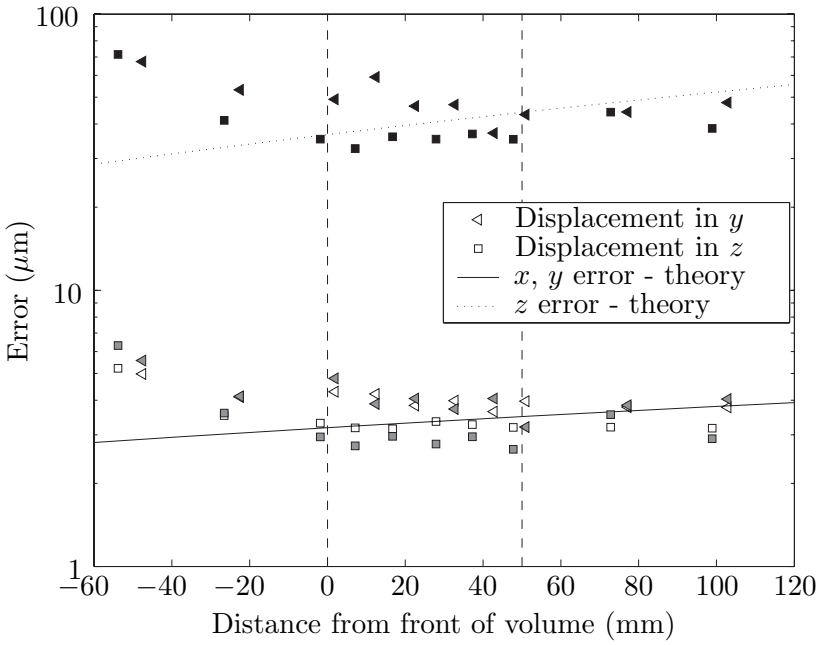

Figure 4.7: Fixed part of 90% confidence limits of plate-averaged displacements. White, grey, and black symbols refer to the errors in the x-, y-, and z-directions, respectively.

are shown in Figure 4.7. For the theoretical curves, the $\langle\epsilon\rangle_{90}$ value was found by performing a single least-squares fit to all the data inside the volume. This fit produced an $\langle\epsilon\rangle_{90}$ value of 0.069 px. This value is fairly close but higher than the one obtained with synthetic images in Section 4.2. The discrepancy in the results for low z-position comes from the fact that the dots on the plate appear very blurred and that the amplitude of the peaks becomes very low.

Another important result is the ratio of the constant parts of the error. According to theory, the ratio between the x or y constant part of the 90% confidence limit, and the z constant part of the 90% confidence limit is given by Equation (3.21). The theoretical, parameter-free curve, as well as the experimental values for this ratio are shown in Figure 4.8.

The varying part of the 90% confidence limit is presented in Figure 4.9. These errors remain quite small (1 μm per mm in x or y and 10 μm per mm in z); however, part of the error may be due to lack of robustness of the test setup, in particular the placement and precision of the testing target.

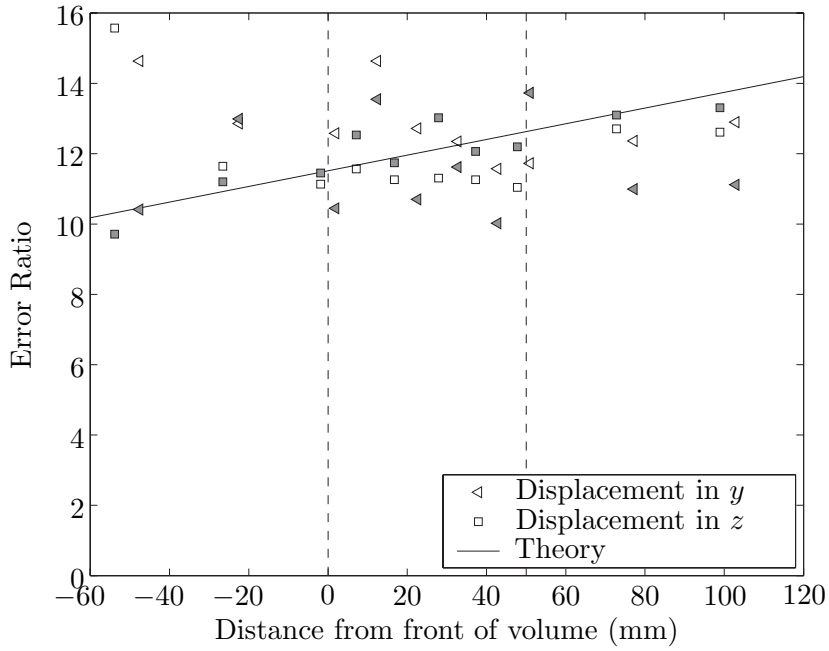

Figure 4.8: Ratio of fixed part of 90% confidence limits of plate-averaged displacements. Empty and grey symbols refer to the ratio of the constant part of the 90% confidence limit in the x- and y-directions, respectively, and the constant part of the 90% confidence limit in the z-direction.

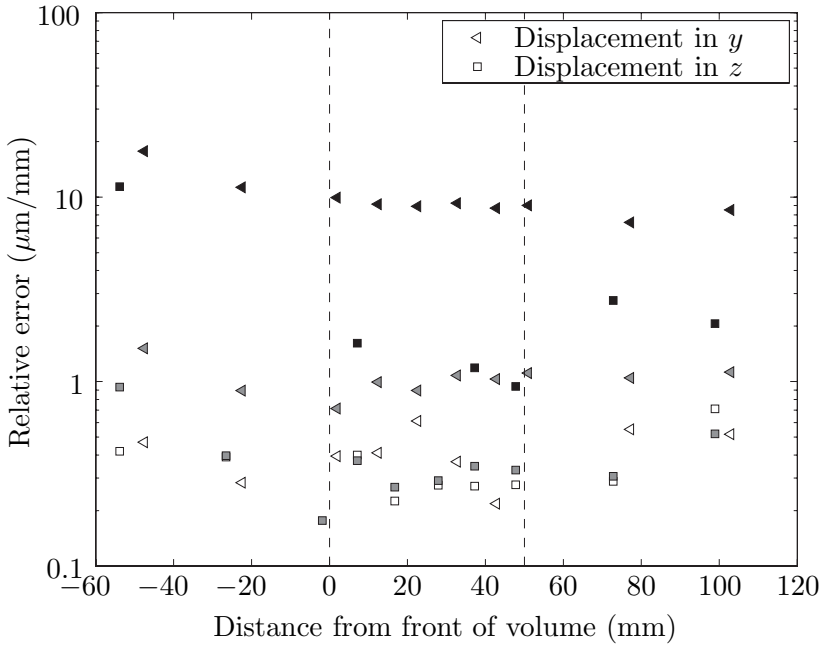

Figure 4.9: Variable part of 90% confidence limits of plate-averaged displacements. White, grey, and black symbols refer to the errors in the x-, y-, and z-directions, respectively.

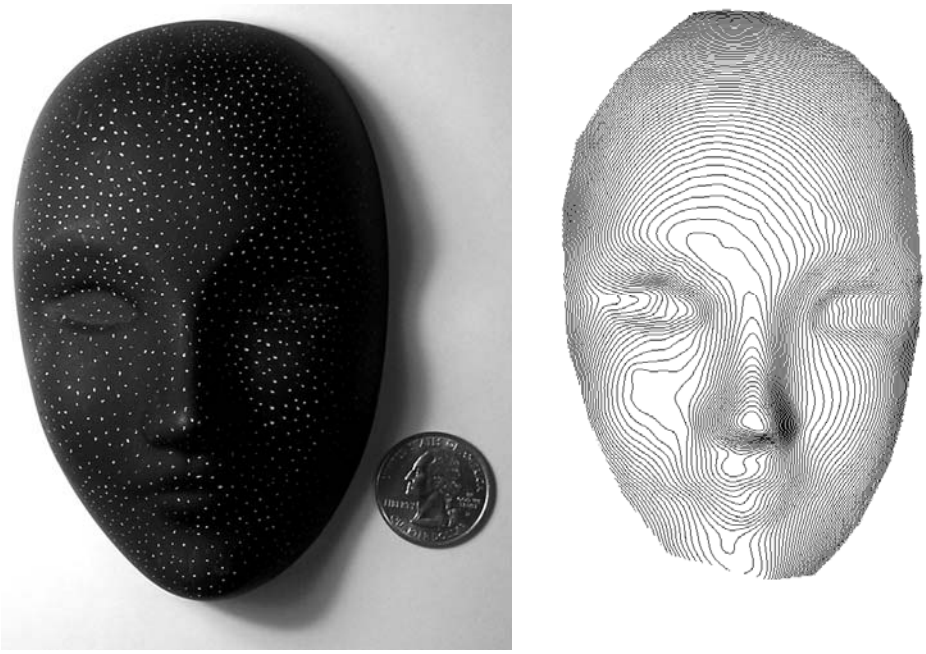

Figure 4.10: Three-dimensional solid imaging of a doll face. Left: black doll's face with white dots. Right: contours of doll's face from measurements with the camera. These results were taken with an older version camera having less accuracy but able to image a $10 \times 10 \times 10\,\mathrm{cm}^3$ volume.

4.4 3D Solid Imaging

An additional capability of the 3DPTV system is 3-D solid imaging. To illustrate this capability the system was used to image the face of a doll. This was done by painting a doll face black, and putting a large number of white dots on the face. While it is hard to make analytic conclusions from the results, Figure 4.10 shows excellent resolution of the face. Some of the roughness on the image is possibly due to the fact that some of the white dots were large and non-circular. Note that these results were obtained using an old version camera, which did not take advantage of offsets or of calibration. This camera was able to investigate a $10 \times 10 \times 10$ cm^3 volume but with a much lower accuracy.

4.5 Sonic Jet Injection

The 3DPTV system was used to image a supersonic gas flow. Three-dimensional particle tracking measurements in supersonic flows are particularly challenging and present many

problems not seen in slower flows or in two-dimensional particle tracking. First, in order for the particles to respond quickly to the flow, they must be very small. In addition, since we have to illuminate a volume instead of a sheet, the illumination intensity is much smaller. These two factors lead to particles that become very hard to detect.

Experiments using a sonic jet injector with 1 μm diameter olive oil droplets were conducted. Even with a 200 mJ Nd:YAG laser the intensity of the light scattered by the particles was very low and detection was very difficult. Despite the very low signal-to-noise ratio (about 1) the 3DPTV system was able to produce an accurate velocity field. Figure 4.11 shows an instantaneous velocity field containing 224 vectors, which is approximately 35 vectors per cubic centimeter. The particles were accelerated to sonic speeds through a converging nozzle with an outlet diameter of 7 mm. The region downstream of the injector nozzle was kept in vacuum; therefore, the particles continued to accelerate to supersonic speeds after exiting the injector. The speed of the particles ranged between 350 m/s and 500 m/s.

The original plan to study transverse jet injection into a supersonic gas flow had to be abandoned because we lacked the funds to upgrade the laser system to a level where a sufficiently large number of vectors could be acquired.

4.6 Delta Wing Experiment

Measurements of the vortex generated by a delta wing were conducted in a water tunnel at the University of Washington. A delta wing with a 65.5° sweep angle was placed at a 25° angle of attack. The free-stream speed of the tunnel was 10 cm/s. The results presented below were obtained by time-averaging multiple vector fields.

Figure 4.12 shows the experimental setup. In both views the location of the laser beam with respect to the delta wing is shown. The side view shows the placement of the camera and the glass of the water tunnel. The coordinate system, i, is centered at the tip of the delta wing. i_1 is along the centerline of the delta wing, i_2 is in the plane of the delta wing and perpendicular to the centerline, and i_3 is perpendicular to the surface of the delta wing.

Three slices of the velocity field are shown in Figure 4.13. The color represents the

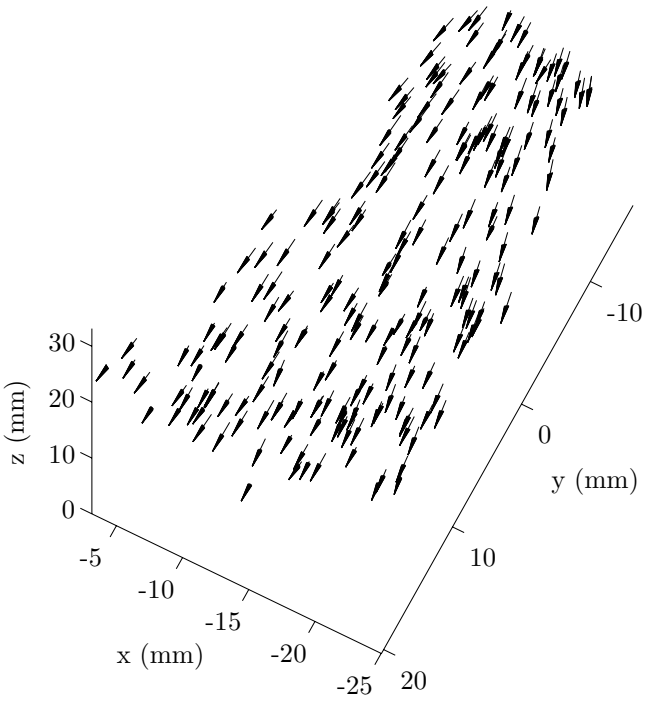

Figure 4.11: Velocity vectors of a sonic jet injector with 1 μm olive oil seeding particles.

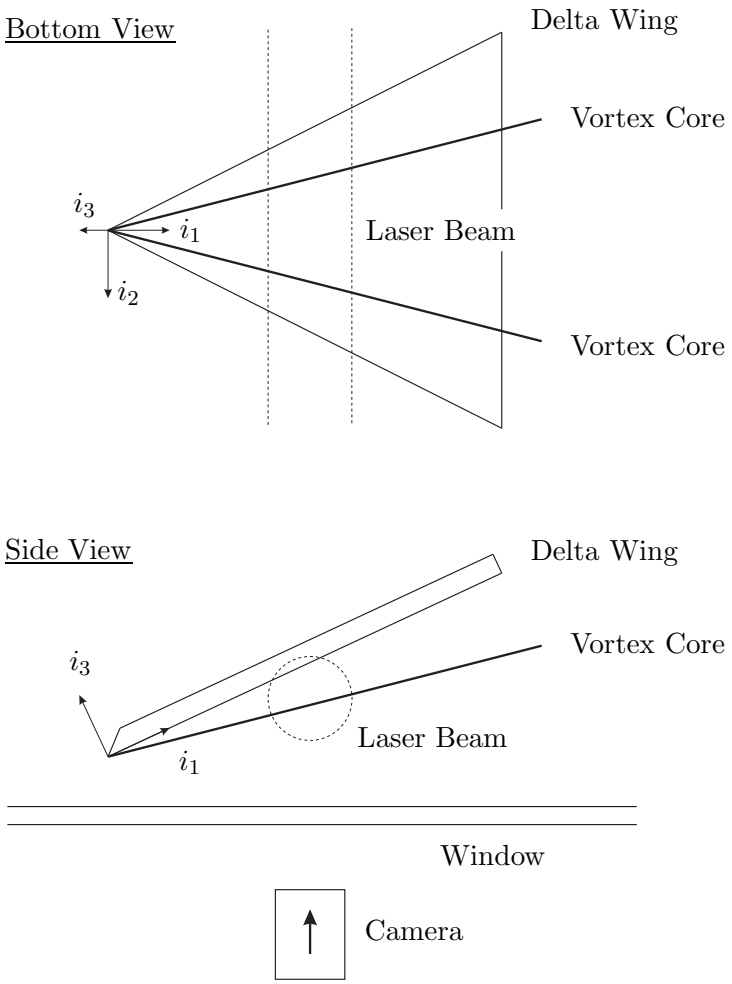

Figure 4.12: Delta wing setup for three-dimensional velocity measurements of a tip generated vortex.

magnitude of the velocity. The contours correspond to increments of 0.02 cm/s. Starting at an i_1 of 110 mm we see a high speed region, which corresponds to the vortex core. We see that at $i_1 = 180$ mm vortex breakdown has occurred as there is no longer a high speed core. The low speed region corresponds to the secondary vortex. The slices have been cropped at the delta wing.

An in-plane vector field plot at $i_1 = 145$ mm is shown in Figure 4.14. The vortex is clearly seen in the figure. Since the vector field created by 3DPTV is not on a regular grid, the data were interpolated onto a uniform grid. $i_3 = 0$ mm corresponds to the bottom of the delta wing, which is shown as an outline in the figure.

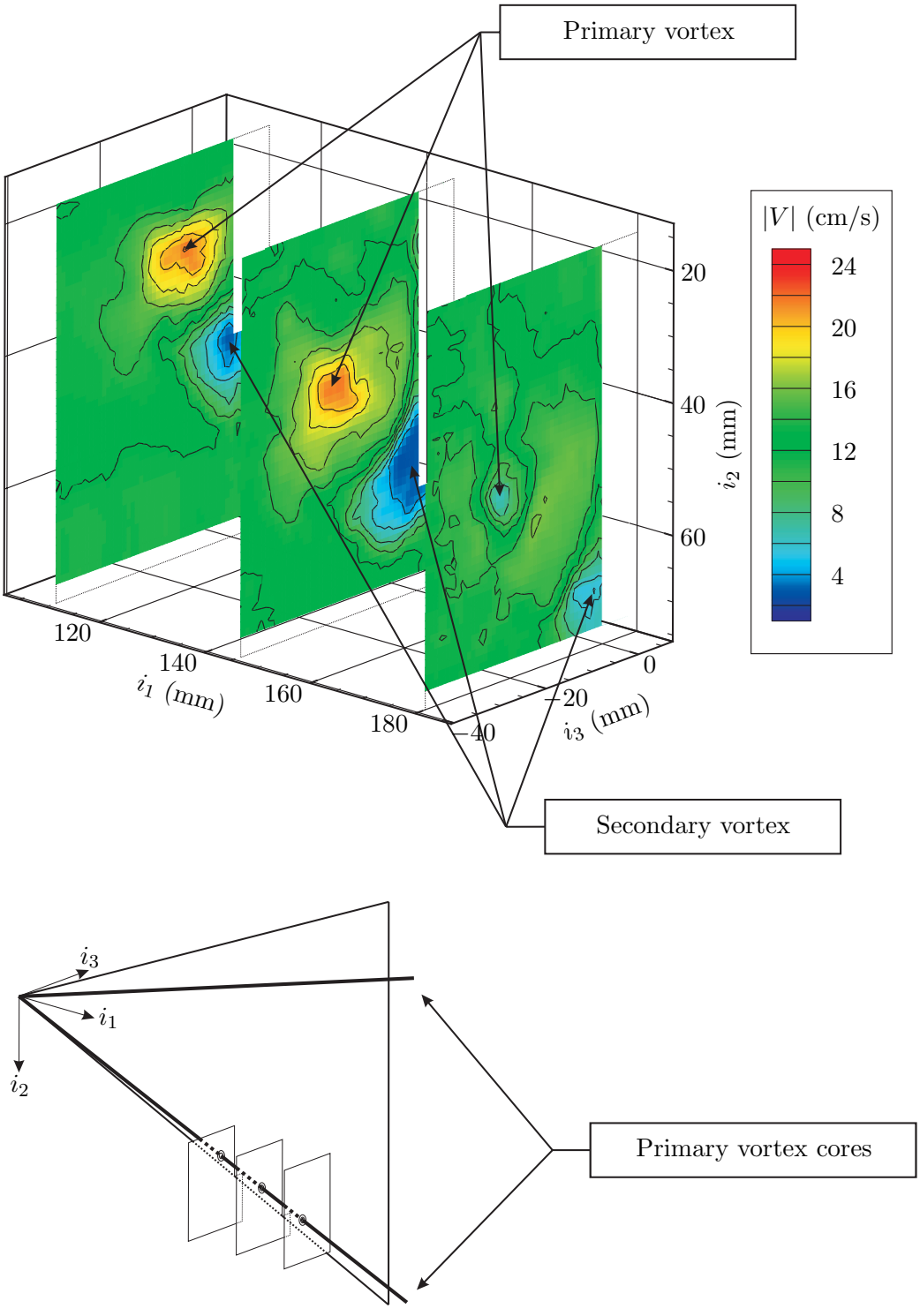

Figure 4.13: Three-dimensional slices (at i_1 of 110 mm, 145 mm and 180 mm) showing the breakdown of a vortex generated by a delta wing. The colors represent the magnitude of the flow velocity. Note that the slices are cropped at the wing location and that the wing is vertical. The position of the slices relative to the delta wing is shown in the lower part of the figure.

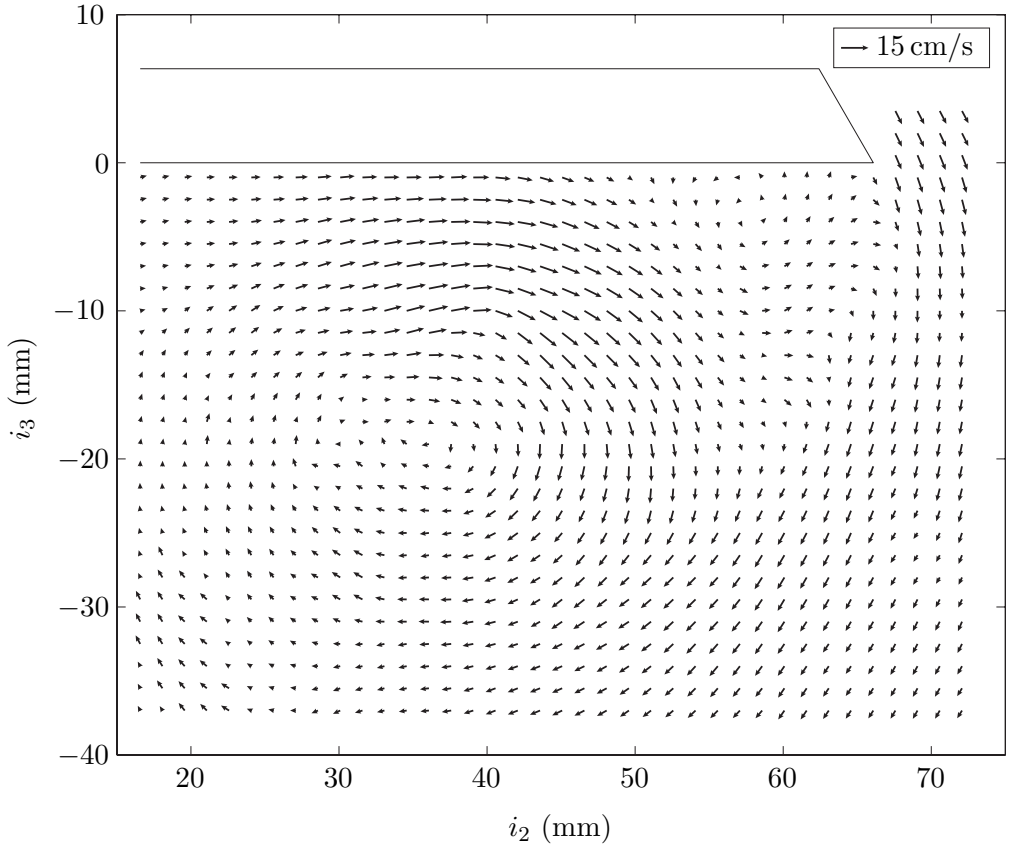

Figure 4.14: Vector field at $i_1 = 145\,\text{mm}$ showing the vortex generated by the tip of a delta wing.

Conclusions and Recommendations

In conclusion, the 3-D particle triangulation velocimetry technique that was implemented has been shown to produce excellent results in terms of accuracy. The errors were of the order of the best accuracy that can be achieved with the translation stages used. The upper bound estimate for the mean error is only 2% of the displacement and the 90% confidence interval is less than 5.2 μm in the x-, y-directions and less than 66 μm in the z-direction, for a $50\times50\times50\,\mathrm{mm}^3$ volume. These errors agree with the theoretical error analysis.

Several improvements can be made to increase the accuracy of the camera or to broaden its use. First, a substantial accuracy improvement in z can be obtained by increasing the radius of the lens positions, r, while still keeping the CCDs in a compact unit. One way of obtaining a large r is by physically separating the cameras, as many researchers do [2, 12, 16, 4]; however, physically separating the cameras is not recommended because of the additional calibration required and the lack of convenience when moving experiments. The camera used for the experiments maintained its calibration for over a year even though the camera was moved and used in several different test setups. Furthermore, preliminary experiments show that the accuracy in all directions can also be increased by focusing the camera inside the test volume (by reducing L and so increasing d_C). At the same time, the blur radius will be reduced and the number of overlapping particles will be significantly decreased, allowing for either a larger number of particles or for a lower processing time. Because of lens limitations, even these focused images will span multiple pixels. To minimize lens aberrations the axes of the lenses should intersect the center of the test volume.

The 3DPTV system was designed to be able to measure a wide variety of fluid flows as well as solid surfaces. In order to determine three-dimensional locations, individual particles must be found; this lends itself to direct particle tracking. In addition, particle

tracking, as opposed to a statistical method, works well even when there are low densities or large gradients. Since the velocity field is formed directly from the particle positions and not by averaging over several particles, it is important that these particles be found with a great deal of accuracy. In order to achieve high accuracy, a calibration process is essential. This calibration process corrects for the imperfect placement of the CCDs, for lens aberrations, and for other effects. Since the particle images are blurred they will often overlap on the CCD images. Because of this, a simple search for local maxima will produce very inaccurate results; therefore, the current software performs a least-squares optimization of a fitting function, which produces very good results.

Part II

Extension of Guderley's Solution for Converging Shock Waves

Nomenclature

Roman characters, lower case

a_k	kth expansion coefficient of shock position
$\overline{a}_k$	kth normalized expansion coefficient of shock position
b_k	kth additional expansion coefficient of shock position (weak shock)
$\overline{b}_k$	kth normalized additional expansion coefficient of shock position (weak shock)
c	speed of sound
$\boldsymbol{e}_i$	ith eigenvector of the Euler differential equations in the (η, θ) coordinates
f	arbitrary function
i	unknown exponent in shock position expansion
k	arbitrary integer
n	exponent in Guderley's solution
r	radial coordinate of a point
t	time
u	velocity

Roman characters, upper case

C	integration constant
D_f	denominator of f
N_f	numerator of f
P	pressure
$\boldsymbol{P}_k$	node k in the characteristic program
R_s	radial position of shock
U_s	velocity of shock

$\overline{U}_{\rm s}$ normalized velocity of shock ($\overline{U}_{\rm s} = \frac{U_{\rm s}}{c_{\rm I}}$)

$\tilde{U}_{\rm s}$ non-singular normalization of the shock velocity ($\tilde{U}_{\rm s} = \theta\frac{U_{\rm s}}{c_{\rm I}}$)

Greek characters

α time scaling constant in strong shock expansion

β constant

γ ratio of specific heats

ϵ number that can take the values 1 or -1

η non-dimensional variable ($\eta = \frac{R_{\rm s}}{r}$)

θ non-dimensional variable ($\theta = \frac{c_{\rm I}t}{R_{\rm s}}$)

λ_i ith eigenvalue of the Euler differential equations in the (η, θ) coordinates

ν symmetry of the problem (1 for planar, 2 for axisymmetric, and 3 for spherical)

ξ intermediate variable for strong shock expansion

π intermediate variable for strong shock expansion

ρ density

σ intermediate variable for strong shock expansion

τ characteristic time

$\overline{\tau}_{\rm s}$ scaled characteristic time used in the strong shock expansion

$\overline{\tau}_{\rm w}$ scaled characteristic time used in the weak shock expansion

ϕ intermediate variable for strong shock expansion

ψ intermediate variable for strong shock expansion

ω intermediate variable for strong shock expansion

Subscripts

1 relative to the first expansion term

2 relative to the second expansion term

3 relative to the third expansion term

I relative to region I

II relative to region II

III	relative to region III
IV	relative to region IV
s	relative to shock

Superscripts

l	relative to the limit for η tending to infinity (region IV)
s	relative to the shock between regions I and II
T	transpose of a matrix
(-1)	inverse of a function
$\star$	relative to the condition on shock trajectory
$*$	relative to the singular point in region II
$\pm$	relative to either the incoming or the reflected shock case
$-$	relative to the incoming shock case (regions I and II)
$+$	relative to the reflected shock case (regions III and IV)

Introduction

The problem of an imploding shock wave is important from a fundamental gas-dynamical point of view, and has important applications ranging from detonation and fusion initiation to the destruction of kidney stones. It was first investigated by Guderley [19]. He considered a cylindrical or spherical shock wave, initially at a very large radius and propagating inward through a perfect gas at rest and reflecting from the axis or center. As the shock approaches the center, it accelerates.

Guderley considered only the case where the shock is already so intense that the strong form of the shock jump relations apply. For that case he found a similarity solution, in which the shock radius is obtained as a power of the time relative to the time at which it reaches the center, with an exponent that is smaller than one, so that the shock strength becomes infinite at the center. The value of the exponent is the same for the incoming and reflected waves. It has since been recalculated with greater accuracy than Guderley's by several researchers. In 1988, Hafner [20] derived the equations in Lagrangian coordinates and used power series to solve these. Doing so, he was able to find the exponent value with a very high number of significant digits.

The problem was also studied by Chester [21], Chisnell [22], and Whitham [23] with approximate methods, specifically geometrical shock dynamics. In their solutions, the exponent in the expression for the Mach number as a function of shock radius for the spherical case is exactly twice that for the cylindrical case. This approximate result differs from the exact one by less than one percent. The method is quite simple and fairly accurate.

More recently, Chisnell [24] described the imploding shock problem analytically, along with the flow generated behind it, by making a few analytical assumptions. The exponent values that he found, using approximate equations, are fairly close to their exact values,

which indicates that his descriptions are valid. Chisnell also investigated the converging shock behavior when the specific heat ratio, γ, tends to 1 or to infinity.

Finally, Lee used a quasi-similar approximation and was able to find the approximate flow behavior even for finite Mach numbers [25]. His solution agrees very well with the exact solution.

Although suggested by Guderley in 1942, the power solution was, to our knowledge, never extended as a power series. This power series would allow for an increased range of acceptable Mach numbers, allowing the solution to remain valid a bit farther from the point of reflection.

The aim of the present work is to revisit the derivation of the Guderley solution, and to obtain a power series solution both for the incoming and reflected shocks, in which the Guderley solution is the first term. Such a solution would apply in and near the strong-shock limit. Also, we seek a series solution for the case of an initially infinitesimally weak shock at initially infinite radius as it propagates inward. Furthermore, we also aim to compute the flow field in this case using the method of characteristics. Finally, we want to compare the results with numerical simulations.

In the following chapters, we will first define accurately the imploding-reflecting shock problem. The problem will then be posed, dimensional analysis will be used to guide the solution strategy, and finally, the general equations will be given (Chapter 1). Then the Guderley solution will be explained and two additional terms will be added. An expansion will also be formed for a very weak shock located very far from the reflection point (Chapter 2). A special characteristic algorithm, designed to find the complete imploding shock solution from infinity to the origin, will be explained (Chapter 3). Finally, some comparative results, between expansions, characteristic solutions, and an Euler solver, will be presented (Chapter 4).

Chapter 1

Problem Definition

This chapter is divided into three parts. In the first part, the general notations used in the present work are introduced. In the second part, some dimensional analysis is performed to understand the form of the solution one can expect. And finally in the last part, the basic equations are introduced.

1.1 General Notations

Consider the one-dimensional problem of a shock propagating through an inviscid perfect gas at rest, from infinity, and reflecting at the origin. This shock can have either spherical ($\nu = 3$), cylindrical ($\nu = 2$), or planar symmetry ($\nu = 1$). In the last case, we can imagine the problem as being a shock reflecting from a wall. Guderley defines the problem such that it has no characteristic length; the shock comes from infinity and reflects towards infinity [19].

The independent variables are the radius r and the time t. The shock position is given by $R_{\rm s}(t)$ and its velocity is $U_{\rm s}(t)$. The origin of the independent variables is such that the shock reflects when $r = 0$ and $t = 0$, *i.e.*,

$$R_{\rm s}(0) = 0. \tag{1.1}$$

In this configuration, the incoming part of the shock is characterized by $t < 0$ and the reflected part, by $t > 0$. The medium is a perfect gas with a ratio of specific heats γ, and the flow upstream of the incoming shock is at rest with pressure $P_{\rm I}$ and density $\rho_{\rm I}$ (see

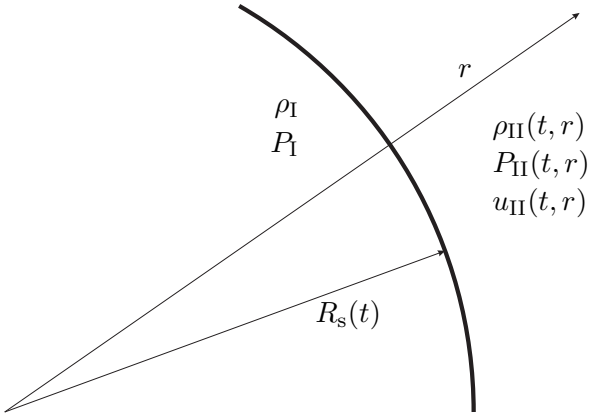

Figure 1.1: Problem notations for the incoming shock.

Figure 1.1). Note that the notation in this work is slightly different from that chosen by Guderley [19], because it is more suited to the improvements that are made.

The entire problem can be divided into four separate regions. Region I is the undisturbed flow ($t < 0$ and $r < R_{\mathrm{s}}(t)$). In this region, the density and the pressure are constant and the flow is at rest. Region II corresponds to the flow behind the incoming shock ($t < 0$ and $r > R_{\mathrm{s}}(t)$). Region III corresponds to the flow upstream of the reflected shock ($t > 0$ and $r > R_{\mathrm{s}}(t)$). And, finally, region IV corresponds to the flow downstream of the reflected shock ($t > 0$ and $r < R_{\mathrm{s}}(t)$).

Figure 1.2 shows these four regions, as well as the shapes of the different families of characteristics. First a particle trajectory is shown by the thin solid curves. In region I, the flow is at rest and the particle trajectories are just lines of constant r. After the incoming shock, the gas flows towards the center but slows down in time due to the accumulation of mass. After the reflected shock, the flow is directed away from the center and slows down to eventually come to rest when the pressure becomes constant in the whole domain. The second family of characteristics is defined by $\frac{dr}{dt} = u + c$ and is represented by dotted curves. In region I, these are straight lines representing waves moving at the speed of sound. After the incoming shock, they are deflected toward the center and they stop at the shock. In fact, the second family of characteristics in region IV represents waves that travel faster than the shock and stop when they reach it. Finally, the last family of characteristics is defined by $\frac{dr}{dt} = u - c$ and is represented by dashed curves. In region I, these characteristics

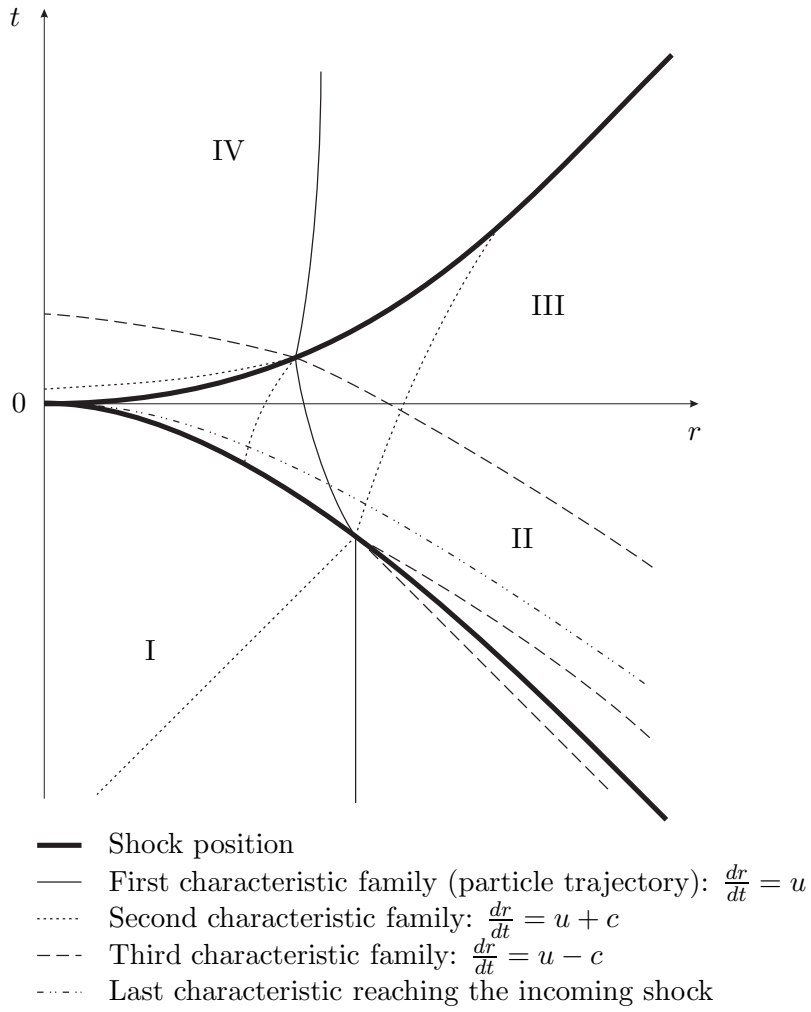

Figure 1.2: Sketch of the r–t diagram of the problem. The shock position is represented by the thick curves. The three different characteristic families are represented as well: $\frac{dr}{dt} = u$ (solid curves), $\frac{dr}{dt} = u + c$ (dotted curves), and $\frac{dr}{dt} = u - c$ (dashed curves), where u and c are the local velocity and speed of sound of the flow, respectively.

are also straight lines that describe waves moving at the speed of sound. They stop at the incoming shock since, in region II, they travel faster than the shock. The third family of characteristics in region II or III reaching the reflected shock is just deflected by the reflected shock. Note that the particular characteristic that reaches the shock at $t = 0$ is of particular importance since it is the boundary of the incoming shock influence domain. This characteristic leads to singularities in the equations as explained in later chapters. Note that since, in region III, no information comes from the reflected shock, regions II and III could be computed together. The notations are such that $f_{\rm I}$ refers to the value of f in region I, $f_{\rm II}$ to the value of f in region II, *etc.*

1.2 Dimensional Analysis

The important variables of the problem were introduced in Section 1.1. First, ν is the constant that defines which type of symmetry we are considering. Second, $\rho_{\rm I}$, $P_{\rm I}$ define the flow properties of the undisturbed region (region I), and γ is the specific heat ratio of the perfect gas. Third, t and r are the independent variables of the problem. And finally, the radius of the shock is given by $R_{\rm s}$.

According to Buckingham's Pi Theorem, since we have seven variables, we can form four independent non-dimensional numbers. We can take for example the following non-dimensional parameters

$$\nu,\ \gamma,\ \theta = \frac{c_{\rm I} t}{R_{\rm s}},\ \eta = \frac{R_{\rm s}}{r},$$

where $c_{\rm I}$ is the speed of sound of the undisturbed flow ($c_{\rm I} = \sqrt{\frac{\gamma P_{\rm I}}{\rho_{\rm I}}}$). These four non-dimensional variables are enough to describe the complete solution of the problem. This means that under the coordinates (θ, η), we may expect a universal solution for a fixed γ and a given symmetry. The density, pressure, and velocity can be expressed as

$$\rho = \rho_{\rm I} \overline{\rho}(\nu, \gamma, \theta, \eta)\,, \tag{1.2}$$

$$P = P_{\rm I} \overline{P}(\nu, \gamma, \theta, \eta)\,, \tag{1.3}$$

$$u = c_{\rm I} \overline{u}(\nu, \gamma, \theta, \eta)\,. \tag{1.4}$$

The differential equations that define the universal solution in these coordinates are derived later in Section 3.

We can also investigate the shock motion by introducing the velocity of the shock $U_\mathrm{s} = \frac{dR_\mathrm{s}}{dt}$. Since the shock is located at $\eta = 1$, we have

$$U_\mathrm{s} = c_\mathrm{I} K^{(-1)}(\nu, \gamma, \theta) \tag{1.5}$$

where $K^{(-1)}$ is the inverse function of K. This last expression can be rewritten as

$$\theta = K\left(\nu, \gamma, \overline{U}_\mathrm{s}\right), \tag{1.6}$$

where K is an unknown function and where the normalized velocity $\overline{U}_\mathrm{s}$ is defined as

$$\overline{U}_\mathrm{s} = \frac{U_\mathrm{s}}{c_\mathrm{I}}. \tag{1.7}$$

This equation is very useful to compare results since it does not involve any kind of initial conditions on the shock position. However, it is not very convenient to make direct predictions of the shock position. In fact, Equation 1.6 involves three variables (t, $R_\mathrm{s}(t)$, and $U_\mathrm{s}(t)$), and is a non-linear differential equation for $R_\mathrm{s}(t)$. This can be seen if we write the equation as

$$\frac{c_\mathrm{I} t}{R_\mathrm{s}(t)} = K\left(\nu, \gamma, \frac{1}{c_\mathrm{I}} \frac{dR_\mathrm{s}(t)}{dt}\right). \tag{1.8}$$

To find a more suitable equation, we drop the independent variable t and force the condition that the shock goes through $R_\mathrm{s}^\star$ with a normalized velocity $\overline{U}_\mathrm{s}^\star$. We now have five non-dimensional parameters that we can choose to be

$$\nu,\ \gamma,\ \frac{R_\mathrm{s}}{R_\mathrm{s}^\star},\ \overline{U}_\mathrm{s},\ \overline{U}_\mathrm{s}^\star.$$

An equation linking these parameters can be written

$$\frac{R_\mathrm{s}}{R_\mathrm{s}^\star} = f\left(\nu, \gamma, \overline{U}_\mathrm{s}, \overline{U}_\mathrm{s}^\star\right), \tag{1.9}$$

where we have the condition that

$$1 = f\left(\nu, \gamma, \overline{U}_{\mathrm{s}}^{\star}, \overline{U}_{\mathrm{s}}^{\star}\right). \tag{1.10}$$

To simplify the equation even further, assume that we know the normalized velocity of the shock at another location ($\overline{U}_{\mathrm{s}} = \overline{U}_{\mathrm{s}}^{\star\star}$ at $r = R_{\mathrm{s}}^{\star\star}$). We have that

$$f\left(\nu, \gamma, \overline{U}_{\mathrm{s}}, \overline{U}_{\mathrm{s}}^{\star\star}\right) = \frac{R_{\mathrm{s}}}{R_{\mathrm{s}}^{\star\star}} = \frac{R_{\mathrm{s}}^{\star}}{R_{\mathrm{s}}^{\star\star}} f\left(\nu, \gamma, \overline{U}_{\mathrm{s}}, \overline{U}_{\mathrm{s}}^{\star}\right) = g\left(\nu, \gamma, \overline{U}_{\mathrm{s}}^{\star}, \overline{U}_{\mathrm{s}}^{\star\star}\right) f\left(\nu, \gamma, \overline{U}_{\mathrm{s}}, \overline{U}_{\mathrm{s}}^{\star}\right), \tag{1.11}$$

where we have defined the function g such that

$$\frac{R_{\mathrm{s}}^{\star}}{R_{\mathrm{s}}^{\star\star}} = g\left(\nu, \gamma, \overline{U}_{\mathrm{s}}^{\star}, \overline{U}_{\mathrm{s}}^{\star\star}\right). \tag{1.12}$$

Equation 1.11 is always true and in particular for $\overline{U}_{\mathrm{s}} = \overline{U}_{\mathrm{s}}^{\star}$,

$$f\left(\nu, \gamma, \overline{U}_{\mathrm{s}}^{\star}, \overline{U}_{\mathrm{s}}^{\star\star}\right) = g\left(\nu, \gamma, \overline{U}_{\mathrm{s}}^{\star}, \overline{U}_{\mathrm{s}}^{\star\star}\right) f\left(\nu, \gamma, \overline{U}_{\mathrm{s}}^{\star}, \overline{U}_{\mathrm{s}}^{\star}\right) = g\left(\nu, \gamma, \overline{U}_{\mathrm{s}}^{\star}, \overline{U}_{\mathrm{s}}^{\star\star}\right), \tag{1.13}$$

where we have used the condition in Equation 1.10. Combining Equations 1.9, 1.11, and 1.13, we obtain

$$\frac{R_{\mathrm{s}}}{R_{\mathrm{s}}^{\star}} = \frac{f\left(\nu, \gamma, \overline{U}_{\mathrm{s}}, \overline{U}_{\mathrm{s}}^{\star\star}\right)}{f\left(\nu, \gamma, \overline{U}_{\mathrm{s}}^{\star}, \overline{U}_{\mathrm{s}}^{\star\star}\right)}. \tag{1.14}$$

This last equation is valid for any $\overline{U}_{\mathrm{s}}^{\star\star}$ that can be arbitrarily chosen the same for any problem. In the present work, it was chosen that $\overline{U}_{\mathrm{s}}^{\star\star} = -2$. A new function F can now be defined such that

$$F\left(\nu, \gamma, \overline{U}_{\mathrm{s}}\right) = f\left(\nu, \gamma, \overline{U}_{\mathrm{s}}, -2\right), \tag{1.15}$$

which finally leads to the following relation:

$$\frac{R_{\mathrm{s}}}{R_{\mathrm{s}}^{\star}} = \frac{F\left(\nu, \gamma, \overline{U}_{\mathrm{s}}\right)}{F\left(\nu, \gamma, \overline{U}_{\mathrm{s}}^{\star}\right)}, \tag{1.16}$$

with

$$F(\nu, \gamma, -2) = 1. \tag{1.17}$$

This last relation is particularly interesting since it means that all the curves (R_s, $\overline{U}_\mathrm{s}$) can be collapsed onto a single one using an appropriate scaling factor. In other words, F can be plotted once, and for all different cases. The R_s axis is just scaled so that the curve passes through ($R_\mathrm{s}^\star$, $\overline{U}_\mathrm{s}^\star$). Introducing the characteristic time τ such that

$$\tau = \frac{R_\mathrm{s}^\star}{c_\mathrm{I} F\left(\nu, \gamma, \overline{U}_\mathrm{s}^\star\right)}, \tag{1.18}$$

we can rewrite Equation 1.16 as

$$\frac{R_\mathrm{s}}{c_\mathrm{I}\tau} = F\big(\nu, \gamma, \overline{U}_\mathrm{s}\big)\,. \tag{1.19}$$

According to the definition of the function F, we can note that $c_\mathrm{I}\tau$ is the radius at which the incoming shock has a Mach number of 2. Mathematically, no initial conditions can exist since the shock is initiated at infinity; however, we can imagine two cases in which the infinitely weak initial shock has different strengths at the same very large value of R_s, which means that these two cases will lead to different solutions in the full domain. We can therefore distinguish the different cases by the value of τ, which is then equivalent to artificial initial conditions.

We can go a bit further and define the inverse function $F^{(-1)}$ such that

$$\overline{U}_\mathrm{s} = F^{(-1)}\left(\nu, \gamma, \frac{R_\mathrm{s}}{c_\mathrm{I}\tau}\right). \tag{1.20}$$

Starting from the definition of $\overline{U}_\mathrm{s}$, and using the fact that τ is constant, we can write that

$$\overline{U}_\mathrm{s} = \frac{1}{c_\mathrm{I}}\frac{dR_\mathrm{s}}{dt} = \frac{d\frac{R_\mathrm{s}}{c_\mathrm{I}\tau}}{d\frac{t}{\tau}}, \tag{1.21}$$

which, when used with Equation 1.20, leads to a differential equation for $\frac{R_\mathrm{s}}{c_\mathrm{I}\tau}$ in terms of $\frac{t}{\tau}$:

$$\frac{d\frac{R_\mathrm{s}}{c_\mathrm{I}\tau}}{d\frac{t}{\tau}} = F^{(-1)}\left(\nu, \gamma, \frac{R_\mathrm{s}}{c_\mathrm{I}\tau}\right). \tag{1.22}$$

This expression can be rewritten as

$$\frac{d\frac{R_s}{c_I\tau}}{F^{(-1)}\left(\nu,\gamma,\frac{R_s}{c_I\tau}\right)} = d\frac{t}{\tau}. \tag{1.23}$$

We can define a function G such that

$$G^{(-1)}(\nu,\gamma,x) = \int \frac{dx}{F^{(-1)}(\nu,\gamma,x)}, \tag{1.24}$$

$$G^{(-1)}(\nu,\gamma,0) = 0. \tag{1.25}$$

Solving Equation 1.23, we can find the general expression of R_s in terms of t and of the imposed conditions:

$$R_s = c_I\tau\, G\left(\nu,\gamma,\frac{t}{\tau}\right). \tag{1.26}$$

The series expansions will be written in the same form as Equation 1.26. The functions F, G and K are very important and will be used to make comparisons between the different series expansions, the solution from a characteristics program and Euler computations (Section 4.4).

1.3 Problem Equations

The gas properties in each of the four regions are continuous. Since we consider an inviscid perfect gas, the Euler equations can be used. These are

$$\frac{\partial\rho}{\partial t} + u\frac{\partial\rho}{\partial r} + \rho\frac{\partial u}{\partial r} + \frac{(\nu-1)\,\rho u}{r} = 0, \tag{1.27}$$

$$\frac{\partial u}{\partial t} + u\frac{\partial u}{\partial r} + \frac{1}{\rho}\frac{\partial P}{\partial r} = 0, \tag{1.28}$$

$$\frac{\partial P}{\partial t} + u\frac{\partial P}{\partial r} - \frac{\gamma P}{\rho}\left(\frac{\partial\rho}{\partial t} + u\frac{\partial\rho}{\partial r}\right) = 0, \tag{1.29}$$

where ρ, u, and P are the density, the flow velocity, and the pressure, respectively. In addition, the regions are connected together either by shock jump conditions or by continuity. Between regions I and II, we have shock jump conditions with an upstream region at rest,

i.e.,

$$\rho_{\mathrm{II}}(t, R_{\mathrm{s}}(t)) = \rho_{\mathrm{I}} \frac{\gamma + 1}{\gamma - 1 + 2\left(\frac{c_{\mathrm{I}}}{U_{\mathrm{s}}(t)}\right)^2}, \tag{1.30}$$

$$P_{\mathrm{II}}(t, R_{\mathrm{s}}(t)) = P_{\mathrm{I}} \frac{2\gamma\left(\frac{U_{\mathrm{s}}(t)}{c_{\mathrm{I}}}\right)^2 + 1 - \gamma}{\gamma + 1}, \tag{1.31}$$

$$u_{\mathrm{II}}(t, R_{\mathrm{s}}(t)) = \frac{2U_{\mathrm{s}}(t)}{\gamma + 1}\left[1 - \left(\frac{c_{\mathrm{I}}}{U_{\mathrm{s}}(t)}\right)^2\right]. \tag{1.32}$$

Regions II and III are connected by imposing that the values remain continuous across their common boundary, *i.e.*,

$$\rho_{\mathrm{III}}(0, r) = \rho_{\mathrm{II}}(0, r)\,, \tag{1.33}$$

$$P_{\mathrm{III}}(0, r) = P_{\mathrm{II}}(0, r)\,, \tag{1.34}$$

$$u_{\mathrm{III}}(0, r) = u_{\mathrm{II}}(0, r)\,. \tag{1.35}$$

And finally, regions III and IV are also connected by shock jump conditions, but this time, the upstream flow is not at rest anymore, *i.e.*,

$$\rho_{\mathrm{IV}}(t, R_{\mathrm{s}}(t)) = \rho_{\mathrm{III}}(t, R_{\mathrm{s}}(t)) \frac{\gamma + 1}{\gamma - 1 + 2\left[\frac{c_{\mathrm{III}}(t, R_{\mathrm{s}}(t))}{U_{\mathrm{s}}(t) - u_{\mathrm{III}}(t, R_{\mathrm{s}}(t))}\right]^2}, \tag{1.36}$$

$$P_{\mathrm{IV}}(t, R_{\mathrm{s}}(t)) = P_{\mathrm{III}}(t, R_{\mathrm{s}}(t)) \frac{2\gamma\left[\frac{U_{\mathrm{s}}(t) - u_{\mathrm{III}}(t, R_{\mathrm{s}}(t))}{c_{\mathrm{III}}(t, R_{\mathrm{s}}(t))}\right]^2 + 1 - \gamma}{\gamma + 1}, \tag{1.37}$$

$$u_{\mathrm{IV}}(t, R_{\mathrm{s}}(t)) = U_{\mathrm{s}}(t) + \left[u_{\mathrm{III}}(t, R_{\mathrm{s}}(t)) - U_{\mathrm{s}}(t)\right] \frac{\gamma - 1 + 2\left[\frac{c_{\mathrm{III}}(t, R_{\mathrm{s}}(t))}{U_{\mathrm{s}}(t) - u_{\mathrm{III}}(t, R_{\mathrm{s}}(t))}\right]^2}{\gamma + 1}. \tag{1.38}$$

Now that all the regions are connected together, the only additional condition is that the flow has no velocity at $r = 0$, *i.e.*,

$$u_{\mathrm{IV}}(t, 0) = 0. \tag{1.39}$$

There are no initial conditions since the shock starts infinitely far from the origin and Equations 1.27 to 1.39 completely define the problem.

Chapter 2

Series Expansion Solutions

To obtain a simple solution, it is useful to find the limiting behaviors of the shock in the form of a series. Guderley obtained the first term of the expansion series solution close to the origin, for $r \ll c_1\tau$ (or equivalently, for $M_s \gg 1$). In the next paragraphs, we will first transform the equations to make them more suitable for solving the expansion problems (Section 2.1). Guderley's solution will then be examined (Section 2.2) and extended with two additional terms (Section 2.3). Expansions will also be formed for the weak shock case, *i.e.*, for $r \gg c_1\tau$, or for $M_s - 1 \ll 1$ (Section 2.4). These can be very useful as initial conditions if we use a numerical method to find the solution in the whole domain. Finally, we will summarize briefly what we have found (Section 2.5).

2.1 Initial Change of Variables

Looking at Figure 1.2, we see that the four regions have complicated shapes that are not known *a priori*. It is much easier to transform these regions into regions with fixed shapes to know exactly where the shock jump conditions have to be applied. This can be performed easily by making the change of variables

$$(t,\, r) \rightarrow (\eta,\, r)\,,$$

where

$$\eta = \frac{R_s(t)}{r}. \tag{2.1}$$

The shock jump conditions now occur at $\eta = 1$ and under this change of variables, Figure 1.2 is transformed into Figure 2.1. Note that the transformation is not a bijection,[1] this is the reason why Figure 2.1 is composed of two parts, the first for $t < 0$ and the second for $t > 0$. To facilitate further calculations, the velocity of the shock is now expressed in terms of its position instead of in terms of time directly ($U_{\mathrm{s}}(R_{\mathrm{s}}(t))$ instead of $U_{\mathrm{s}}(t)$). Using these definitions, we can also transform the derivatives to

$$\begin{aligned}\frac{\partial}{\partial t} &= \frac{\partial \eta}{\partial t}\frac{\partial}{\partial \eta} \\ &= \frac{U_{\mathrm{s}}(\eta r)}{r}\frac{\partial}{\partial \eta}, \qquad (2.2)\\ \frac{\partial}{\partial r} &= \frac{\partial}{\partial r} + \frac{\partial \eta}{\partial r}\frac{\partial}{\partial \eta} \\ &= \frac{\partial}{\partial r} - \frac{\eta}{r}\frac{\partial}{\partial \eta}. \qquad (2.3)\end{aligned}$$

Using these expressions, we can write the Euler equations in terms of the new variables,

$$r\frac{\partial(\rho u)}{\partial r} - \eta\frac{\partial(\rho u)}{\partial \eta} + U_{\mathrm{s}}(\eta r)\frac{\partial \rho}{\partial \eta} + (\nu - 1)\rho u = 0, \qquad (2.4)$$

$$\rho u r\frac{\partial u}{\partial r} + \rho\left[U_{\mathrm{s}}(\eta r) - \eta u\right]\frac{\partial u}{\partial \eta} + r\frac{\partial P}{\partial r} - \eta\frac{\partial P}{\partial \eta} = 0, \qquad (2.5)$$

$$ur\frac{\partial}{\partial r}\left(\frac{P}{\rho^{\gamma}}\right) + \left[U_{\mathrm{s}}(\eta r) - \eta u\right]\frac{\partial}{\partial \eta}\left(\frac{P}{\rho^{\gamma}}\right) = 0. \qquad (2.6)$$

2.2 Guderley's Solution

Guderley's work was focused on the region close to $r = 0$ ($r \ll c_{\mathrm{I}}\tau$). In that region, it can be assumed that between regions I and II, the strong shock jump conditions are valid [19]. Note that this assumption cannot be made for the reflected shock between III and IV. In fact, although the reflected shock velocity tends to infinity when r tends to 0, its Mach number is finite since the speed of sound tends to infinity as well. Furthermore, Guderley hypothesized that under the strong shock assumption, the shock position can be written as

[1] A transformation that is one-to-one and onto.

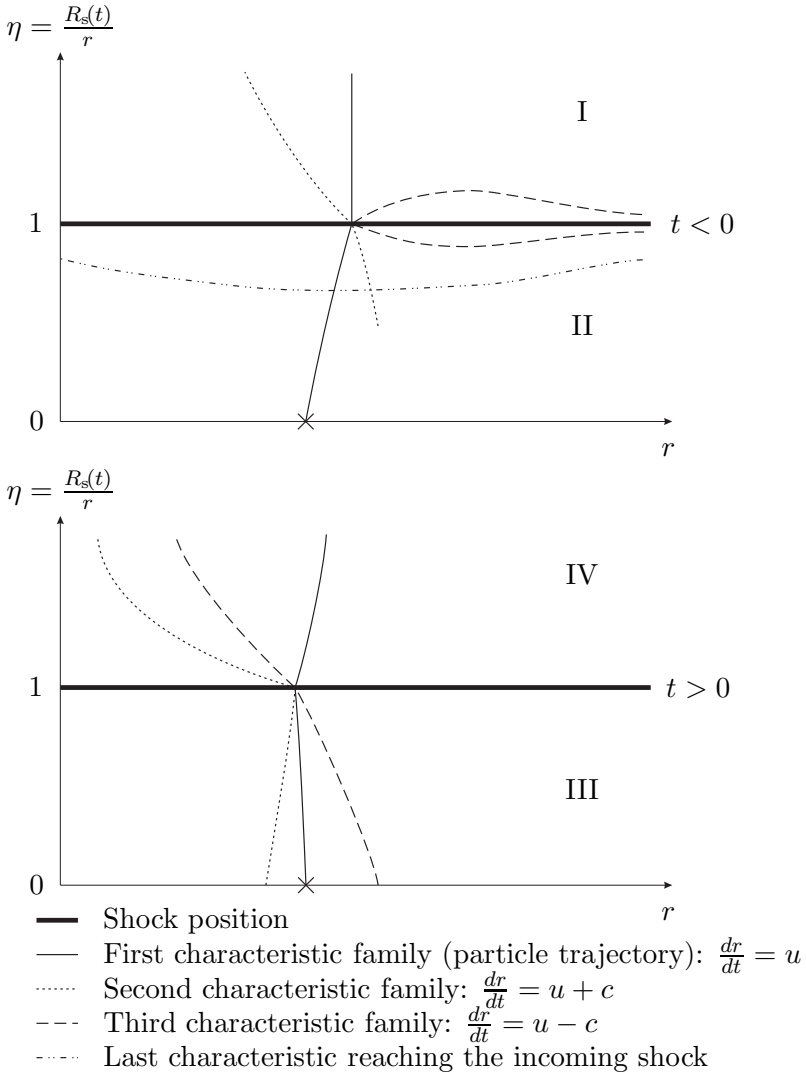

Figure 2.1: Sketch of the η–r diagram for the problem. The shock position is represented by the thick lines. The three different kinds of characteristics are shown as well: $\frac{dr}{dt} = u$ (solid curves), $\frac{dr}{dt} = u + c$ (dotted curves), and $\frac{dr}{dt} = u - c$ (dashed curves), where u and c are the local velocity and speed of sound of the flow, respectively. The crosses correspond to the same point in the (r, t) domain. Note the particular shape of the last characteristic reaching the incoming shock. In the η–r diagram, it reaches $r = 0$ at a finite η that is different from 1, this leads to a singularity in the domain.

proportional to time to a power $n^{\pm}$. Using the notations introduced in Equation 1.26, this means that

$$R_{\mathrm{s}}(t) = c_{\mathrm{I}}\tau\beta^{\pm}\left(\frac{|t|}{\tau}\right)^{n^{\pm}}, \tag{2.7}$$

where $\beta^{\pm}$ is a constant that takes the value β^{-} in the incoming shock case, and β^{+} in the reflected shock case. In all the following sections, the superscript $\pm$ refers to a value that has different values in the incoming and in the reflected case, and the superscripts $-$ and $+$ refer to the incoming and to the reflected cases, respectively. To simplify the expressions in later sections, it is more convenient to write Equation 2.7 as

$$R_{\mathrm{s}}(t) = c_{\mathrm{I}}\overline{\tau}_{\mathrm{s}}\left(\frac{t}{\alpha^{\pm}\overline{\tau}_{\mathrm{s}}}\right)^{n^{\pm}}, \tag{2.8}$$

where $\alpha^{\pm}$ is a constant that is chosen to be -1 for the incoming shock, and that has an unknown constant positive value (α^{+}) for the reflected shock, and where

$$\overline{\tau}_{\mathrm{s}} = \left(\beta^{-}\right)^{\frac{1}{1-n^{-}}}\tau. \tag{2.9}$$

The exponent $n^{\pm}$ is an unknown constant and, based on the work so far, its value is not necessarily the same in the incoming and in the reflected cases. Its value lies between 0 and 1 since $R_{\mathrm{s}}(0) = 0$ and the speed of the shock tends to infinity when t tends to 0. Once again, note that although the results are the same, this notation differs from that of Guderley. From Equation 2.8, we can find the shock velocity, which is

$$\begin{aligned} U_{\mathrm{s}}(R_{\mathrm{s}}) &= c_{\mathrm{I}}\frac{n^{\pm}}{\alpha^{\pm}}\left(\frac{t(R_{\mathrm{s}})}{\alpha^{\pm}\overline{\tau}_{\mathrm{s}}}\right)^{n^{\pm}-1} \\ &= c_{\mathrm{I}}\frac{n^{\pm}}{\alpha^{\pm}}\left(\frac{R_{\mathrm{s}}}{c_{\mathrm{I}}\overline{\tau}_{\mathrm{s}}}\right)^{\frac{n^{\pm}-1}{n^{\pm}}}. \end{aligned} \tag{2.10}$$

Since the shock position will be valid only for $R_{\mathrm{s}} \ll c_{\mathrm{I}}\overline{\tau}_{\mathrm{s}}$, the solution that we obtain is only valid for small r. In addition, since the characteristics coming from the shock are only correct for small t (or small R_{s}), we find that the solution is only correct for $t \ll \overline{\tau}_{\mathrm{s}}$.

The method to solve this simplified problem will be discussed in the following sections.

New shock jump conditions can first be written and new variables can be introduced (Section 2.2.1). From the resulting equations, the problem can be solved for $n^{\pm}$ and then for $\alpha^{\pm}$ (Section 2.2.2).

2.2.1 Self-Similar Problem

We can first write the new shock jump conditions for the incoming case. These conditions are found by taking the leading term of Equations 1.30 through 1.32 when $U_{\rm s}(R_{\rm s})$ is much bigger than $c_{\rm I}$ (*i.e.*, for a very large incoming shock Mach number). These new conditions are

$$\rho_{\rm II}(1,r) = \rho_{\rm I}\frac{\gamma+1}{\gamma-1}, \tag{2.11}$$

$$\begin{aligned} P_{\rm II}(1,r) &= P_{\rm I}\frac{2\gamma}{\gamma+1}\left(\frac{U_{\rm s}(R_{\rm s})_{\eta=1}}{c_{\rm I}}\right)^2 \\ &= P_{\rm I}\frac{2\gamma\left(n^{\pm}\right)^2}{\gamma+1}\left(\frac{r}{c_{\rm I}\overline{\tau}_{\rm s}}\right)^{\frac{2\left(n^{\pm}-1\right)}{n^{\pm}}}, \end{aligned} \tag{2.12}$$

$$\begin{aligned} u_{\rm II}(1,r) &= \frac{2}{\gamma+1}U_{\rm s}(R_{\rm s})_{\eta=1} \\ &= -c_{\rm I}\frac{2n^{\pm}}{\gamma+1}\left(\frac{r}{c_{\rm I}\overline{\tau}_{\rm s}}\right)^{\frac{n^{\pm}-1}{n^{\pm}}}, \end{aligned} \tag{2.13}$$

where we used the fact that $(R_{\rm s})_{\eta=1} = r$ and that in the incoming case $\alpha^{-} = -1$. These equations suggest that we try a solution of the form

$$\rho(\eta,r) = \rho_{\rm I}\rho_1(\eta)\,, \tag{2.14}$$

$$P(\eta,r) = P_{\rm I}P_1(\eta)\left(\frac{n^{\pm}}{\alpha^{\pm}}\right)^2\left(\frac{r}{c_{\rm I}\overline{\tau}_{\rm s}}\right)^{\frac{2\left(n^{\pm}-1\right)}{n^{\pm}}}, \tag{2.15}$$

$$u(\eta,r) = c_{\rm I}u_1(\eta)\,\frac{n^{\pm}}{\alpha^{\pm}}\left(\frac{r}{c_{\rm I}\overline{\tau}_{\rm s}}\right)^{\frac{n^{\pm}-1}{n^{\pm}}}, \tag{2.16}$$

where $\rho_1(\eta)$, $P_1(\eta)$, and $u_1(\eta)$ are unknown functions of η only. The subscripts 1, 2, and 3 denote the first, second, and third terms in the expansions. Using this, Equations 2.4 to 2.6

become

$$\frac{\nu-\frac{1}{n^{\pm}}}{\eta}\rho_1(\eta)\,u_1(\eta)+\left[\eta^{-\frac{1}{n^{\pm}}}-u_1(\eta)\right]\rho_1'(\eta)-\rho_1(\eta)\,u_1'(\eta)=0, \tag{2.17}$$

$$\frac{1-\frac{1}{n^{\pm}}}{\eta}\left[2P_1(\eta)+\gamma\rho_1(\eta)\,u_1(\eta)^2\right]+\gamma\rho_1(\eta)\,u_1'(\eta)\left[\eta^{-\frac{1}{n^{\pm}}}-u_1(\eta)\right]-P_1'(\eta)=0, \tag{2.18}$$

$$\left[\rho_1(\eta)\,P_1'(\eta)-\gamma P_1(\eta)\,\rho_1'(\eta)\right]\left[\eta^{-\frac{1}{n^{\pm}}}-u_1(\eta)\right]+\frac{2-\frac{2}{n^{\pm}}}{\eta}\rho_1(\eta)\,u_1(\eta)\,P_1(\eta)=0, \tag{2.19}$$

where $'$ expresses the derivative of the variable with respect to η. Since these equations no longer depend on r, the assumed form of the variable is acceptable and the problem becomes self-similar. Note that these equations are valid in each of the three unknown regions (II, III, and IV). The shock jump conditions between regions I and II are now

$$\rho_{1,\mathrm{II}}(1)=\frac{\gamma+1}{\gamma-1}, \tag{2.20}$$

$$P_{1,\mathrm{II}}(1)=\frac{2\gamma}{\gamma+1}, \tag{2.21}$$

$$u_{1,\mathrm{II}}(1)=\frac{2}{\gamma+1}. \tag{2.22}$$

Once again, we did not assume anything yet about the value of the exponent $n^{\pm}$. Using the change of variables defined earlier, the continuity conditions between II and III (Equations 1.33 to 1.35) become

$$\rho_{1,\mathrm{III}}(0)=\rho_{1,\mathrm{II}}(0)\,, \tag{2.23}$$

$$P_{1,\mathrm{III}}(0)\left(\frac{n^+}{\alpha^+}\right)^2\left(\frac{r}{c_{\mathrm{I}}\overline{\tau}_{\mathrm{s}}}\right)^{\frac{2\left(n^+-1\right)}{n^+}}=P_{1,\mathrm{II}}(0)\left(n^-\right)^2\left(\frac{r}{c_{\mathrm{I}}\overline{\tau}_{\mathrm{s}}}\right)^{\frac{2\left(n^--1\right)}{n^-}}, \tag{2.24}$$

$$u_{1,\mathrm{III}}(0)\,\frac{n^+}{\alpha^+}\left(\frac{r}{c_{\mathrm{I}}\overline{\tau}_{\mathrm{s}}}\right)^{\frac{n^+-1}{n^+}}=-u_{1,\mathrm{II}}(0)\,n^-\left(\frac{r}{c_{\mathrm{I}}\overline{\tau}_{\mathrm{s}}}\right)^{\frac{n^--1}{n^-}}. \tag{2.25}$$

These conditions have to be satisfied for all r. This is only possible if we impose the

condition that $n^{\pm} = n^{+} = n^{-} = n$. The final continuity conditions between II and III are

$$\rho_{1,\mathrm{III}}(0) = \rho_{1,\mathrm{II}}(0)\,, \tag{2.26}$$

$$\frac{P_{1,\mathrm{III}}(0)}{\left(\alpha^{+}\right)^{2}} = P_{1,\mathrm{II}}(0)\,, \tag{2.27}$$

$$\frac{u_{1,\mathrm{III}}(0)}{\alpha^{+}} = -u_{1,\mathrm{II}}(0)\,. \tag{2.28}$$

It is also possible to write the shock jump conditions in the reflected case:

$$\rho_{1,\mathrm{IV}}(1) = \rho_{1,\mathrm{III}}(1)\,\frac{\gamma+1}{\gamma-1+2\frac{P_{1,\mathrm{III}}(1)}{\rho_{1,\mathrm{III}}(1)\left[1-u_{1,\mathrm{III}}(1)\right]^{2}}}, \tag{2.29}$$

$$P_{1,\mathrm{IV}}(1) = P_{1,\mathrm{III}}(1)\,\frac{2\gamma\frac{\rho_{1,\mathrm{III}}(1)\left[1-u_{1,\mathrm{III}}(1)\right]^{2}}{P_{1,\mathrm{III}}(1)}+1-\gamma}{\gamma+1}, \tag{2.30}$$

$$u_{1,\mathrm{IV}}(1) = 1 + \left[u_{1,\mathrm{III}}(1)-1\right]\frac{\gamma-1+2\frac{P_{1,\mathrm{III}}(1)}{\rho_{1,\mathrm{III}}(1)\left[1-u_{1,\mathrm{III}}(1)\right]^{2}}}{\gamma+1}. \tag{2.31}$$

Finally, since $n \leq 1$, the final condition (Equation 1.39) becomes

$$\lim_{\eta\to\infty} u_{1,\mathrm{IV}}(\eta) = 0. \tag{2.32}$$

All these last equations define a self-similar problem that gives a first approximation of the solution to the implosion problem around the point of reflection ($r \ll c_{\mathrm{I}}\overline{\tau}_{\mathrm{s}}$). Equations 2.17 to 2.19 form a non-linear system of differential equations that can be further simplified by applying a last change of variables:

$$\phi_1(\eta) = \eta^{\frac{1}{n}} u_1(\eta)\,, \tag{2.33}$$

$$\pi_1(\eta) = \frac{\eta^{\frac{2}{n}} P_1(\eta)}{\gamma\rho_1(\eta)\left[1-\phi_1(\eta)\right]}. \tag{2.34}$$

The system of equations (Equations 2.17 to 2.19) can be rewritten as follows:

$$\eta\frac{\rho_1'(\eta)}{\rho_1(\eta)}+\frac{\nu\phi_1(\eta)-\eta\phi_1'(\eta)}{1-\phi_1(\eta)}=0, \quad (2.35)$$

$$\pi_1(\eta)\left[2-\eta\frac{\rho_1'(\eta)}{\rho_1(\eta)}\right]+\eta\left[\phi_1'(\eta)-\pi_1'(\eta)\right]+\frac{n\eta\pi_1(\eta)\,\phi_1'(\eta)+n\phi_1(\eta)^2-\phi_1(\eta)}{n\left[1-\phi_1(\eta)\right]}=0, \quad (2.36)$$

$$\eta\left[(\gamma-1)\frac{\rho_1'(\eta)}{\rho_1(\eta)}-\frac{\pi_1'(\eta)}{\pi_1(\eta)}\right]+\frac{2-2n\phi_1(\eta)+n\eta\phi_1'(\eta)}{n\left[1-\phi_1(\eta)\right]}=0, \quad (2.37)$$

with the conditions 2.20 to 2.22, and 2.26 to 2.32, becoming

$$\rho_{1,\mathrm{II}}(1)=\frac{\gamma+1}{\gamma-1}, \quad (2.38)$$

$$\phi_{1,\mathrm{II}}(1)=\frac{2}{\gamma+1}, \quad (2.39)$$

$$\pi_{1,\mathrm{II}}(1)=\frac{2}{\gamma+1}, \quad (2.40)$$

$$\rho_{1,\mathrm{III}}(0)=\rho_{1,\mathrm{II}}(0)\,, \quad (2.41)$$

$$\lim_{\eta\to 0}\frac{\phi_{1,\mathrm{III}}(\eta)}{\phi_{1,\mathrm{II}}(\eta)}=-\alpha^+, \quad (2.42)$$

$$\lim_{\eta\to 0}\frac{\pi_{1,\mathrm{III}}(\eta)}{\pi_{1,\mathrm{II}}(\eta)}=\left(\alpha^+\right)^2, \quad (2.43)$$

$$\rho_{1,\mathrm{IV}}(1)=\rho_{1,\mathrm{III}}(1)\,\frac{(\gamma+1)\left[1-\phi_{1,\mathrm{III}}(1)\right]}{(\gamma-1)\left[1-\phi_{1,\mathrm{III}}(1)\right]+2\gamma\pi_{1,\mathrm{III}}(1)}, \quad (2.44)$$

$$\phi_{1,\mathrm{IV}}(1)=\frac{2-2\gamma\pi_{1,\mathrm{III}}(1)+(\gamma-1)\,\phi_{1,\mathrm{III}}(1)}{\gamma+1}, \quad (2.45)$$

$$\pi_{1,\mathrm{IV}}(1)=\frac{2-2\phi_{1,\mathrm{III}}(1)-(\gamma-1)\,\pi_{1,\mathrm{III}}(1)}{\gamma+1}, \quad (2.46)$$

$$\lim_{\eta\to\infty}\frac{\phi_{1,\mathrm{IV}}(\eta)}{\eta^{\frac{1}{n}}}=0. \quad (2.47)$$

In addition, we should note that, since $P_{1,\mathrm{IV}}(\eta)$ is not singular, $\frac{\pi_{1,\mathrm{IV}}(\eta)}{\eta^{\frac{2}{n}}}\left(1-\phi_{1,\mathrm{IV}}(\eta)\right)$ has to be finite even when η tends to infinity. The differential equation system can be rearranged

as

$$\phi_1'(\eta) = \frac{\phi_1(\eta)\left(1 - n\phi_1(\eta)\right) + \pi_1(\eta)\left(2 - 2n - n\gamma\nu\phi_1(\eta)\right)}{n\eta\left(1 - \phi_1(\eta) - \gamma\pi_1(\eta)\right)}, \tag{2.48}$$

$$\frac{\pi_1'(\eta)}{\pi_1(\eta)} = \frac{\begin{pmatrix} 2 + \left[\gamma - 2 - n\gamma + n\left(\nu - 2 + \gamma - \gamma\nu\right)\left(1 - \phi_1(\eta)\right)\right]\phi_1(\eta) + \\ n\gamma\pi_1(\eta)\left[\left(2 - \nu\right)\phi_1(\eta) - 2\right] \end{pmatrix}}{n\eta\left(1 - \phi_1(\eta)\right)\left(1 - \phi_1(\eta) - \gamma\pi_1(\eta)\right)}, \tag{2.49}$$

$$\frac{\rho_1'(\eta)}{\rho_1(\eta)} = \frac{2\left(1 - n\right)\pi_1(\eta) + \phi_1(\eta)\left[1 - n\nu + n\left(\nu - 1\right)\phi_1(\eta)\right]}{n\eta\left(1 - \phi_1(\eta)\right)\left(1 - \phi_1(\eta) - \gamma\pi_1(\eta)\right)}. \tag{2.50}$$

The problem can be solved by taking ϕ_1 as the independent variable instead of η. This leads finally to the system

$$\pi_1'(\phi_1) = \pi_1(\phi_1)\frac{\begin{pmatrix} 2 + \left[\gamma - 2 - n\gamma + n\left(\nu - 2 + \gamma - \gamma\nu\right)\left(1 - \phi_1\right)\right]\phi_1 + \\ n\gamma\pi_1(\phi_1)\left[\left(2 - \nu\right)\phi_1 - 2\right] \end{pmatrix}}{\left(1 - \phi_1\right)\left[\phi_1\left(1 - n\phi_1\right) + \pi_1(\phi_1)\left(2 - 2n - n\gamma\nu\phi_1\right)\right]}, \tag{2.51}$$

$$\frac{\eta'(\phi_1)}{\eta(\phi_1)} = \frac{n\left(1 - \phi_1 - \gamma\pi_1(\phi_1)\right)}{\phi_1\left(1 - n\phi_1\right) + \pi_1(\phi_1)\left(2 - 2n - n\gamma\nu\phi_1\right)}, \tag{2.52}$$

$$\frac{\rho_1'(\phi_1)}{\rho_1(\phi_1)} = \frac{2\left(1 - n\right)\pi_1(\phi_1) + \phi_1\left(1 - n\nu + n\left(\nu - 1\right)\phi_1\right)}{\left(1 - \phi_1\right)\left[\phi_1\left(1 - n\phi_1\right) + \pi_1(\phi_1)\left(2 - 2n - n\gamma\nu\phi_1\right)\right]}. \tag{2.53}$$

It is possible to find a first integral to this system:

$$\rho_1(\phi_1) = C\left[\frac{\pi_1(\phi_1)^n}{\eta(\phi_1)^2}\left(1 - \phi_1\right)^{\frac{2(1-n)+n\nu}{\nu}}\right]^{\frac{\nu}{n\nu(\gamma-1)-2(1-n)}}, \tag{2.54}$$

where C is a constant that takes a different value in each region. The problem is now relatively easy to solve since Equation 2.51 can first be considered alone to solve for $\pi_1(\phi_1)$. Then, Equation 2.52 can be integrated to find $\eta(\phi_1)$. $\rho_1(\phi_1)$ is obtained using the first integral that has just been found. Finally, note that since some variables are tending to 0, it is better to find P_1 and u_1 by integrating them rather than by using the variable definitions 2.33 and 2.34.

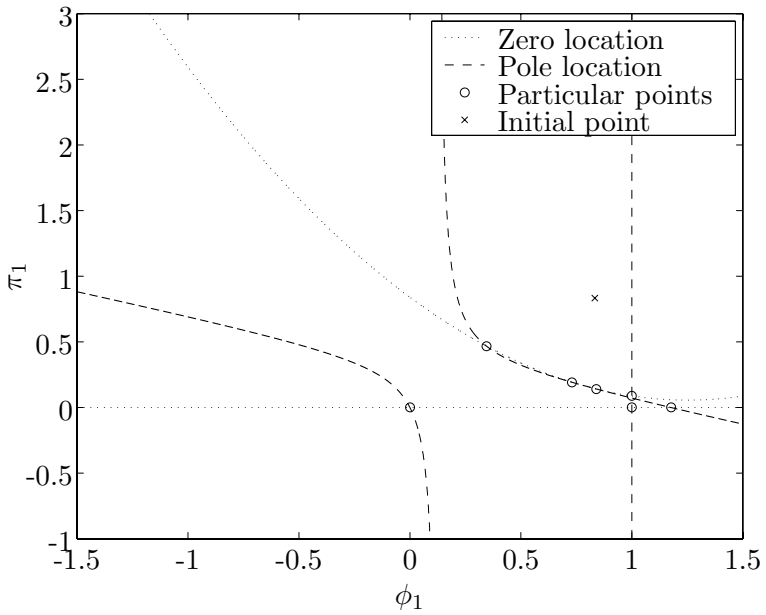

Figure 2.2: Zero and pole locations of the right-hand side of the $\pi_1'(\phi_1)$ equation for $\nu = 2$, $\gamma = 1.4$, and $n = 0.85$. The circles are the particular points that are intersections of the zero and the pole curves. The cross is the location of the initial point in region II.

2.2.2 Discussion and Solution of the Problem

First, consider the limiting values of the problem. In region II, just downstream of the shock, $\phi_{1,\mathrm{II}}$ and $\pi_{1,\mathrm{II}}$ are given exactly by the shock jump conditions (Equations 2.39 and 2.40). At the junction between II and III, ρ_1, P_1, and u_1 are continuous and finite, meaning that, since η tends to 0, ϕ_1 and π_1 tend also to 0 at the junction (see Equations 2.33 and 2.34). Finally in region IV, when η tends to infinity, $P_{1,\mathrm{IV}}$ needs to be finite, meaning that $\pi_{1,\mathrm{IV}}\,(1 - \phi_{1,\mathrm{IV}})$ needs to tend to infinity as well. In addition, ϕ_1 cannot change sign within a region, and $\pi_1\,(1 - \phi_1)$ remains always positive.

In the problem, ν and γ are fixed. For each value of n, we can plot, in the (ϕ_1, π_1) plane, the zeros and poles of the right-hand side of Equations 2.51 to 2.53. This is represented in Figures 2.2, 2.3, and 2.4 for the equations for $\pi_1'(\phi_1)$, $\log(\eta(\phi_1))'$, and $\log(\rho_1(\phi_1))'$, respectively. In these plots, the value of n was chosen arbitrarily to give a qualitative understanding of the nature of the problem.

In region II, the solution trajectory has to go from the initial point to (0, 0). Along that trajectory, the variables have to remain continuous. The only way this is possible is if the

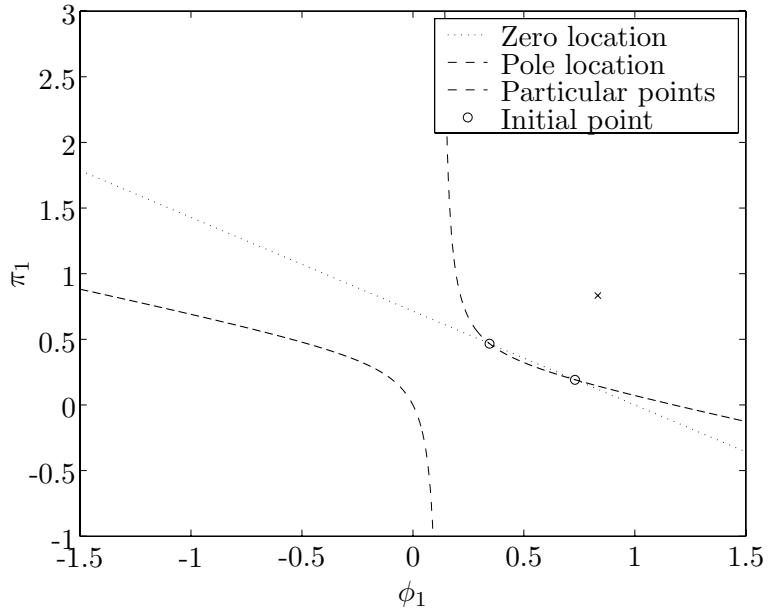

Figure 2.3: Zero and pole locations of the right-hand side of the $\log(\eta(\phi_1))'$ equation for $\nu = 2$, $\gamma = 1.4$, and $n = 0.85$. The circles are the particular points that are intersections of the zero and the pole curves. The cross is the location of the initial point in region II.

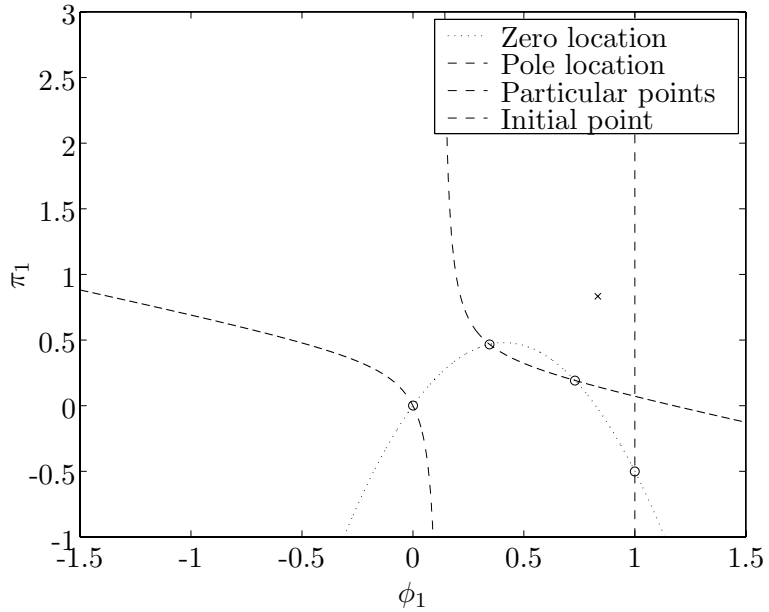

Figure 2.4: Zero and pole locations of the right-hand side of the $\log(\rho_1(\phi_1))'$ equation for $\nu = 2$, $\gamma = 1.4$, and $n = 0.85$. The circles are the particular points that are intersections of the zero and the pole curves. The cross is the location of the initial point in region II.

trajectory crosses a pole when it is also a zero. In fact, it can be shown that if it does not do so, the solution will not be smooth within the region. The only two acceptable points, (ϕ_1^*, π_1^*), where that occurs simultaneously in each of the three figures (Figures 2.2 to 2.4), are at

$$\phi_1^* = \frac{2(1-n) - \gamma(1-n\nu) + \sqrt{[2(1-n) - \gamma(1-n\nu)]^2 - 8(1-n)n\gamma(\nu-1)}}{2n\gamma(\nu-1)}, \quad (2.55)$$

$$\pi_1^* = \frac{1-\phi_1^*}{\gamma}, \quad (2.56)$$

and at

$$\phi_1^* = \frac{2(1-n) - \gamma(1-n\nu) - \sqrt{[2(1-n) - \gamma(1-n\nu)]^2 - 8(1-n)n\gamma(\nu-1)}}{2n\gamma(\nu-1)}, \quad (2.57)$$

$$\pi_1^* = \frac{1-\phi_1^*}{\gamma}. \quad (2.58)$$

For these intersections to exist, the square root has to be non-imaginary, which means that one of the two following conditions has to be satisfied:

$$n < \frac{4 + 2\gamma(\nu-3) + \gamma^2\nu - (2\gamma)^{\frac{3}{2}}(\nu-1)}{4 + \gamma[\nu(4+\gamma\nu) - 8]} \quad (2.59)$$

or

$$n > \frac{4 + 2\gamma(\nu-3) + \gamma^2\nu + (2\gamma)^{\frac{3}{2}}(\nu-1)}{4 + \gamma[\nu(4+\gamma\nu) - 8]}. \quad (2.60)$$

It is now conceptually easy to find n since it corresponds to the value for which the trajectory crosses one of the circled points. It is important to note that the singular point corresponds to a point on the limiting characteristic. That particular characteristic reaches $r = 0$ at $t = 0$ and is represented in characteristic sketches by a dash-dot-dot curve.

Consider now the trajectory in region IV. By examining Equation 2.51, we can find that the only way $\frac{\phi_{1,\mathrm{IV}}(\eta)}{\eta^{\frac{1}{n}}}$ can tend to infinity while keeping $\frac{\pi_{1,\mathrm{IV}}(\eta)}{\eta^{\frac{2}{n}}}(1 - \phi_{1,\mathrm{IV}}(\eta))$ finite, is such that the trajectory becomes tangent to the pole curve around its singularity (at $\phi_{1,\mathrm{IV}} = \frac{2(1-n)}{n\nu\gamma}$). This condition leads to a specific value of α^+ (α^- being -1).

To compute the results, the equations are integrated with a fourth-order scheme de-

scribed in Appendix A. In region II, the solution is integrated from the singularity towards the initial condition and a shooting method, iterating on n using a Newton-Raphson algorithm, is performed until the trajectory passes through the initial conditions. Then, it is integrated from the singularity towards (0, 0). The limit of the differential equations at the singularity is found using the L'Hôpital theorem. The limit of $\pi_1'(\phi_1)$ is found by solving the system

$$\pi_1'(\phi_1) = \frac{\frac{\partial N_{\pi_1'(\phi_1)}}{\partial \pi_1(\phi_1)}\pi_1'(\phi_1) + \frac{\partial N_{\pi_1'(\phi_1)}}{\partial \phi_1}}{\frac{\partial D_{\pi_1'(\phi_1)}}{\partial \pi_1(\phi_1)}\pi_1'(\phi_1) + \frac{\partial D_{\pi_1'(\phi_1)}}{\partial \phi_1}}, \tag{2.61}$$

when (ϕ_1, π_1) tends to (ϕ_1^*, π_1^*) and where the functions N_f and D_f represent the numerator and the denominator of f, respectively. After obtaining the complete solution in region II, we iterate on the value of $\phi_{1,\mathrm{IV}}$ just downstream of the shock. At each iteration, we start to integrate region IV from $\phi_{1,\mathrm{IV}} = \frac{2(1-n)}{n\nu\gamma}$ towards the chosen value of $\phi_{1,\mathrm{IV}}$ behind the shock. Using inverted shock jump conditions, we get these values upstream of the shock in region III and we integrate the equations towards (0, 0). If the $\phi_{1,\mathrm{IV}}$ and α^+ values are correctly chosen, P_1, ρ_1, and u_1 are continuous between II and III.

Each time a variable or its derivative tends to infinity, the corresponding differential equation is modified to avoid singularities. In other words, if the variable f behaves like $(C - \phi_1)^a$, the equation for $f'(\phi_1)$ is replaced by an equation for $\overline{f}'(\phi_1)$ where $f(\phi_1) = \overline{f}(\phi_1)\,(C - \phi_1)^a$. All the limiting behaviors of the variables are given in Appendix C. Finally, since, inside region III, $\pi_1'(\phi_1)$ can become infinite and then change sign, all equations are modified for part of the integration to use π_1 as the independent variable instead of ϕ_1.

As an example, Figures 2.5 and 2.6 represent two solution trajectories in the (ϕ_1, π_1) plane along with the corresponding pole and zero curves of the $\pi_1'(\phi_1)$ equation. Note that in Figure 2.6, $\pi_1'(\phi_1)$ becomes infinite and changes sign within region III. Some numerical results for various ν and γ are given in Appendix E.

Finally, note that according to Section 1.2, τ is defined by the artificial initial conditions and its value is different from the value of $\overline{\tau}_\mathrm{s}$. The ratio $\frac{\overline{\tau}_\mathrm{s}}{\tau}$ and the constant $\beta^\pm$, in Equation 2.9, cannot be evaluated using this expansion series method. The entire problem has to be computed using a different method and the constants are determined so that

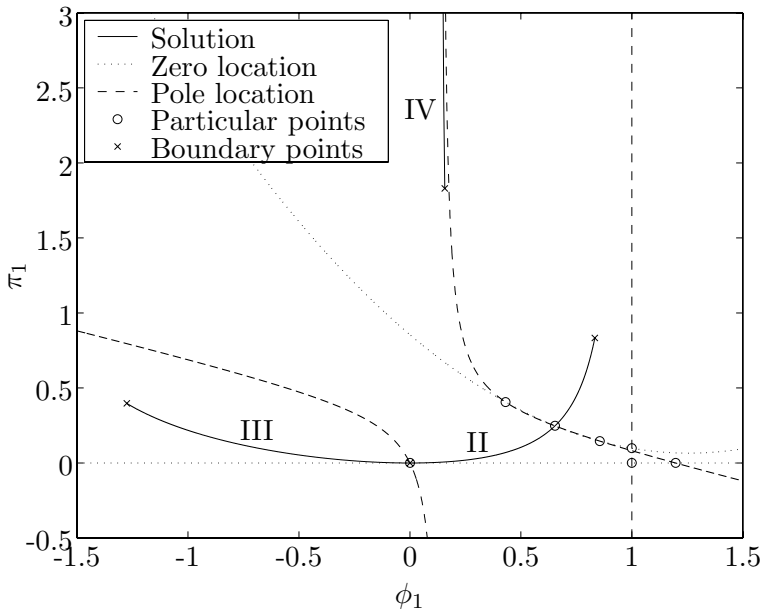

Figure 2.5: Zero and pole locations of the right-hand side of the $\pi_1'(\phi_1)$ equation (Equation 2.51), for $\nu = 2$, $\gamma = 1.4$, and $n = 0.83532$. The circles are the particular points that are intersections of the zero and the pole curves. The solution is represented by the solid curve and the crosses show the boundaries of the regions.

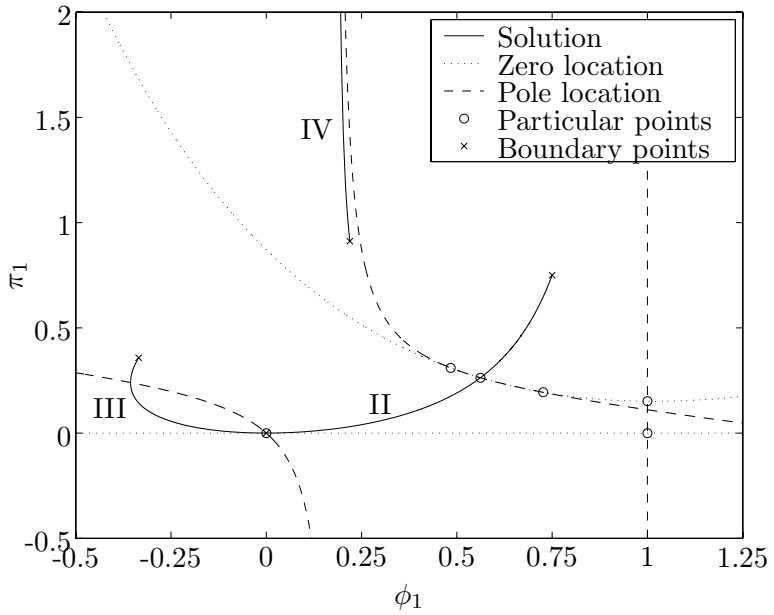

Figure 2.6: Zero and pole locations of the right-hand side of the $\pi_1'(\phi_1)$ equation (Equation 2.51), for $\nu = 3$, $\gamma = 5/3$, and $n = 0.68838$. The circles are the particular points that are intersections of the zero and the pole curves. The solution is represented by the solid curve and the crosses show the boundaries of the regions.

the shock trajectory fits the expansion. This process will be explained in more detail in Chapter 3.

2.3 Strong Shock Series Expansion

Guderley's solution described in Section 2.2 is only valid for very strong shocks ($M^2 \gg 1$ or $R_\mathrm{s} \ll c_\mathrm{I}\tau$). It is therefore useful to extend the solution in the form of an expansion so that the approximate solution remains valid over a wider range of Mach numbers. Although it has never been done, it was suggested by Guderley in 1942 [19]. The way to do this is to extend Equation 2.8 and to assume a shock position equation of the form

$$R_\mathrm{s}(t) = c_\mathrm{I}\overline{\tau}_\mathrm{s}\left(\frac{t}{\alpha^{\pm}\overline{\tau}_\mathrm{s}}\right)^n\left[1 + a_2^{\pm}\left(\frac{t}{\alpha^{\pm}\overline{\tau}_\mathrm{s}}\right)^{i_2} + a_3^{\pm}\left(\frac{t}{\alpha^{\pm}\overline{\tau}_\mathrm{s}}\right)^{i_3} + \mathrm{H.O.T.}\right], \tag{2.62}$$

where $i_k < i_{k+1}$ and where H.O.T. represents all the higher order terms. Each new term that is added introduces new equations to solve. Although it involves lengthy calculations, the method to find the values of i_k is straightforward. First, the shock location is expanded in terms of a power series in t. The shock jump conditions between I and II, and the variables ρ, P, and u are expanded as well. A new system of differential equations is written for each term. These systems of equations are singular at the exact same points as those found in the Guderley strong shock solution. To avoid these singularities, each system has to possess a coefficient $a_k^{\pm}$ that can be chosen appropriately. If the exponents i_k are not correct, some systems of equations will not have an available coefficient to avoid infinite derivatives at the singular point. Performing all the calculations, it can be shown that $i_k = 2\,(k-1)\,(1-n)$. The actual calculations that lead to these values are not presented, but the following paragraphs will show that these exponents are in fact correct since they introduce in each system of equations a coefficient $a_k^{\pm}$ that can be chosen to avoid singular behaviors.

In the next sections, Guderley's solution will be expanded. First, the equations will be written as series (Section 2.3.1), then two additional terms will be solved (Sections 2.3.2 and 2.3.3).

2.3.1 Expansion of the Equations

First, consider the shock motion equation introduced in Equation 2.62. Once the appropriate exponents are introduced, the shock motion is given by

$$R_{\mathrm{s}}(t) = c_{\mathrm{I}}\overline{\tau}_{\mathrm{s}}\left(\frac{t}{\alpha^{\pm}\overline{\tau}_{\mathrm{s}}}\right)^{n}\left[1 + a_2^{\pm}\left(\frac{t}{\alpha^{\pm}\overline{\tau}_{\mathrm{s}}}\right)^{2(1-n)} + a_3^{\pm}\left(\frac{t}{\alpha^{\pm}\overline{\tau}_{\mathrm{s}}}\right)^{4(1-n)} + \mathrm{H.O.T.}\right]. \quad (2.63)$$

This equation can be inverted to express t in terms of R_{s}, which gives

$$t(R_{\mathrm{s}}) = \alpha^{\pm}\overline{\tau}_{\mathrm{s}}\left(\frac{R_{\mathrm{s}}}{c_{\mathrm{I}}\overline{\tau}_{\mathrm{s}}}\right)^{\frac{1}{n}}\left[1 - \frac{a_2^{\pm}}{n}\left(\frac{R_{\mathrm{s}}}{c_{\mathrm{I}}\overline{\tau}_{\mathrm{s}}}\right)^{\frac{2(1-n)}{n}} + \frac{\left(a_2^{\pm}\right)^2(5-3n) - 2na_3^{\pm}}{2n^2}\left(\frac{R_{\mathrm{s}}}{c_{\mathrm{I}}\overline{\tau}_{\mathrm{s}}}\right)^{\frac{4(1-n)}{n}} + \mathrm{H.O.T.}\right]. \quad (2.64)$$

From the shock position equation, we can obtain its velocity,

$$U_{\mathrm{s}}(t) = c_{\mathrm{I}}\frac{n}{\alpha^{\pm}}\left(\frac{t}{\alpha^{\pm}\overline{\tau}_{\mathrm{s}}}\right)^{n-1}\left[1 + a_2^{\pm}\frac{2-n}{n}\left(\frac{t}{\alpha^{\pm}\overline{\tau}_{\mathrm{s}}}\right)^{2(1-n)} + a_3^{\pm}\frac{4-3n}{n}\left(\frac{t}{\alpha^{\pm}\overline{\tau}_{\mathrm{s}}}\right)^{4(1-n)} + \mathrm{H.O.T.}\right], \quad (2.65)$$

and finally, we can express that last equation in terms of the radius of the shock,

$$U_{\mathrm{s}}(R_{\mathrm{s}}) = c_{\mathrm{I}}\frac{n}{\alpha^{\pm}}\left(\frac{R_{\mathrm{s}}}{c_{\mathrm{I}}\overline{\tau}_{\mathrm{s}}}\right)^{\frac{n-1}{n}}\left[1 + \overline{a}_2^{\pm}\frac{1}{\gamma}\left(\frac{\alpha^{\pm}}{n}\right)^2\left(\frac{R_{\mathrm{s}}}{c_{\mathrm{I}}\overline{\tau}_{\mathrm{s}}}\right)^{\frac{2(1-n)}{n}} + \overline{a}_3^{\pm}\frac{1}{\gamma^2}\left(\frac{\alpha^{\pm}}{n}\right)^4\left(\frac{R_{\mathrm{s}}}{c_{\mathrm{I}}\overline{\tau}_{\mathrm{s}}}\right)^{\frac{4(1-n)}{n}} + \mathrm{H.O.T.}\right], \quad (2.66)$$

where we used the following normalized coefficients:

$$\overline{a}_2^{\pm} = \frac{a_2^{\pm}n\gamma(3-2n)}{\left(\alpha^{\pm}\right)^2} \quad (2.67)$$

$$\overline{a}_3^{\pm} = \frac{n^2\gamma^2\left[2a_3^{\pm}n(5-4n) - \left(a_2^{\pm}\right)^2(1-n)(7-4n)\right]}{2\left(\alpha^{\pm}\right)^4}. \quad (2.68)$$

Using this, series can also be written for each of the shock jump conditions as well as for

the continuity conditions between regions II and III. The results obtained are in the form of a series in terms of $\frac{r}{c_1\overline{\tau}_s}$ and lead us to try series of the form

$$\rho(\eta,r) = \rho_1\rho_1(\eta)\left[1+\rho_2(\eta)\left(\frac{r}{c_1\overline{\tau}_s}\right)^{\frac{2(1-n)}{n}} + \rho_3(\eta)\left(\frac{r}{c_1\overline{\tau}_s}\right)^{\frac{4(1-n)}{n}} + \text{H.O.T.}\right], \tag{2.69}$$

$$P(\eta,r) = P_1P_1(\eta)\left(\frac{n}{\alpha^{\pm}}\right)^2\left(\frac{r}{c_1\overline{\tau}_s}\right)^{\frac{2(n-1)}{n}} \left[1+P_2(\eta)\left(\frac{r}{c_1\overline{\tau}_s}\right)^{\frac{2(1-n)}{n}} + P_3(\eta)\left(\frac{r}{c_1\overline{\tau}_s}\right)^{\frac{4(1-n)}{n}} + \text{H.O.T.}\right], \tag{2.70}$$

$$u(\eta,r) = c_1u_1(\eta)\frac{n}{\alpha^{\pm}}\left(\frac{r}{c_1\overline{\tau}_s}\right)^{\frac{n-1}{n}} \left[1+u_2(\eta)\left(\frac{r}{c_1\overline{\tau}_s}\right)^{\frac{2(1-n)}{n}} + u_3(\eta)\left(\frac{r}{c_1\overline{\tau}_s}\right)^{\frac{4(1-n)}{n}} + \text{H.O.T.}\right]. \tag{2.71}$$

When all these series are introduced into Euler equations 2.4 to 2.6, the new expressions lead to a series of equations. The way to solve this new problem is to add one term at a time in the series. Assuming that the first k terms are solved, an additional term can be added in all the series (introducing a new coefficient $a^{\pm}_{k+1}$ in the process). Then, the system of equations defined by this additional term is solved and we can proceed to the next term. Previously, only the first term had been obtained (see Section 2.2). We will show how to get the second and third terms of this series in Sections 2.3.2 and 2.3.3, respectively. Note that a^{-}_{k+1} can be different than a^{+}_{k+1}.

2.3.2 Second Term

The equations for the second term are very long. For that reason, only the changes of variables that are performed to get the solution are described in this section. The final system of equations is, however, shown in Appendix B.

Changes of variables are appropriate to try to decouple the equations and to make them simpler to integrate. First, all the changes that were defined in Section 2.2 are introduced and the equations are written so that the functions and the derivatives are expressed in terms of ϕ_1. To remove the $\rho_1(\phi_1)$ and $\eta(\phi_1)$ dependence in the equations, the following

change of variables can be made:

$$\phi_2(\phi_1) = \frac{u_2(\phi_1)\, n^2\gamma}{(\alpha^{\pm})^2\, \eta(\phi_1)^{\frac{2(1-n)}{n}}}\phi_1, \tag{2.72}$$

$$\pi_2(\phi_1) = \frac{P_2(\phi_1)\, n^2\gamma}{(\alpha^{\pm})^2\, \eta(\phi_1)^{\frac{2(1-n)}{n}}}\,(1-\phi_1)\,, \tag{2.73}$$

$$\psi_2(\phi_1) = \frac{\rho_2(\phi_1)\, n^2\gamma}{(\alpha^{\pm})^2\, \eta(\phi_1)^{\frac{2(1-n)}{n}}}\,(1-\phi_1)\,. \tag{2.74}$$

The resulting system is made up of three coupled linear differential equations that can be written as

$$\frac{d\boldsymbol{x}}{d\phi_1} = \boldsymbol{A}(\phi_1)\,\boldsymbol{x} + \overline{a}_2^{\pm}\boldsymbol{b}(\phi_1)\,, \tag{2.75}$$

where

$$\boldsymbol{x} = \begin{pmatrix} \phi_2(\phi_1) \\ \pi_2(\phi_1) \\ \psi_2(\phi_1) \end{pmatrix}. \tag{2.76}$$

The matrix $\boldsymbol{A}(\phi_1)$ and the vector $\boldsymbol{b}(\phi_1)$ are known functions that are singular in region II at $\phi_1 = \phi_1^*$ (first order pole). Since all of the three differential equations are singular, we can use the following new change of variables to obtain two non-singular equations and one singular equation:

$$\omega_2(\phi_1) = [2\,(1-n) + n\nu]\,\psi_2(\phi_1)\,, \tag{2.77}$$

$$\xi_2(\phi_1) = \psi_2(\phi_1) - \phi_2(\phi_1)\,, \tag{2.78}$$

$$\sigma_2(\phi_1) = \frac{2\,(1-n) + n\nu}{2\,(1-n)}\,[\pi_2(\phi_1) - \gamma\psi_2(\phi_1)] + [\psi_2(\phi_1) - \phi_2(\phi_1)]\,. \tag{2.79}$$

This last change of variables leads to a system of equations that is relatively easy to solve (see Appendix B). The first of the three differential equations is independent of $\omega_2(\phi_1)$ and of $\xi_2(\phi_1)$. Since it is not singular at $\phi_1 = \phi_1^*$, this equation does not introduce any condition on the value of $\overline{a}_2^{-}$. Furthermore, it is possible to integrate it analytically, which gives

$$\sigma_2(\phi_1) = C\frac{\rho_1(\phi_1)^{\gamma-1}\,\eta(\phi_1)^2}{\pi_1(\phi_1)} - \phi_1\overline{a}_2^{\pm}, \tag{2.80}$$

where C is an integration constant that is different in each region and that can be found very easily using the region boundary conditions. The last two equations are coupled but only one is singular in region II.

Note that, as can be seen in Appendix B, the differential equations and the boundary conditions are linear in $\overline{a}_2^{\pm}$. This means that the functions can be expressed as $f_2(\phi_1) = f_{2,\mathrm{a}}(\phi_1) + f_{2,\mathrm{b}}(\phi_1)\,\overline{a}_2^{\pm}$, and the system can be split into a part independent of $\overline{a}_2^{\pm}$ and another proportional to $\overline{a}_2^{\pm}$.

To solve this second-term problem, we first start with region II. Knowing the shock jump conditions for $\sigma_2(\phi_1)$, it is easy to find the constant C_{II} in Equation 2.80. Note that at this point C_{II} is of the form $C_{\mathrm{II,a}} + C_{\mathrm{II,b}}\overline{a_2^-}$, with $C_{\mathrm{II,a}}$ and $C_{\mathrm{II,b}}$ being known constants. We can then focus on the two other equations. We start by choosing ω_2^* and ξ_2^* at the singularity. Then, we find the value of $\overline{a_2^-}$ that avoids a singular behavior, as well as the limit of the equations at the singularity, using L'Hôpital's theorem. Starting from the singularity, we can then integrate towards the shock. Iterating on the values of ω_2^* and ξ_2^*, a shooting method is used to satisfy the shock jump conditions.

Note that the limiting values of the derivatives at the singularity involve limiting values of the second derivatives of first term variables. It can also be shown that the limiting values of the derivatives of the ith term involve limiting values of the ith derivatives of the first term. This also means that since, in our case, the first term is integrated with fourth-order accuracy, the second term is accurate to third order and the third is only accurate to second order.

Once region II is completely obtained, regions III and IV are solved together. The value of $\overline{a}_2^+$ is such that the velocity remains 0 in region IV for $r = 0$. Looking at the form of the variable expansions as well as the changes of variables, a sufficient condition for that is that the functions $\sigma_{2,\mathrm{IV}}$, $\omega_{2,\mathrm{IV}}$, and $\xi_{2,\mathrm{IV}}$ remain finite everywhere. This leads to a condition linking $\omega_{2,\mathrm{IV}}$ and $\xi_{2,\mathrm{IV}}$ at $r = 0$ as seen in Appendix C. To solve the equations, we choose the values of $\sigma_{2,\mathrm{IV}}$ at the shock and of $\xi_{2,\mathrm{IV}}$ at $r = 0$. The equations are then integrated towards the shock, the inverse shock jump conditions are used to obtain boundary values in region III and finally, the variables are integrated up to $\eta = 0$. A shooting method is

once again performed and we iterate to find $\omega_{2,\mathrm{IV}}$ and $\xi_{2,\mathrm{IV}}$ at $r = 0$, as well as $\overline{a}_2^+$, so that $\rho_{2,\mathrm{II}}$, $P_{2,\mathrm{II}}$, and $u_{2,\mathrm{II}}$ are continuous at $\eta = 0$.

Note that once again, equations have to be adapted to take care of the limiting behaviors of the variables, as explained in Appendix C.

2.3.3 Third Term

The third term is obtained in the same manner as the second term. The equations in this case are much longer and fill pages. The changes of variables as well as the procedure to obtain the solution are described, but the details are not given. Again, all previous changes of variables are performed and the functions are expressed in terms of ϕ_1. Then, a first change of variables is made to avoid dependence on $\eta(\phi_1)$ and $\rho_1(\phi_1)$:

$$\phi_3(\phi_1) = \frac{u_3(\phi_1)\, n^4\gamma^2}{(\alpha^{\pm})^4\, \eta(\phi_1)^{\frac{4(1-n)}{n}}}\phi_1, \tag{2.81}$$

$$\pi_3(\phi_1) = \frac{P_3(\phi_1)\, n^4\gamma^2}{(\alpha^{\pm})^4\, \eta(\phi_1)^{\frac{4(1-n)}{n}}}\,(1-\phi_1)\,, \tag{2.82}$$

$$\psi_3(\phi_1) = \frac{\rho_3(\phi_1)\, n^4\gamma^2}{(\alpha^{\pm})^4\, \eta(\phi_1)^{\frac{4(1-n)}{n}}}\,(1-\phi_1)\,. \tag{2.83}$$

This leads to a system of the form

$$\frac{d\boldsymbol{x}}{d\phi_1} = \boldsymbol{A}(\phi_1)\,\boldsymbol{x} + \overline{a}_3^{\pm}\boldsymbol{b}(\phi_1) + \boldsymbol{c}(\phi_1)\,, \tag{2.84}$$

where

$$\boldsymbol{x} = \begin{pmatrix} \phi_2(\phi_1) \\ \pi_2(\phi_1) \\ \psi_2(\phi_1) \end{pmatrix}. \tag{2.85}$$

This system is composed of three equations that are singular in region II at $\phi_{1,\mathrm{II}} = \phi_1^*$. To decouple one of these equations and to have only one of them singular, the following change

of variables can be used:

$$\omega_3(\phi_1) = [4\,(1-n) + n\nu]\,\psi_3(\phi_1)\,, \tag{2.86}$$

$$\xi_3(\phi_1) = \psi_3(\phi_1) - \phi_3(\phi_1)\,, \tag{2.87}$$

$$\sigma_3(\phi_1) = \frac{4\,(1-n)+n\nu}{2\,(1-n)}\,[\pi_3(\phi_1) - \gamma\psi_3(\phi_1)] + [\psi_3(\phi_1) - \phi_3(\phi_1)]\,. \tag{2.88}$$

The resulting system includes one non-coupled first-order differential equation for $\sigma_3(\phi_1)$. Although this equation seems too complicated to integrate analytically, a numerical integration can be performed directly. The two other equations are coupled but only one of them is singular at $\phi_{1,\mathrm{II}} = \phi_1^*$. The way to solve the problem is exactly the same as for the second term.

2.4 Weak Shock Series Expansion

Guderley's problem does not have any length scale. The shock is supposed to come from infinity, to travel up to $r = 0$, and then to bounce back to infinity. It is therefore also interesting to look for an expansion solution when the shock is still weak and far away from the origin. This can only be done in the incoming shock case ($t \ll -\tau$). In fact, in the reflected shock case, the full history of the flow is required and no analytic limiting behavior can be obtained easily. In this section, we will construct an expansion in a similar way to what was done in Sections 2.2 and 2.3, but instead of expanding the solution around $(r,\, t)$ close to $(0,\, 0)$, we will do it around $(r,\, t)$ tending to $(\infty,\, -\infty)$.

To solve this problem, we write the expansion in the following form:

$$R_\mathrm{s}(t) = c_\mathrm{I}\tau\left[\frac{-t}{\tau} + \sum_{k=1}^{\infty} a_k \left(\frac{-t}{\tau}\right)^{1-ki}\right], \tag{2.89}$$

where the coefficients a_k have to be found and where i is such that each system of equations in the series introduces a new coefficient a_k, which is in turn chosen such that the corresponding system becomes non-singular. This expression is such that, for large t, the shock velocity becomes c_I, which corresponds to the propagation speed of an infinitely weak wave.

Note that additional terms,

$$\sum_{k=0}^{\infty} b_k \frac{\log\left(\frac{-t}{\tau}\right)}{\left(\frac{-t}{\tau}\right)^{ki}},$$

have to be added if $\frac{1}{i}$ is a positive integer. This is because, in that case, one of the terms in Equation 2.89 becomes just a constant and vanishes as soon as we calculate $U_{\mathrm{s}}(t) = \frac{dR_{\mathrm{s}}(t)}{dt}$. To avoid any singularity in the solution, a complete series expansion of $U_{\mathrm{s}}(t)$ is required and these additional terms are needed.

The calculations involved in the determination of i are not complicated and although these are simpler than in the strong shock case, they are too long to present here. In the cylindrical case, we can find that $i = \frac{1}{2}$ and in the spherical case, we get $i = 1$. The first terms of these two cases will be examined in Sections 2.4.1 and 2.4.2. Note finally that τ is the characteristic time, which has the same value as the one defined in Equation 1.18.

2.4.1 Cylindrical Case

In this case, the shock position expansion can be formed using $i = \frac{1}{2}$ and we get the following shock motion expansion:

$$R_{\mathrm{s}}(t) = c_1 \tau \left[\frac{-t}{\tau} + a_1 \sqrt{\frac{-t}{\tau}} + b_0 \log\left(\frac{-t}{\tau}\right) + a_2 + \mathrm{H.O.T.} \right]. \tag{2.90}$$

If we pose that $\overline{\tau}_{\mathrm{w}} = a_1^2 \tau$, we can rewrite this expansion as

$$R_{\mathrm{s}}(t) = c_1 \overline{\tau}_{\mathrm{w}} \left[\frac{-t}{\overline{\tau}_{\mathrm{w}}} + \sqrt{\frac{-t}{\overline{\tau}_{\mathrm{w}}}} + \overline{b}_0 \log\left(\frac{-t}{\overline{\tau}_{\mathrm{w}}}\right) + \overline{a}_2 + \mathrm{H.O.T.} \right], \tag{2.91}$$

where

$$\overline{b}_0 = \frac{b_0}{a_1^2}, \tag{2.92}$$

$$\overline{a}_2 = \frac{a_2 + b_0 \log\left(a_1^2\right)}{a_1^2}. \tag{2.93}$$

This expression can be inverted to give

$$t(R_{\rm s}) = -\tau\left[\frac{R_{\rm s}}{c_{\rm I}\overline{\tau}_{\rm w}} - \sqrt{\frac{R_{\rm s}}{c_{\rm I}\overline{\tau}_{\rm w}}} - \overline{b}_0\log\left(\frac{R_{\rm s}}{c_{\rm I}\overline{\tau}_{\rm w}}\right) + \left(\frac{1}{2} - \overline{a}_2\right) + \text{H.O.T.}\right]. \tag{2.94}$$

From the shock position we can get the shock velocity

$$U_{\rm s}(t) = \frac{dR_{\rm s}(t)}{dt} = -c_{\rm I}\left[1 + \frac{1}{2}\sqrt{\frac{\overline{\tau}_{\rm w}}{-t}} + \overline{b}_0\frac{\overline{\tau}_{\rm w}}{-t} + \text{H.O.T.}\right], \tag{2.95}$$

which can also be expressed as a function of $R_{\rm s}$,

$$U_{\rm s}(R_{\rm s}) = -c_{\rm I}\left[1 + \frac{1}{2}\sqrt{\frac{c_{\rm I}\overline{\tau}_{\rm w}}{R_{\rm s}}} + \left(\frac{1}{4} + \overline{b}_0\right)\frac{c_{\rm I}\overline{\tau}_{\rm w}}{R_{\rm s}} + \text{H.O.T.}\right]. \tag{2.96}$$

Replacing $U_{\rm s}(R_{\rm s})$ in equations 1.30 to 1.32, we can obtain an expansion of the shock jump conditions:

$$\rho_{\rm II}(1) = \rho_{\rm I}\left[1 + \frac{2}{\gamma+1}\sqrt{\frac{c_{\rm I}\overline{\tau}_{\rm w}}{R_{\rm s}}} + \frac{7-\gamma+8\overline{b}_0\,(1+\gamma)}{2(1+\gamma)^2}\frac{c_{\rm I}\overline{\tau}_{\rm w}}{R_{\rm s}} + \text{H.O.T.}\right], \tag{2.97}$$

$$P_{\rm II}(1) = P_{\rm I}\left[1 + \frac{2\gamma}{\gamma+1}\sqrt{\frac{c_{\rm I}\overline{\tau}_{\rm w}}{R_{\rm s}}} + \frac{\left(3+8\overline{b}_0\right)\gamma}{2\,(1+\gamma)}\frac{c_{\rm I}\overline{\tau}_{\rm w}}{R_{\rm s}} + \text{H.O.T.}\right], \tag{2.98}$$

$$u_{\rm II}(1) = c_{\rm I}\left[-\frac{2}{\gamma+1}\sqrt{\frac{c_{\rm I}\overline{\tau}_{\rm w}}{R_{\rm s}}} - \frac{1+8\overline{b}_0}{2\,(1+\gamma)}\frac{c_{\rm I}\overline{\tau}_{\rm w}}{R_{\rm s}} + \text{H.O.T.}\right]. \tag{2.99}$$

Since these conditions are applied at $\eta = 1$, we can replace $R_{\rm s}$ by r in the previous equations, which leads us to try the following variable forms:

$$\rho_{\rm II}(\eta, r) = \rho_{\rm I}\left[1 + \rho_{1,\rm II}(\eta)\sqrt{\frac{c_{\rm I}\overline{\tau}_{\rm w}}{r}} + \rho_{2,\rm II}(\eta)\frac{c_{\rm I}\overline{\tau}_{\rm w}}{r} + \text{H.O.T.}\right], \tag{2.100}$$

$$P_{\rm II}(\eta, r) = P_{\rm I}\left[1 + P_{1,\rm II}(\eta)\sqrt{\frac{c_{\rm I}\overline{\tau}_{\rm w}}{r}} + P_{2,\rm II}(\eta)\frac{c_{\rm I}\overline{\tau}_{\rm w}}{r} + \text{H.O.T.}\right], \tag{2.101}$$

$$u_{\rm II}(\eta, r) = c_{\rm I}\left[u_{1,\rm II}(\eta)\sqrt{\frac{c_{\rm I}\overline{\tau}_{\rm w}}{r}} + u_{2,\rm II}(\eta)\frac{c_{\rm I}\overline{\tau}_{\rm w}}{r} + \text{H.O.T.}\right]. \tag{2.102}$$

Replacing these variables in Equations 2.4 to 2.6, we can get a series of systems of equations.

The first two are

$$u_{1,\mathrm{II}}(\eta) - 2\left[\eta u'_{1,\mathrm{II}}(\eta) + \rho'_{1,\mathrm{II}}(\eta)\right] = 0, \tag{2.103}$$

$$P_{1,\mathrm{II}}(\eta) + 2\left[\eta P'_{1,\mathrm{II}}(\eta) + \gamma u'_{1,\mathrm{II}}(\eta)\right] = 0, \tag{2.104}$$

$$P'_{1,\mathrm{II}}(\eta) - \gamma \rho'_{1,\mathrm{II}}(\eta) = 0, \tag{2.105}$$

and

$$\frac{\rho'_{1,\mathrm{II}}(\eta)}{2\sqrt{\eta}} + \rho'_{2,\mathrm{II}}(\eta) + \eta\left[u'_{2,\mathrm{II}}(\eta) + \rho_{1,\mathrm{II}}(\eta)\, u'_{1,\mathrm{II}}(\eta) + u_{1,\mathrm{II}}(\eta)\, \rho'_{1,\mathrm{II}}(\eta)\right] = 0, \tag{2.106}$$

$$P_{2,\mathrm{II}}(\eta) + \eta P'_{2,\mathrm{II}}(\eta) + \gamma\left[u'_{2,\mathrm{II}}(\eta) + \rho_{1,\mathrm{II}}(\eta)\, u'_{1,\mathrm{II}}(\eta) + \eta u_{1,\mathrm{II}}(\eta)\, u'_{1,\mathrm{II}}(\eta)\right] + \frac{\gamma}{2}\left[\frac{1}{\sqrt{\eta}} u'_{1,\mathrm{II}}(\eta) + u_{1,\mathrm{II}}(\eta)^2\right] = 0, \tag{2.107}$$

$$P'_{2,\mathrm{II}}(\eta) - \gamma\left[(\gamma - 1)\, \rho_{1,\mathrm{II}}(\eta)\, \rho'_{1,\mathrm{II}}(\eta) + \rho'_{2,\mathrm{II}}(\eta)\right] = 0. \tag{2.108}$$

Consider the first system of equations, along with the appropriate shock jump conditions. The solution to this problem is the following:

$$\rho_{1,\mathrm{II}}(\eta) = \frac{4}{\pi(\gamma+1)} K\left(\frac{1-\eta}{2}\right), \tag{2.109}$$

$$P_{1,\mathrm{II}}(\eta) = \frac{-4}{\pi(\gamma+1)}\left[2E\left(\frac{1-\eta}{2}\right) - K\left(\frac{1-\eta}{2}\right)\right], \tag{2.110}$$

$$u_{1,\mathrm{II}}(\eta) = \frac{4\gamma}{\pi(\gamma+1)} K\left(\frac{1-\eta}{2}\right), \tag{2.111}$$

where the functions K and E are the complete elliptic integrals of the first and the second kind, respectively. These are defined as

$$K(x) = \int_0^{\frac{\pi}{2}} \sqrt{1 - x\sin(\theta)^2}\, d\theta, \tag{2.112}$$

$$E(x) = \int_0^{\frac{\pi}{2}} \frac{1}{\sqrt{1 - x\sin(\theta)^2}}\, d\theta. \tag{2.113}$$

The system of equations for the second term is much more complicated and has the following

first integral:

$$P_{2,\mathrm{II}}(\eta) - \gamma\left[\frac{\gamma-1}{2}\rho_{1,\mathrm{II}}(\eta)^2 + \rho_{2,\mathrm{II}}(\eta)\right] = 0. \tag{2.114}$$

The analytical solution will not be searched for, since the expressions are complicated, but it is relatively easy to find the value of b_0 by expanding these equations. First, we can write a differential equation for $P_{2,\mathrm{II}}(\eta)$:

$$P'_{2,\mathrm{II}}(\eta) = \frac{\frac{\gamma}{4\sqrt{\eta}}u_{1,\mathrm{II}}(\eta) + \eta\left[P_{2,\mathrm{II}}(\eta) + \gamma\eta\left(u^2_{1,\mathrm{II}}(\eta)\right)'\right] - \gamma\left[\frac{\rho'_{1,\mathrm{II}}(\eta)}{\sqrt{\eta}} - \frac{\gamma-1}{2}\left(\rho^2_{1,\mathrm{II}}(\eta)\right)'\right]}{1-\eta^2}. \tag{2.115}$$

Replacing the first term functions by their solutions and taking the dominant term of the right-hand side of the resulting equation for η close to 1 leads to

$$P'_{2,\mathrm{II}}(\eta) = \frac{1}{1-\eta}\left[\frac{\gamma\left(13-3\gamma\right)}{8\left(\gamma+1\right)^2} + \frac{P_{2,\mathrm{II}}(1)}{2}\right] + \mathcal{O}(1)\,. \tag{2.116}$$

Since the variables need to be bounded everywhere, this leading term has to be suppressed. Replacing $P_{2,\mathrm{II}}(1)$ by its value in the shock jump conditions, we have a condition for $\overline{b}_0$:

$$\overline{b}_0 = -\frac{19+3\gamma}{16\left(\gamma+1\right)}. \tag{2.117}$$

The resulting shock motion is given by

$$R_{\mathrm{s}}(t) = c_{\mathrm{I}}\overline{\tau}_{\mathrm{w}}\left[\frac{-t}{\overline{\tau}_{\mathrm{w}}} + \sqrt{\frac{-t}{\overline{\tau}_{\mathrm{w}}}} - \frac{19+3\gamma}{16\left(\gamma+1\right)}\log\left(\frac{-t}{\overline{\tau}_{\mathrm{w}}}\right) + \overline{a}_2 + \mathrm{H.O.T.}\right]. \tag{2.118}$$

It is impossible to fix the value of $\overline{a}_2$ using expansion equations. In theory, $\overline{a}_2$ is fixed so that when the shock reaches $r = 0$, we also have $t = 0$. In addition, $\frac{\overline{\tau}_{\mathrm{w}}}{\tau}$ has a specific value so that the shock trajectory fits the expansions. If we want these two values, the whole problem has to be solved using another numerical method. That will be done in Chapter 3.

2.4.2 Spherical Case

In the spherical case, $i = 1$ and Equation 2.89 gives the following shock motion:

$$R_{\rm s}(t) = c_{\rm I}\tau \left[\frac{-t}{\tau} + b_0 \log\!\left(\frac{-t}{\tau}\right) + a_1 + b_1 \frac{\log\left(\frac{-t}{\tau}\right)}{\frac{-t}{\tau}} + a_2 \frac{1}{\frac{-t}{\tau}} + \text{H.O.T.} \right]. \tag{2.119}$$

This expression can be simplified if we set $\overline{\tau}_{\rm w} = b_0\tau$:

$$R_{\rm s}(t) = c_{\rm I}\overline{\tau}_{\rm w} \left[\frac{-t}{\overline{\tau}_{\rm w}} + \log\!\left(\frac{-t}{\overline{\tau}_{\rm w}}\right) + \overline{a}_1 + \overline{b}_1 \frac{\log\left(\frac{-t}{\overline{\tau}_{\rm w}}\right)}{\frac{-t}{\overline{\tau}_{\rm w}}} + \overline{a}_2 \frac{1}{\frac{-t}{\overline{\tau}_{\rm w}}} + \text{H.O.T.} \right], \tag{2.120}$$

where

$$\overline{a}_1 = \frac{a_1}{b_0} + \log(b_0)\,, \tag{2.121}$$

$$\overline{a}_2 = \frac{a_2 + b_1 \log(b_0)}{b_0^2}, \tag{2.122}$$

$$\overline{b}_1 = \frac{b_1}{b_0^2}. \tag{2.123}$$

This expansion can be inverted to

$$t(R_{\rm s}) = -\overline{\tau}_{\rm w} \left[\frac{R_{\rm s}}{c_{\rm I}\overline{\tau}_{\rm w}} - \log\!\left(\frac{R_{\rm s}}{c_{\rm I}\overline{\tau}_{\rm w}}\right) - \overline{a}_1 + \left(1 - \overline{b}_1\right) \frac{\log\left(\frac{R_{\rm s}}{c_{\rm I}\overline{\tau}_{\rm w}}\right)}{\frac{R_{\rm s}}{c_{\rm I}\overline{\tau}_{\rm w}}} + \left(\overline{a}_1 - \overline{a}_2\right) \frac{1}{\frac{R_{\rm s}}{c_{\rm I}\overline{\tau}_{\rm w}}} + \text{H.O.T.} \right]. \tag{2.124}$$

The velocity of the shock can be calculated and expressed as a function of the shock radius:

$$U_{\rm s}(R_{\rm s}) = -c_{\rm I} \left[1 + \frac{1}{\frac{R_{\rm s}}{c_{\rm I}\overline{\tau}_{\rm w}}} + \left(1 - \overline{b}_1\right) \frac{\log\left(\frac{R_{\rm s}}{c_{\rm I}\overline{\tau}_{\rm w}}\right)}{\frac{R_{\rm s}}{c_{\rm I}\overline{\tau}_{\rm w}}} + \left(\overline{a}_1 - \overline{a}_2 + \overline{b}_1\right) \frac{1}{\left(\frac{R_{\rm s}}{c_{\rm I}\overline{\tau}_{\rm w}}\right)^2} + \text{H.O.T.} \right]. \tag{2.125}$$

Once again, using this result, the shock jump conditions at $\eta = 1$ can be expanded to give

$$\rho_{\mathrm{II}}(1) = \rho_{\mathrm{I}} \left[1 + \frac{4}{\gamma+1} \frac{1}{\frac{R_{\mathrm{s}}}{c_{\mathrm{I}}\overline{\tau}_{\mathrm{w}}}} + \frac{4\left(1-\overline{b}_1\right)}{\gamma+1} \frac{\log\left(\frac{R_{\mathrm{s}}}{c_{\mathrm{I}}\overline{\tau}_{\mathrm{w}}}\right)}{\left(\frac{R_{\mathrm{s}}}{c_{\mathrm{I}}\overline{\tau}_{\mathrm{w}}}\right)^2} + \frac{4\left(\frac{5-3\gamma}{2(\gamma+1)} + \overline{a}_1 - \overline{a}_2 + \overline{b}_1\right)}{(\gamma+1)\left(\frac{R_{\mathrm{s}}}{c_{\mathrm{I}}\overline{\tau}_{\mathrm{w}}}\right)^2} + \mathrm{H.O.T.} \right], \quad (2.126)$$

$$P_{\mathrm{II}}(1) = P_{\mathrm{I}} \left[1 + \frac{4\gamma}{\gamma+1} \frac{1}{\frac{R_{\mathrm{s}}}{c_{\mathrm{I}}\overline{\tau}_{\mathrm{w}}}} + \frac{4\gamma\left(1-\overline{b}_1\right)}{\gamma+1} \frac{\log\left(\frac{R_{\mathrm{s}}}{c_{\mathrm{I}}\overline{\tau}_{\mathrm{w}}}\right)}{\left(\frac{R_{\mathrm{s}}}{c_{\mathrm{I}}\overline{\tau}_{\mathrm{w}}}\right)^2} + \frac{4\gamma\left(\frac{1}{2} + \overline{a}_1 - \overline{a}_2 + \overline{b}_1\right)}{(\gamma+1)\left(\frac{R_{\mathrm{s}}}{c_{\mathrm{I}}\overline{\tau}_{\mathrm{w}}}\right)^2} + \mathrm{H.O.T.} \right], \quad (2.127)$$

$$u_{\mathrm{II}}(1) = c_{\mathrm{I}} \left[-\frac{4}{\gamma+1} \frac{1}{\frac{R_{\mathrm{s}}}{c_{\mathrm{I}}\overline{\tau}_{\mathrm{w}}}} - \frac{4\left(1-\overline{b}_1\right)}{\gamma+1} \frac{\log\left(\frac{R_{\mathrm{s}}}{c_{\mathrm{I}}\overline{\tau}_{\mathrm{w}}}\right)}{\left(\frac{R_{\mathrm{s}}}{c_{\mathrm{I}}\overline{\tau}_{\mathrm{w}}}\right)^2} + \frac{4\left(\frac{1}{2} - \overline{a}_1 + \overline{a}_2 - \overline{b}_1\right)}{(\gamma+1)\left(\frac{R_{\mathrm{s}}}{c_{\mathrm{I}}\overline{\tau}_{\mathrm{w}}}\right)^2} + \mathrm{H.O.T.} \right]. \quad (2.128)$$

This leads to variables of the following form:

$$\rho_{\mathrm{II}}(\eta, r) = \rho_{\mathrm{I}} \left[1 + \rho_{1,\mathrm{II}}(\eta) \frac{1}{\frac{r}{c_{\mathrm{I}}\overline{\tau}_{\mathrm{w}}}} + \rho_{2,\mathrm{II}}(\eta) \frac{\log\left(\frac{r}{c_{\mathrm{I}}\overline{\tau}_{\mathrm{w}}}\right)}{\left(\frac{r}{c_{\mathrm{I}}\overline{\tau}_{\mathrm{w}}}\right)^2} + \rho_{3,\mathrm{II}}(\eta) \frac{1}{\left(\frac{r}{c_{\mathrm{I}}\overline{\tau}_{\mathrm{w}}}\right)^2} + \mathrm{H.O.T.} \right], \quad (2.129)$$

$$P_{\mathrm{II}}(\eta, r) = P_{\mathrm{I}} \left[1 + P_{1,\mathrm{II}}(\eta) \frac{1}{\frac{r}{c_{\mathrm{I}}\overline{\tau}_{\mathrm{w}}}} + P_{2,\mathrm{II}}(\eta) \frac{\log\left(\frac{r}{c_{\mathrm{I}}\overline{\tau}_{\mathrm{w}}}\right)}{\left(\frac{r}{c_{\mathrm{I}}\overline{\tau}_{\mathrm{w}}}\right)^2} + P_{3,\mathrm{II}}(\eta) \frac{1}{\left(\frac{r}{c_{\mathrm{I}}\overline{\tau}_{\mathrm{w}}}\right)^2} + \mathrm{H.O.T.} \right], \quad (2.130)$$

$$u_{\mathrm{II}}(\eta, r) = c_{\mathrm{I}} \left[u_{1,\mathrm{II}}(\eta) \frac{1}{\frac{r}{c_{\mathrm{I}}\overline{\tau}_{\mathrm{w}}}} + u_{2,\mathrm{II}}(\eta) \frac{\log\left(\frac{r}{c_{\mathrm{I}}\overline{\tau}_{\mathrm{w}}}\right)}{\left(\frac{r}{c_{\mathrm{I}}\overline{\tau}_{\mathrm{w}}}\right)^2} + u_{3,\mathrm{II}}(\eta) \frac{1}{\left(\frac{r}{c_{\mathrm{I}}\overline{\tau}_{\mathrm{w}}}\right)^2} + \mathrm{H.O.T.} \right]. \quad (2.131)$$

Substituting these expressions into Equations 2.4 to 2.6, it is relatively easy to extract the systems of equations relative to the first three terms. First, extracting the equations relative

to the first term (the term in $\frac{1}{r}$), we get

$$u_{1,\mathrm{II}}(\eta) - \eta u'_{1,\mathrm{II}}(\eta) - \rho'_{1,\mathrm{II}}(\eta) = 0, \tag{2.132}$$

$$P_{1,\mathrm{II}}(\eta) + \eta P'_{1,\mathrm{II}}(\eta) + \gamma u'_{1,\mathrm{II}}(\eta) = 0, \tag{2.133}$$

$$P'_{1,\mathrm{II}}(\eta) - \gamma \rho'_{1,\mathrm{II}}(\eta) = 0. \tag{2.134}$$

Given the boundary conditions, it is easy to find the solution of this system:

$$\rho_{1,\mathrm{II}}(\eta) = \frac{4}{\gamma+1}, \tag{2.135}$$

$$P_{1,\mathrm{II}}(\eta) = \frac{4\gamma}{\gamma+1}, \tag{2.136}$$

$$u_{1,\mathrm{II}}(\eta) = \frac{-4\eta}{\gamma+1}. \tag{2.137}$$

The second system corresponds to the terms in $\frac{\log(r)}{r^2}$:

$$\eta u'_{2,\mathrm{II}}(\eta) + \rho'_{2,\mathrm{II}}(\eta) = 0, \tag{2.138}$$

$$2P_{2,\mathrm{II}}(\eta) + \eta P'_{2,\mathrm{II}}(\eta) + \gamma u'_{2,\mathrm{II}}(\eta) = 0, \tag{2.139}$$

$$P'_{2,\mathrm{II}}(\eta) - \gamma \rho'_{2,\mathrm{II}}(\eta) = 0. \tag{2.140}$$

Solving this system for $P_{2,\mathrm{II}}(\eta)$, we find that

$$P_{2,\mathrm{II}}(\eta) = \frac{C}{1-\eta^2}, \tag{2.141}$$

which is singular at $\eta = 1$ and cannot satisfy the boundary conditions unless $C = 0$. The only way that is possible is to impose the condition that $\overline{b}_1 = 1$. The solution then becomes

$$\rho_{2,\mathrm{II}}(\eta) = 0, \tag{2.142}$$

$$P_{2,\mathrm{II}}(\eta) = 0, \tag{2.143}$$

$$u_{2,\mathrm{II}}(\eta) = 0. \tag{2.144}$$

Finally, the system corresponding to $\frac{1}{r^2}$, can be written as

$$\rho'_{3,\mathrm{II}}(\eta) + \eta u'_{3,\mathrm{II}}(\eta) - \frac{16\eta}{(\gamma+1)^2} = 0, \tag{2.145}$$

$$2P_{3,\mathrm{II}}(\eta) + \eta P'_{3,\mathrm{II}}(\eta) + \gamma u'_{3,\mathrm{II}}(\eta) - \frac{4\gamma\left(1+\gamma+4\eta-8\eta^3\right)}{\eta(\gamma+1)^2} = 0, \tag{2.146}$$

$$P'_{3,\mathrm{II}}(\eta) - \gamma\rho'_{3,\mathrm{II}}(\eta) = 0. \tag{2.147}$$

This system can be solved for $P_{3,\mathrm{II}}(\eta)$, which gives

$$P_{3,\mathrm{II}}(\eta) = \frac{4\gamma\eta\left(2\eta^3-\gamma-1\right)+C}{(1+\gamma)^2(1-\eta^2)}. \tag{2.148}$$

Once again, this solution is singular at $\eta = 1$ unless $C = 4\gamma(\gamma-1)$. To satisfy the shock jump conditions under that condition, we need to have $\overline{a}_2 = \overline{a}_1 + \frac{\gamma+5}{\gamma+1}$. The solution then becomes

$$\rho_{3,\mathrm{II}}(\eta) = \frac{4}{\gamma+1}\left[\frac{1}{1+\eta} - \frac{2\left(\gamma+\eta^2\right)}{\gamma+1}\right], \tag{2.149}$$

$$P_{3,\mathrm{II}}(\eta) = \frac{4\gamma}{\gamma+1}\left[\frac{1}{1+\eta} - \frac{2\left(1+\eta^2\right)}{\gamma+1}\right], \tag{2.150}$$

$$u_{3,\mathrm{II}}(\eta) = \frac{4}{\gamma+1}\left[\frac{1}{1+\eta} - \frac{4(1-2\eta)}{\gamma+1} + \log\left(\frac{2\eta}{1+\eta}\right)\right]. \tag{2.151}$$

All these last calculations lead to a shock motion of the following form:

$$R_{\mathrm{s}}(t) = c_{\mathrm{I}}\overline{\tau}_{\mathrm{w}}\left[\frac{-t}{\overline{\tau}_{\mathrm{w}}} + \log\left(\frac{-t}{\overline{\tau}_{\mathrm{w}}}\right) + \overline{a}_1 + \frac{\log\left(\frac{-t}{\overline{\tau}_{\mathrm{w}}}\right)}{\frac{-t}{\overline{\tau}_{\mathrm{w}}}} + \frac{\overline{a}_1 + \frac{\gamma+5}{\gamma+1}}{\frac{-t}{\overline{\tau}_{\mathrm{w}}}} + \mathrm{H.O.T.}\right]. \tag{2.152}$$

The values of $\overline{a}_1$ and of $\frac{\overline{\tau}_{\mathrm{w}}}{\tau}$ cannot be determined using expansion equations, and their values can only be found by integrating the complete equations until the shock reaches the origin. Like in the cylindrical case, $\overline{a}_1$ is such that $R_{\mathrm{s}}(0) = 0$, and $\frac{\overline{\tau}_{\mathrm{w}}}{\tau}$ is such that the shock trajectory matches the expansion.

2.5 Summary

In this section, we will summarize the results that have been found in this chapter. The problem was redefined in terms of r and $\eta = \frac{R_s(t)}{r}$. The limiting behaviors were examined and the following shock expansions were obtained:

$$R_{\mathrm{s}}(t)_{\mathrm{St.}} = c_{\mathrm{I}}\overline{\tau}_{\mathrm{s}}\left(\frac{t}{\alpha^{\pm}\overline{\tau}_{\mathrm{s}}}\right)^{n}\left[1 + a_2^{\pm}\left(\frac{t}{\alpha^{\pm}\overline{\tau}_{\mathrm{s}}}\right)^{2(1-n)} + a_3^{\pm}\left(\frac{t}{\alpha^{\pm}\overline{\tau}_{\mathrm{s}}}\right)^{4(1-n)} + \mathrm{H.O.T.}\right], \tag{2.153}$$

$$R_{\mathrm{s}}(t)_{\mathrm{W.,\ cyl.}} = c_{\mathrm{I}}\overline{\tau}_{\mathrm{w}}\left[\frac{-t}{\overline{\tau}_{\mathrm{w}}} + \sqrt{\frac{-t}{\overline{\tau}_{\mathrm{w}}}} - \frac{19+3\gamma}{16\,(\gamma+1)}\log\left(\frac{-t}{\overline{\tau}_{\mathrm{w}}}\right) + \overline{a}_2 + \mathrm{H.O.T.}\right], \tag{2.154}$$

$$R_{\mathrm{s}}(t)_{\mathrm{W.,\ sph.}} = c_{\mathrm{I}}\overline{\tau}_{\mathrm{w}}\left[\frac{-t}{\overline{\tau}_{\mathrm{w}}} + \log\left(\frac{-t}{\overline{\tau}_{\mathrm{w}}}\right) + \overline{a}_1 + \frac{\log\left(\frac{-t}{\overline{\tau}_{\mathrm{w}}}\right)}{\frac{-t}{\overline{\tau}_{\mathrm{w}}}} + \frac{\overline{a}_1 + \frac{\gamma+5}{\gamma+1}}{\frac{-t}{\overline{\tau}_{\mathrm{w}}}} + \mathrm{H.O.T.}\right], \tag{2.155}$$

for the strong shock expansion and the weak shock expansions in the cylindrical and spherical cases, respectively. The constants n, α^+, a_2^-, a_2^+, a_3^-, and a_3^+ in the strong shock equations are found using the method described in Section 2.3. The constants $\overline{\tau}_{\mathrm{s}}$ and $\overline{\tau}_{\mathrm{w}}$ are proportional to τ, which is defined by Equation 1.18. The values of $\frac{\overline{\tau}_{\mathrm{s}}}{\tau}$, $\frac{\overline{\tau}_{\mathrm{w}}}{\tau}$, $\overline{a}_1$, and $\overline{a}_2$ cannot be found by just considering the expansions. To find them, a computation needs to be done using another technique. This will be done in Chapter 3.

The limiting characteristic, that is, the boundary of the flow influencing the incoming shock (region II), is of particular importance since it leads to singularities in the $(r,\ \eta)$ plane. This limiting characteristic lies at a finite η ($\eta = \eta^*$) for the strong shock case and at $\eta = 1$ in the weak shock expansion case.

The values of all constants (n, α^+, a_2^-, a_2^+, a_3^-, a_3^+, η^*, $\frac{\overline{\tau}_{\mathrm{s}}}{\tau}$, $\overline{a}_1$, $\overline{a}_2$, and $\frac{\overline{\tau}_{\mathrm{w}}}{\tau}$) are given in Appendix E. The functions F, G, and K that were defined in Section 1.2 do not involve the constant τ and are invariant for given ν and γ. The expansions of these functions are given in Appendix D.1.

Chapter 3

Incoming Shock Complete Solution

In the previous chapter, we investigated the limiting behaviors of the problem and we obtained solutions that included unknown constants. These particular constants are $\frac{\overline{\tau}_{\rm s}}{\tau}$ in the strong shock expansion, $\frac{\overline{\tau}_{\rm w}}{\tau}$ and $\overline{a}_2$ in the weak shock expansion in the cylindrical case, and $\frac{\overline{\tau}_{\rm w}}{\tau}$ and $\overline{a}_1$ in the weak shock expansion in the spherical case. These can only be determined with a complete calculation of the incoming shock problem. For that purpose, as well as to obtain the complete incoming solution, a program based on the characteristics method was written.

The equations used in the computation are shown in Section 3.1 and details about the program will be explained in Section 3.2. Results will be presented in Chapter 4.

3.1 Characteristic Equations

Since the program has to be able to compute the flow starting at $R_{\rm s} \gg c_{\rm I}\tau$ and ending at $R_{\rm s} \ll c_{\rm I}\tau$, computing the solution in real space (r, t) would be very inconvenient. To avoid that, the following change of variables is performed:

$$\theta = \frac{c_{\rm I} t}{R_{\rm s}(t)}, \tag{3.1}$$

$$\eta = \frac{R_{\rm s}(t)}{r}. \tag{3.2}$$

Under this change of variables, the infinite domain becomes a square-bounded domain with θ and η ranging from -1 to 0 and from 0 to 1, respectively (see Figure 3.1). The reason

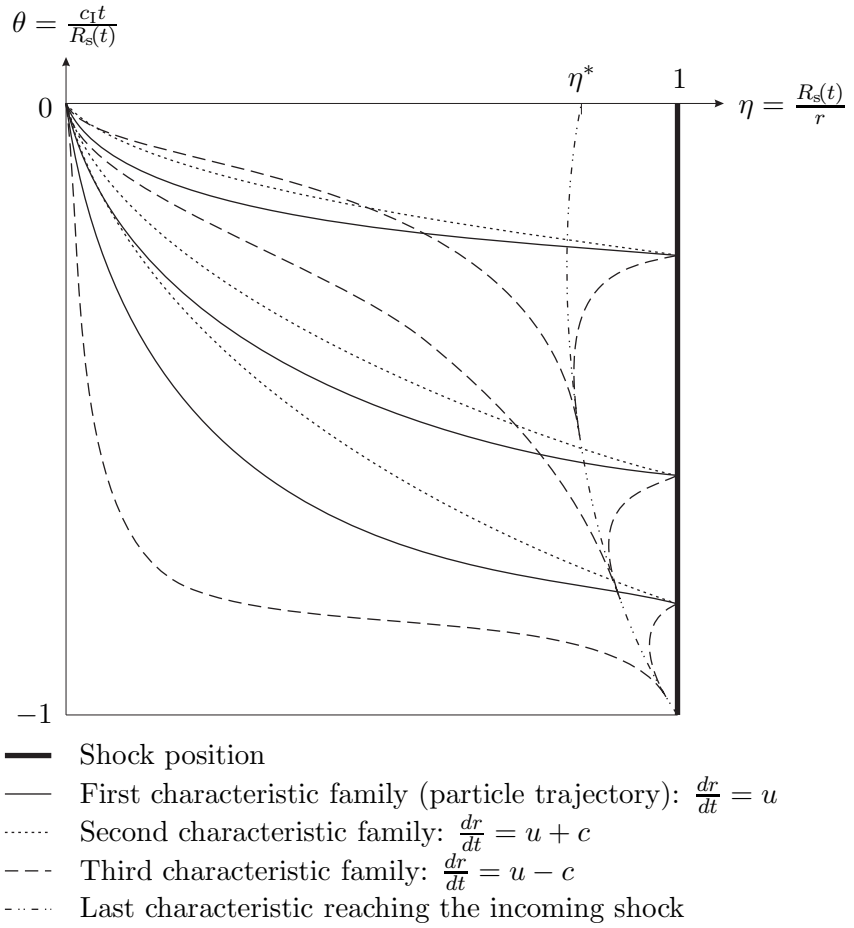

Figure 3.1: Sketch of the η–θ diagram for the problem in region II. The shock position is represented by the thick line. The three different kinds of characteristics are shown as well: $\frac{dr}{dt} = u$ (solid curves), $\frac{dr}{dt} = u + c$ (dotted curves), and $\frac{dr}{dt} = u - c$ (dashed curves), where u and c are the local velocity and speed of sound of the flow, respectively. η^* is the particular value of η at which we have a singularity in the strong shock series expansion.

for introducing θ follows logically from Equation 1.6. In fact, solving the problem, we will naturally find the unknown function $\theta = K\left(\nu, \gamma, \frac{U_s}{c_I}\right)$.

In Section 2.2.1, we saw that, close to the reflection point, the shock jump conditions give a finite density behind the shock, but that the pressure, the velocity and the shock speed tend to infinity. For a shock very close to the reflection point, we have that

$$P_{II}(1,\theta) \propto R_s^{\frac{2(n-1)}{n}} \propto \frac{1}{\theta^2}, \tag{3.3}$$

$$u_{II}(1,\theta) \propto R_s^{\frac{n-1}{n}} \propto \frac{1}{\theta}, \tag{3.4}$$

$$U_s(\theta) \propto R_s^{\frac{n-1}{n}} \propto \frac{1}{\theta}. \tag{3.5}$$

To avoid any singular values in the computational domain, the following new variables are used:

$$\overline{P}(\eta,\theta) = \theta^2 \frac{P_{\mathrm{II}}(\eta,\theta)}{P_{\mathrm{I}}}, \tag{3.6}$$

$$\overline{u}(\eta,\theta) = \theta \frac{u_{\mathrm{II}}(\eta,\theta)}{c_{\mathrm{I}}}, \tag{3.7}$$

$$\overline{c}(\eta,\theta) = \frac{\theta}{c_{\mathrm{I}}} \sqrt{\frac{\gamma P_{\mathrm{II}}(\eta,\theta)}{\rho_{\mathrm{II}}(\eta,\theta)}}, \tag{3.8}$$

$$\widetilde{U}_{\mathrm{s}}(\theta) = \theta \frac{U_{\mathrm{s}}(\theta)}{c_{\mathrm{I}}}. \tag{3.9}$$

Using these last changes of variable, the derivatives in (r, t) can be written in terms of derivatives in (η, θ):

$$\begin{aligned}
\frac{\partial}{\partial t} &= \frac{\partial \eta}{\partial t}\frac{\partial}{\partial \eta} + \frac{\partial \theta}{\partial t}\frac{\partial}{\partial \theta} \\
&= \frac{1}{r}\frac{\partial R_{\mathrm{s}}(t)}{\partial t}\frac{\partial}{\partial \eta} + c_{\mathrm{I}}\left[\frac{1}{R_{\mathrm{s}}(t)} - \frac{t}{{R_{\mathrm{s}}(t)}^2}\frac{\partial R_{\mathrm{s}}(t)}{\partial t}\right]\frac{\partial}{\partial \theta} \\
&= \frac{U_{\mathrm{s}}(t)}{r}\frac{\partial}{\partial \eta} + \frac{c_{\mathrm{I}}}{R_{\mathrm{s}}(t)}\left[1 - \frac{tU_{\mathrm{s}}(t)}{R_{\mathrm{s}}(t)}\right]\frac{\partial}{\partial \theta} \\
&= \frac{\frac{c_{\mathrm{I}}\widetilde{U}_{\mathrm{s}}(\theta)}{\theta}}{\frac{c_{\mathrm{I}}t(\theta)}{\eta\theta}}\frac{\partial}{\partial \eta} + \frac{c_{\mathrm{I}}}{\frac{c_{\mathrm{I}}t(\theta)}{\theta}}\left[1 - \frac{t(\theta)\,\frac{c_{\mathrm{I}}\widetilde{U}_{\mathrm{s}}(\theta)}{\theta}}{\frac{c_{\mathrm{I}}t(\theta)}{\theta}}\right]\frac{\partial}{\partial \theta} \\
&= \frac{\eta\widetilde{U}_{\mathrm{s}}(\theta)}{t(\theta)}\frac{\partial}{\partial \eta} + \frac{\theta}{t(\theta)}\left[1 - \widetilde{U}_{\mathrm{s}}(\theta)\right]\frac{\partial}{\partial \theta},
\end{aligned} \tag{3.10}$$

$$\begin{aligned}
\frac{\partial}{\partial r} &= \frac{\partial \eta}{\partial r}\frac{\partial}{\partial \eta} + \frac{\partial \theta}{\partial r}\frac{\partial}{\partial \theta} \\
&= -\frac{R_{\mathrm{s}}(t)}{r^2}\frac{\partial}{\partial \eta} \\
&= -\frac{\frac{c_{\mathrm{I}}t(\theta)}{\theta}}{\left(\frac{c_{\mathrm{I}}t(\theta)}{\theta\eta}\right)^2}\frac{\partial}{\partial \eta} \\
&= -\frac{\theta\eta^2}{c_{\mathrm{I}}t(\theta)}\frac{\partial}{\partial \eta}.
\end{aligned} \tag{3.11}$$

The new problem can now be formulated. After a few manipulations, the Euler equations become

$$\frac{\partial}{\partial \theta}\boldsymbol{v} + \boldsymbol{A}\frac{\partial}{\partial \eta}\boldsymbol{v} = \boldsymbol{b}, \tag{3.12}$$

where $\boldsymbol{v}$ is the vector of unknown variables,

$$\boldsymbol{v} = \begin{pmatrix} \overline{P}(\eta,\theta) \\ \overline{u}(\eta,\theta) \\ \overline{c}(\eta,\theta) \end{pmatrix}, \tag{3.13}$$

and where

$$\boldsymbol{A} = \frac{\eta}{\theta\left[\widetilde{U}_{\mathrm{s}}(\theta)-1\right]} \begin{pmatrix} \widetilde{U}_{\mathrm{s}}(\theta)-\eta\overline{u}(\eta,\theta) & -\gamma\eta\overline{P}(\eta,\theta) & 0 \\ -\frac{\eta\overline{c}(\eta,\theta)^2}{\gamma\overline{P}(\eta,\theta)} & \widetilde{U}_{\mathrm{s}}(\theta)-\eta\overline{u}(\eta,\theta) & 0 \\ 0 & -\frac{(\gamma-1)\eta\overline{c}(\eta,\theta)}{2} & \widetilde{U}_{\mathrm{s}}(\theta)-\eta\overline{u}(\eta,\theta) \end{pmatrix}, \tag{3.14}$$

$$\boldsymbol{b} = \frac{1}{\theta\left[\widetilde{U}_{\mathrm{s}}(\theta)-1\right]} \begin{pmatrix} \overline{P}(\eta,\theta)\left[\gamma\eta\left(\nu-1\right)\overline{u}(\eta,\theta)+2\left[\widetilde{U}_{\mathrm{s}}(\theta)-1\right]\right] \\ \overline{u}(\eta,\theta)\left[\widetilde{U}_{\mathrm{s}}(\theta)-1\right] \\ \frac{\overline{c}(\eta,\theta)\left[(\gamma-1)\eta(\nu-1)\overline{u}(\eta,\theta)+2\left[\widetilde{U}_{\mathrm{s}}(\theta)-1\right]\right]}{2} \end{pmatrix}. \tag{3.15}$$

Let the superscript T refer to the transpose of a matrix or a vector. According to the characteristics method, the eigenvalues (λ_i) and the associated eigenvectors ($\boldsymbol{e}_i$) of the matrix $\boldsymbol{A}^{\mathrm{T}}$ are of particular importance to find the differential equations along the characteristics. In fact if we pre-multiply the system of differential equations 3.12 by $\boldsymbol{e}_i^{\mathrm{T}}$, the following equation can be written:

$$\boldsymbol{e}_i^{\mathrm{T}}\frac{\partial}{\partial\theta}\boldsymbol{v} + \boldsymbol{e}_i^{\mathrm{T}}\boldsymbol{A}\frac{\partial}{\partial\eta}\boldsymbol{v} = \boldsymbol{e}_i^{\mathrm{T}}\boldsymbol{b}. \tag{3.16}$$

Since

$$\boldsymbol{e}_i^{\mathrm{T}}\boldsymbol{A} = \left(\boldsymbol{A}^{\mathrm{T}}\boldsymbol{e}_i\right)^{\mathrm{T}} = \left(\lambda_i\boldsymbol{e}_i\right)^{\mathrm{T}} = \lambda_i\boldsymbol{e}_i^{\mathrm{T}}, \tag{3.17}$$

we get

$$\boldsymbol{e}_i^{\mathrm{T}}\left(\frac{\partial}{\partial\theta} + \lambda_i\frac{\partial}{\partial\eta}\right)\boldsymbol{v} = \boldsymbol{e}_i^{\mathrm{T}}\boldsymbol{b}, \tag{3.18}$$

which is equivalent to saying that

$$\boldsymbol{e}_i^{\mathrm{T}}\frac{d}{d\theta}\boldsymbol{v} = \boldsymbol{e}_i^{\mathrm{T}}\boldsymbol{b}, \tag{3.19}$$

on

$$\frac{d\eta}{d\theta} = \lambda_i. \tag{3.20}$$

The first eigenvalue and its associated eigenvector are

$$\lambda_1 = -\frac{\eta\left[\widetilde{U}_{\mathrm{s}}(\theta) - \eta\overline{u}(\eta,\theta)\right]}{\theta\left[\widetilde{U}_{\mathrm{s}}(\theta) - 1\right]}, \tag{3.21}$$

$$\boldsymbol{e}_1 = \begin{pmatrix} -\frac{(\gamma-1)\overline{c}(\eta,\theta)}{2\gamma\overline{P}(\eta,\theta)} \\ 0 \\ 1 \end{pmatrix}. \tag{3.22}$$

Using the results from Equations 3.19 and 3.20, we can get after a few manipulations that

$$\frac{\overline{P}(\eta,\theta)^{\gamma-1}}{\theta^2\overline{c}(\eta,\theta)^{2\gamma}} = \text{Const}, \tag{3.23}$$

on

$$\frac{d\eta}{d\theta} = -\frac{\eta\left[\widetilde{U}_{\mathrm{s}}(\theta) - \eta\overline{u}(\eta,\theta)\right]}{\theta\left[\widetilde{U}_{\mathrm{s}}(\theta) - 1\right]}. \tag{3.24}$$

This is equivalent to saying that the entropy has to remain constant on a particle trajectory. The characteristics corresponding to these equations are represented by solid curves in all the figures.

The two other eigenvalues and eigenvectors are given by

$$\lambda_k = -\frac{\eta\left[\widetilde{U}_{\mathrm{s}}(\theta) - \eta\left[\overline{u}(\eta,\theta) + \epsilon\overline{c}(\eta,\theta)\right]\right]}{\theta\left[\widetilde{U}_{\mathrm{s}}(\theta) - 1\right]}, \tag{3.25}$$

$$\boldsymbol{e}_k = \begin{pmatrix} \epsilon\frac{\overline{c}(\eta,\theta)}{\gamma\overline{P}(\eta,\theta)} \\ 1 \\ 0 \end{pmatrix}, \tag{3.26}$$

with $k = 2$ and $\epsilon = 1$ for the second family characteristics, and $k = 3$ and $\epsilon = -1$ for the third family characteristics. These two characteristics are represented by the dotted and the dashed curves in the figures. They correspond to the characteristics $\frac{dx}{dt} = u + \epsilon c$ in the

x–y plane. Note that the third characteristic family ($\epsilon = -1$, dashed lines in the figures) is the only one that can reach the incoming shock from region II. The last two characteristic differential equations are

$$\frac{d}{d\theta}\overline{u}(\eta,\theta) + \epsilon\frac{\overline{c}(\eta,\theta)}{\gamma\overline{P}(\eta,\theta)}\frac{d}{d\theta}\overline{P}(\eta,\theta) = \frac{1}{\theta}\left[\overline{u}(\eta,\theta) + \epsilon\overline{c}(\eta,\theta)\left[\frac{2}{\gamma} + \frac{\eta\,(\nu-1)\,\overline{u}(\eta,\theta)}{\widetilde{U}_{\rm s}(\theta)-1}\right]\right], \quad (3.27)$$

on

$$\frac{d\eta}{d\theta} = -\frac{\eta\left[\widetilde{U}_{\rm s}(\theta) - \eta\left[\overline{u}(\eta,\theta) + \epsilon\overline{c}(\eta,\theta)\right]\right]}{\theta\left[\widetilde{U}_{\rm s}(\theta) - 1\right]}. \quad (3.28)$$

To be able to start the computation, the weak shock expansion solution is used for $\theta \ll 1$ (see Section 2.4) and the characteristics coming from the shock can be obtained using the shock jump conditions:

$$\overline{P}(1,\theta) = \frac{2\gamma\widetilde{U}_{\rm s}(\theta)^2 - (\gamma-1)\,\theta^2}{\gamma+1}, \quad (3.29)$$

$$\overline{u}(1,\theta) = \frac{2}{\gamma+1}\frac{\widetilde{U}_{\rm s}(\theta)^2 - \theta^2}{\widetilde{U}_{\rm s}(\theta)}, \quad (3.30)$$

$$\overline{c}(1,\theta) = \frac{\sqrt{\left[2\gamma\widetilde{U}_{\rm s}(\theta)^2 - (\gamma-1)\,\theta^2\right]\left[(\gamma-1)\,\widetilde{U}_{\rm s}(\theta)^2 + 2\theta^2\right]}}{\widetilde{U}_{\rm s}(\theta)\,(\gamma+1)}. \quad (3.31)$$

The implementation of these equations will be explained in more detail in the next section.

3.2 Implementation of the Method of Characteristics

As discussed in Section 3.1, the program was designed to have several key features. First, since the velocity and pressure become singular at the point of reflection, the equations need to be rewritten to avoid these singularities. Furthermore, since we need to compute the solution starting at a very large shock radius (and so a very large negative time) and since we need to pursue the calculation until the shock is very close to the reflection point, new independent variables needed to be introduced.

In addition, as seen in Figure 3.1, all the third family characteristics start at (θ, η) =

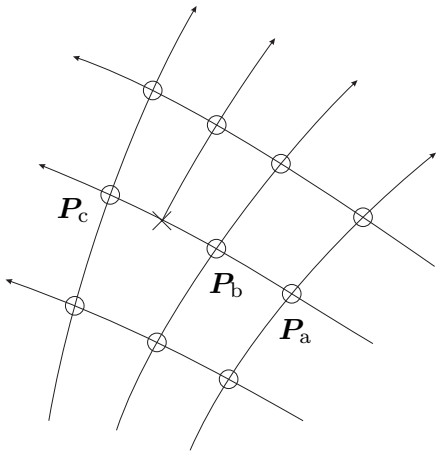

○ Node calculated by the characteristics method

× Interpolated node

Figure 3.2: Addition of a characteristic. Since the distance between two successive characteristics of the same family becomes too big, a new node is interpolated on a characteristic of the other family. The regular nodes are marked with circles, and the interpolated node is shown with a cross. Since the characteristic computations are only first order accurate, the interpolation was chosen to be second order. In this case, to find the interpolated node, the nodes $\boldsymbol{P}_\mathrm{a}$, $\boldsymbol{P}_\mathrm{b}$ and $\boldsymbol{P}_\mathrm{c}$ are used.

$(-1, 1)$. This means that the whole problem is defined in that singular point. Since it is impossible to start there, the program needs to start at $\theta + 1 \ll 1$ so that the weak shock series expansion can be used as a first guess. Note also that although at finite but small $\theta + 1$ the third family characteristics that influence the shock are not merged into a point anymore; they remain within a very narrow range of η. Since all the characteristics going to the shock start from that narrow range, we can choose between two different methods to find the solution.

In the first method, the distance between the characteristics at the initial θ is very small and the characteristics are spreading apart when θ increases. For example, a calculation ($\nu = 2$, $\gamma = 1.4$) was made using this method. The characteristics were initiated at $\theta = -0.995$ and spaced by $\Delta\eta = 4 \times 10^{-15}$. Although this initial spacing was small, the characteristics reaching the shock around $\theta = -0.05$ were spaced by $\Delta\theta = 0.005$ at the shock. This means that to have good accuracy close to the reflection point, the characteristics have to be spaced by just more than the precision of the numbers. This method leads to calculations that are much longer than necessary.

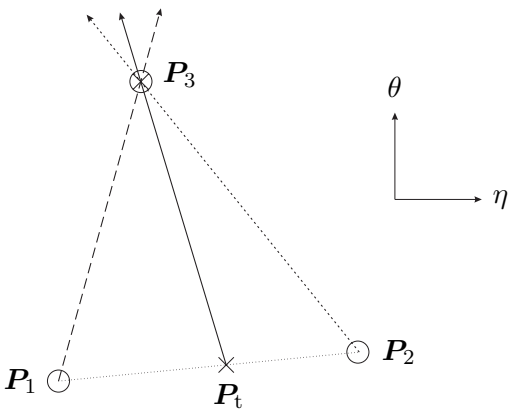

—— First characteristic family (particle trajectory): $\frac{dr}{dt} = u$
····· Second characteristic family: $\frac{dr}{dt} = u + c$
– – – Third characteristic family: $\frac{dr}{dt} = u - c$
◯ Known nodes
⊗ Unknown node
× Temporary node

Figure 3.3: Calculation of a node inside the domain using characteristics. $\boldsymbol{P}_1$ and $\boldsymbol{P}_2$ are two known nodes, $\boldsymbol{P}_\mathrm{t}$ is a temporary node used during the calculations, and $\boldsymbol{P}_3$ is the new node.

The second solution is more complicated but decreases the amount of computational work by increasing the initial spacing of the characteristics. If during the calculation, the spacing of two successive characteristics of the same family becomes excessive, a new characteristic is initiated between them by creating a node that is interpolated along a characteristic of the other family. This method was implemented in this work and is explained graphically in Figure 3.2. To avoid losing accuracy during the process, the interpolation has to be of an order that is at least as high as the order of the characteristic computations.

In the domain, nodes are evaluated using a first-order method. Figure 3.3 shows a sketch of the process. First starting from $\boldsymbol{P}_1$ and $\boldsymbol{P}_2$, the position of $\boldsymbol{P}_3$ is evaluated using the slopes of the third characteristic at $\boldsymbol{P}_1$ and of the second characteristic at $\boldsymbol{P}_2$ (Equation 3.28). Then using the differential equations on these characteristics, we obtain $\overline{P}$ and $\overline{u}$ at the new node (Equation 3.27). Since it does not involve the unknown value $\overline{c}$, the trajectory slope at the new node can be evaluated (Equation 3.24). The position of a temporary node is then found. This node is the intersection to first-order of the trajectory passing through the new node $\boldsymbol{P}_3$ and the segment joining the two initial nodes $\boldsymbol{P}_1$ and $\boldsymbol{P}_2$. By using a

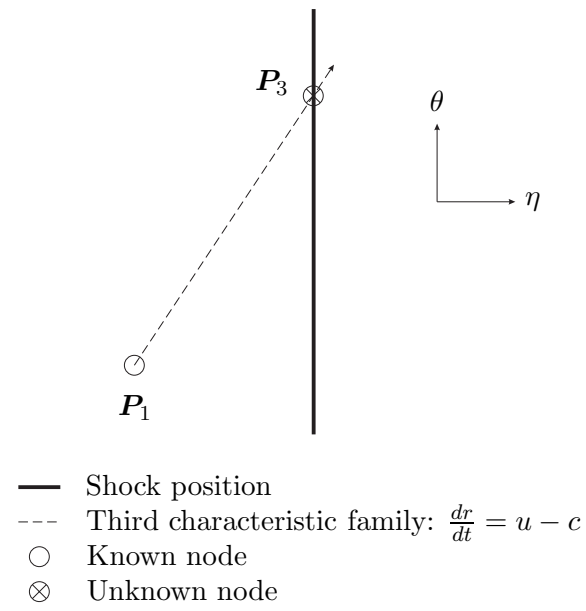

Figure 3.4: Calculation of a node on the shock using characteristics. $\boldsymbol{P}_1$ is a known node and $\boldsymbol{P}_3$ is the new node.

simple first-order interpolation, the value of the entropy can be estimated at the temporary node. Since this value remains constant on a particle trajectory (Equation 3.23), we obtain the value of $\overline{c}$. Finally a corrector step is performed on the whole process. Although we are using this last corrector step, the algorithm remains of first-order accuracy since the interpolation between $\boldsymbol{P}_1$ and $\boldsymbol{P}_2$ is still linear.

When a third family characteristic reaches the shock, a different process is used (see Figure 3.4). First, the slope of the third family characteristic at the node $\boldsymbol{P}_1$ is evaluated using Equation 3.28. The intersection with the shock, $\boldsymbol{P}_3$, can then easily be calculated. The values of $\widetilde{U}_\mathrm{s}$, $\overline{P}$, $\overline{u}$, and $\overline{c}$ are found by satisfying the differential equation along the characteristic (Equation 3.27) as well as the three shock jump conditions (Equations 3.29 to 3.31). Once again, a corrector step is performed on the whole process.

Note that $\widetilde{U}_\mathrm{s}(\theta)$ is evaluated at the shock. Since the equations in the (η, θ) plane also involve $\widetilde{U}_\mathrm{s}(\theta)$, these values are interpolated using third-order splines on the shock values. In addition, to avoid extrapolations of $\widetilde{U}_\mathrm{s}(\theta)$ far from the range of calculated shock nodes, the computation progresses one characteristic of the third family at a time (see Figure 3.5).

To start the computation, the weak shock solution is used at a value of θ that is close to -1. Written in the (η, θ) coordinates, only one unknown constant appears in the initial

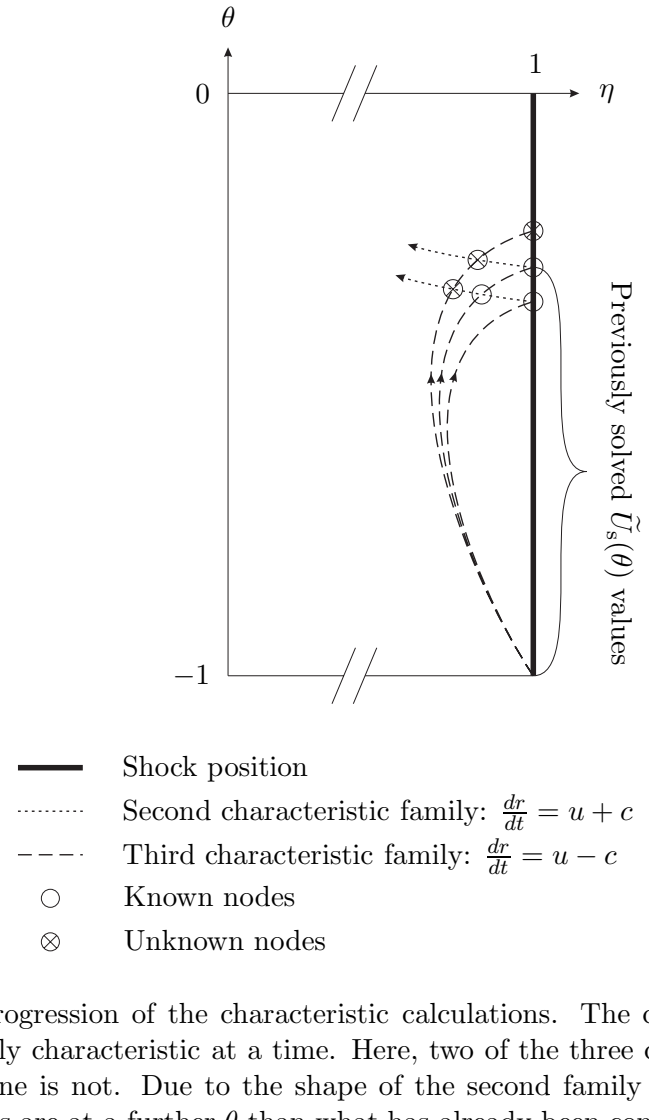

Figure 3.5: Progression of the characteristic calculations. The calculation is progressing one third family characteristic at a time. Here, two of the three characteristics are known and the last one is not. Due to the shape of the second family characteristics, only two unknown nodes are at a further θ than what has already been computed on the shock, and so only one $\widetilde{U}_s(\theta)$ value needs to be extrapolated. The other node is on the shock and its $\widetilde{U}_s(\theta)$ value is not extrapolated but calculated using the characteristics method.

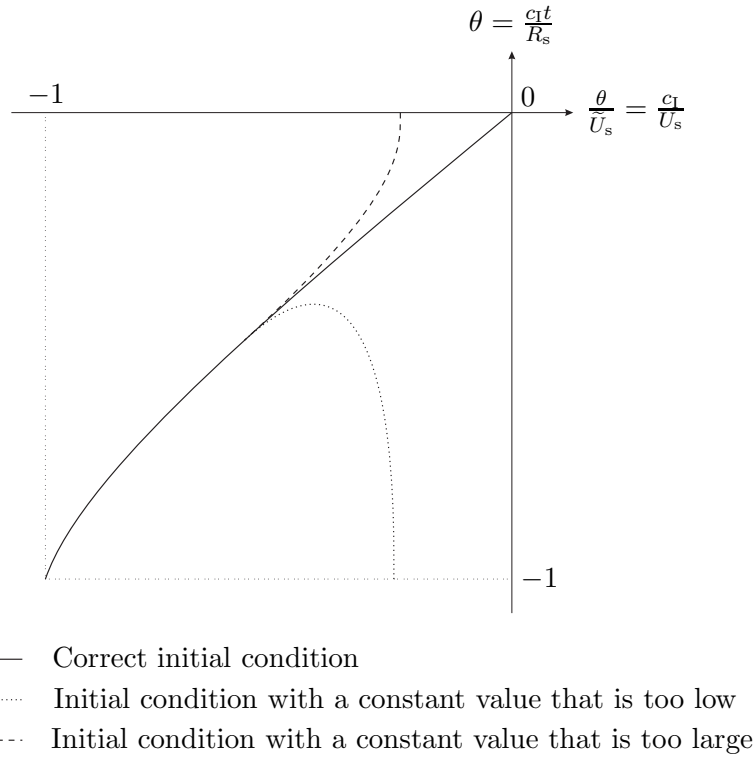

Figure 3.6: Bisection method to determine the initial condition constant. If the constant value is correct, we obtain a curve that tends to (0, 0), this is shown by the full curve. If the constant value is too low, the curve tends to infinity since R_s tends to 0 before the time does (dotted curve). If the constant value is too high, it is the opposite and the curve reaches $\theta = 0$, while $\widetilde{U}_s$ remains finite (dashed curve).

conditions (the time shift $\overline{a}_2$ in the cylindrical case and $\overline{a}_1$ in the spherical case), since the ratio $\frac{\overline{\tau}_\mathrm{w}}{\tau}$ does not appear anymore. If the constant had the correct value, the problem could theoretically be integrated up to the reflection point and θ would tend to 0 at the same time as $\frac{c_\mathrm{I}}{U_\mathrm{s}}$. If the guessed value is too low, the integration leads to a shock radius that tends to 0 before time reaches 0. This means that θ will tend to infinity. On the other hand, if the value is too big, the time tends to 0 before the shock radius and we get a θ that tends to 0 for a finite value of $\frac{c_\mathrm{I}}{U_\mathrm{s}}$. A bisection method was used to obtain the correct constant value.

To find the ratios $\frac{\overline{\tau}_\mathrm{w}}{\tau}$ and $\frac{\overline{\tau}_\mathrm{s}}{\tau}$, the following equation is integrated starting at a Mach number close to 1,

$$\frac{dR_\mathrm{s}}{dt} = U_\mathrm{s}, \tag{3.32}$$

or

$$\frac{1}{c_\mathrm{I}}\frac{dR_\mathrm{s}}{dt} = \frac{\widetilde{U}_\mathrm{s}(\theta)}{\theta} = \frac{\widetilde{U}_\mathrm{s}\left(\frac{c_\mathrm{I}t}{R_\mathrm{s}}\right)}{\frac{c_\mathrm{I}t}{R_\mathrm{s}}}. \tag{3.33}$$

The initial conditions (R_s, t) can be random and the value of $\overline{\tau}_\mathrm{w}$ is arbitrarily chosen, since the unknown ratios should be independent of the initial conditions. Once integrated, the equation gives $\frac{R_\mathrm{s}(t)}{c_\mathrm{I}}$. From there, it is easy to find the functions F and G used in Equations 1.19 and 1.26, respectively. Then τ can be obtained by using $\tau = \frac{R_\mathrm{s}^\star}{c_\mathrm{I}F\left(\nu,\gamma,\overline{U}_\mathrm{s}^\star\right)}$. Fitting the strong shock expansion result to the curve, we finally get $\overline{\tau}_\mathrm{s}$. Once all this is performed, the ratios $\frac{\overline{\tau}_\mathrm{w}}{\tau}$ and $\frac{\overline{\tau}_\mathrm{s}}{\tau}$ can be evaluated.

Results of the unknown constants ($\overline{a}_2$ in the cylindrical case, $\overline{a}_1$ in the spherical case, $\frac{\overline{\tau}_\mathrm{w}}{\tau}$, and $\frac{\overline{\tau}_\mathrm{s}}{\tau}$) are shown in Appendix E. It is important to know that the accuracy of these results is not very high since the integration is only first order and that, for example, the constant in the initial conditions ($\overline{a}_1$ or $\overline{a}_2$), does not appear in any dominant terms. But even though the accuracy is not high, the bisection method has to find the appropriate value with a high number of significant digits so that the characteristics can be computed up to a value of θ that is close to 0. In other words, this means that although we need to find a value that is accurate to about 10^{-10} to have a solution up to very strong shocks without having any singular behavior, this value will highly depend on the integration scheme that is used in the computation, and therefore, will have a relatively low accuracy if we compare

it with its exact theoretical value.

3.3 Summary

The program that was described in this chapter allows for the computation of the complete incoming shock problem using a first-order characteristics method. The initial conditions are taken from the weak shock expansion. In the coordinates that are used in the program, these conditions involve only one unknown constant ($\overline{a}_2$ in the cylindrical case and $\overline{a}_1$ in the spherical case). This constant represents a time shift that has to be found by iterations such that $R_{\mathrm{s}}(0) = 0$.

Once the characteristics problem is solved, the two unknown constant ratios ($\frac{\overline{\tau}_{\mathrm{s}}}{\tau}$ and $\frac{\overline{\tau}_{\mathrm{w}}}{\tau}$) are found by first integrating the equation

$$\frac{1}{c_{\mathrm{I}}}\frac{dR_{\mathrm{s}}}{dt} = \frac{\widetilde{U}_{\mathrm{s}}\left(\frac{c_{\mathrm{I}}t}{R_{\mathrm{s}}}\right)}{\frac{c_{\mathrm{I}}t}{R_{\mathrm{s}}}}, \tag{3.34}$$

where $\widetilde{U}_{\mathrm{s}}\left(\frac{c_{\mathrm{I}}t}{R_{\mathrm{s}}}\right)$ was found during the characteristics computations. Since the constant ratios are independent of the initial condition, the initial conditions for this integration can be arbitrarily chosen. Once integrated, the expansion solutions can be matched to the solution and the desired ratios can be obtained.

All the constant values are presented in Appendix E and some further results will be presented in Chapter 4.

Chapter 4

Results

In this chapter, the series expansion calculations will be compared to the characteristic results. In addition, some comparisons will include computational fluid dynamic calculations of the Euler equations. These were done by Christopher A. Mouton in the AMRITA environment [26].

The strong shock series expansion coefficients were calculated using 2,000 points in region II, 2,000 points in region III, and 1,000 points in region IV. The weak shock expansions where obtained analytically using the results shown in Appendix D.

We will compare some aspects of the results obtained by each method in the following sections. First, actual characteristics will be shown in the (η, θ) plane (Section 4.1). Then, the Euler solver will be briefly described (Section 4.2). The density, the pressure, and the velocity distributions will be compared between Euler calculations and the series expansions (Section 4.3). Finally, the non-dimensional functions F, G, and K that were defined in Section 1.2 will be compared between the different methods (Section 4.4).

4.1 Characteristic Results

Numerical calculations were performed using the characteristics method described in Chapter 3. The calculations were started at $\theta = -0.995$ and went to at least -0.1. In this section, two characteristic results will be presented to show the basic shapes of the second and third characteristic family. Both of these calculations were made with a specific heat ratio, γ, of 1.4. The first calculation has a cylindrical symmetry (Figure 4.1), and the second has

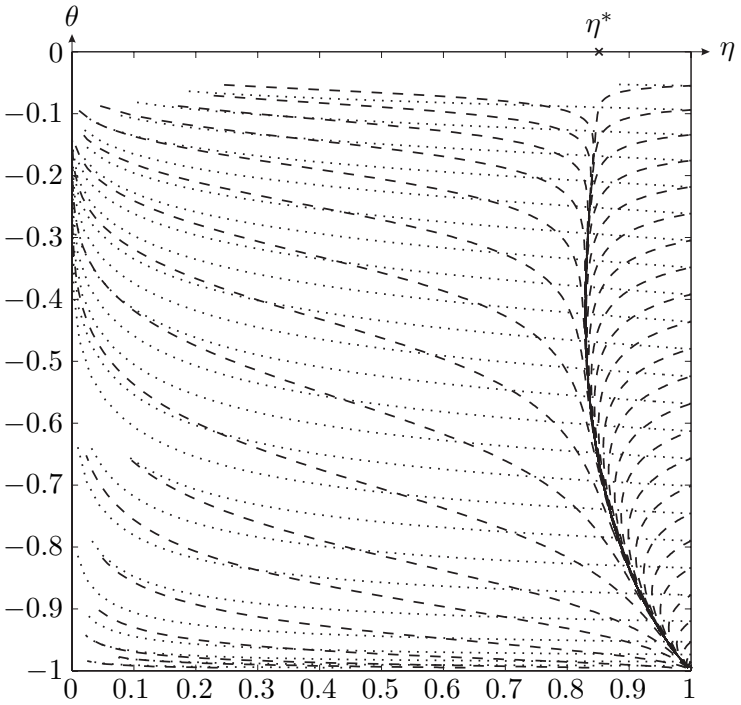

Figure 4.1: Second and third characteristic families in the cylindrical shock case for $\gamma = 1.4$. Dotted and dashed curves represent characteristics of the second and the third families, respectively. The cross represents the limit of the last characteristic reaching the incoming shock. This limit corresponds to the value of η at the singular point in region II in the strong shock series expansion.

a spherical symmetry (Figure 4.2). On each of the figures, some characteristics are shown. Characteristics of the second family are shown with dotted curves and characteristics of the third family are represented with dashed curves. The particular characteristic that separates the portion of the flow in region II that influences the shock from the rest is clearly distinguishable. The limit of this particular characteristic for θ tending to 0 is given in the strong shock expansion calculation since it corresponds to the value of η at the singularity (η^*). This limit is represented by a cross on the figures. Due to the singular behavior of the characteristics close to $\eta = 0$ and to $\theta = 0$, the characteristics could not be computed in the whole domain and were cropped, as seen in the figures.

The figures presented here were done without adding new characteristics inside the domain and this is why the computation had to be stopped at a θ of approximately -0.1. For the results presented in Section 4.4, the characteristic addition feature described in Section 3.2 was used and the computations could go much further. The initial θ was fixed

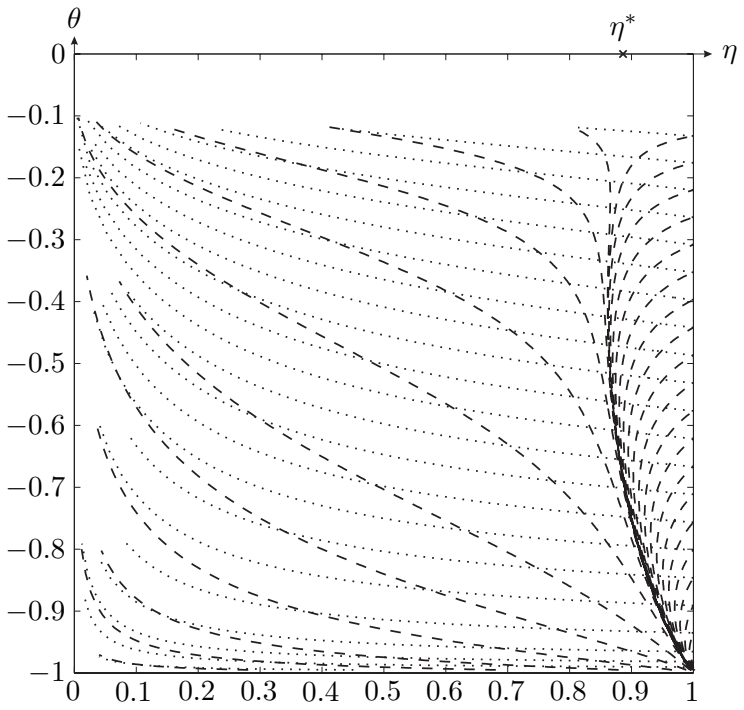

Figure 4.2: Second and third characteristic families in the spherical shock case for $\gamma = 1.4$. Dotted and dashed curves represent characteristics of the second and the third families, respectively. The cross represents the limit of the last characteristic reaching the incoming shock. This limit corresponds to the value of η at the singular point in region II in the strong shock series expansion.

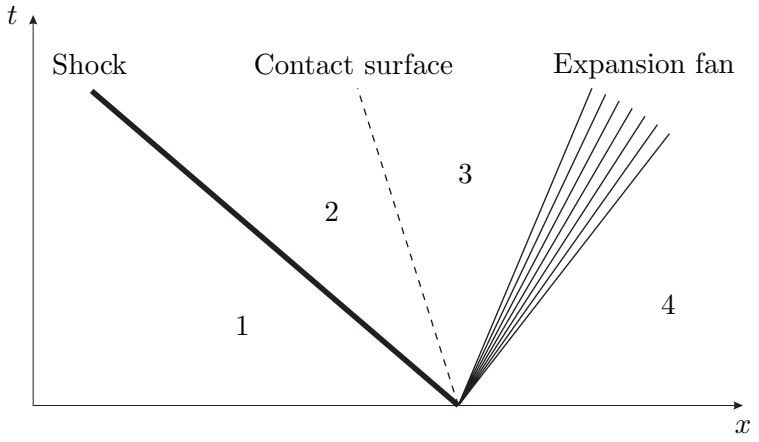

Figure 4.3: x–t diagram of a standard shock tube. The initial conditions of the Euler calculations are equivalent to that of a shock tube that does not produce a contact surface (meaning that the flow properties in 2 are the same as the flow properties in 3).

at -0.995 for all the cases. In the cylindrical case, the characteristics program reached a θ of -0.0338 and of -0.0354 in the $\gamma = 1.4$ and $\gamma = \frac{5}{3}$ cases, respectively. These values represent shock radius ratios between the final and the initial points of about 2×10^{-12} and 1.5×10^{-11}, or shock Mach numbers ranging from 1.00257 to 24.6 and from 1.00257 to 22.9. In the spherical case, the computation went up to $\theta = -0.0426$ and $\theta = -0.0126$ in the $\gamma = 1.4$ and $\gamma = \frac{5}{3}$ cases, respectively, which corresponds to shock radius ratios of 8.6×10^{-7} and 1.3×10^{-7}, and to shock Mach numbers ranging from 1.000772 to 17.54 and from 1.000763 to 57.64.

4.2 Euler Computations

Some computational results were produced using an Euler solver. The problem was started in the same way as a shock tube, the diaphragm being cylindrical or spherical. The initial pressure and density jumps were chosen such that the shock starts at a particular desired Mach number and that the gas properties are continuous across the contact surface during the startup process. In the standard x–t diagram of a shock tube shown in Figure 4.3, this means that $\rho_2 = \rho_3$. This condition and the initial Mach number of the shock give two equations that can be solved for $\frac{P_4}{P_1}$ and $\frac{\rho_4}{\rho_1}$. Although the problem should be started with a non-uniform flow behind the shock, like what was done to start the characteristic program

in Chapter 3, these simplified initial conditions lead to very good results. In fact, a well-known feature of the imploding shock problem is that the details of the initial conditions have little influence on the results. This feature was discovered very early by Payne, in 1957 [27]. He obtained numerical results that agreed very well with Guderley, even though his initial conditions were completely different from what they should be if the shock was supposed to have come from infinity.

The problem was computed as a one-dimensional problem using a Roe solver. The 10,000 cells were uniformly distributed. Adaptive mesh refinement with four levels was used, each of these splitting a cell into five smaller ones. To obtain a lot of discretized data close to the origin, the CFL number ($\frac{c_{\max}\Delta t}{\Delta r}$) was decreased continuously from 0.7 to 0.1 while the shock approached the origin and was increased continuously to its original value when the reflected shock moved away from the origin. The shock is initiated at the 5,000th coarse grid cell.

In the spherical symmetry case, the shock strengthens too quickly close to the origin, and the very high gradients lead eventually to an early abortion of the computation. For that reason, a small solid sphere of size 1 was placed in the center of the computational domain. This sphere does not affect the results in general, but its influence can be high in the reflected shock case close to the origin.

4.3 ρ, P, and u Distribution

Comparisons of the variable distributions were made between the strong shock expansion and the Euler calculations. These comparisons can easily be made using the formulae from Appendix D.2. The variables ρ, P, u, and t are normalized by ρ_{I}, $\rho_{\mathrm{I}}\left|U_{\mathrm{s}}(r)^{-}\right|^2$, $\left|U_{\mathrm{s}}(r)^{-}\right|$, and $\left|t_{\mathrm{s}}(r)^{-}\right|$, respectively. In these expressions, $U_{\mathrm{s}}(r)^{-}$ represents the speed of the incoming shock when it crosses the radius r, and $t_{\mathrm{s}}(r)^{-}$ is the time at which that incoming shock passes r.

Comparisons are made for two specific heat ratios, these are $\gamma = 1.4$ and $\gamma = \frac{5}{3}$. In both cylindrical cases, the shock was initiated at a Mach number of 10 and the variables were analyzed at a radius 20 times smaller than the initial radius. This corresponds to incoming

shock Mach numbers of 18.1 and of 19.8 in the $\gamma = 1.4$ case (Figure 4.4) and in the $\gamma = \frac{5}{3}$ case (Figure 4.5), respectively. In the spherical case, the initial shock Mach number was 5 in the $\gamma = 1.4$ case and 10 in the $\gamma = \frac{5}{3}$ case, and the variables were taken at a radius 10 times smaller than the initial radius. This leads to incoming shock Mach numbers of 12.4 and of 28.7 in the $\gamma = 1.4$ case (Figure 4.6) and in the $\gamma = \frac{5}{3}$ case (Figure 4.7), respectively.

Figures 4.4 to 4.7 show the variation over time of the normalized density, pressure and velocity. Guderley's solution is accurate for very high Mach numbers, but at the current Mach numbers, it shows some discrepancies from the Euler results. Most of these discrepancies appear in the density and the pressure distributions, and are highly reduced when adding two more terms in the expansion. As explained previously, the shock series expansions are accurate for a low shock radius ($R_s \ll c_I \tau$). But this also means that the variables at a given small radius will only be valid for small times ($t \ll \tau$). In fact, at later times, the shock is too far from the origin to be accurately modeled and so its influence is badly represented. This can be seen in Figure 4.5 for the density and the pressure distributions since the series expansions start to diverge from the exact solutions as time progresses. Note also that it may seem that Guderley's solution is better in some cases, but this is purely coincidencial. The addition of the two next terms in the series always improve on Guderley's solution for sufficiently large Mach numbers and this is especially true for regions II and III and right downstream of the reflected shock in region IV.

4.4 The Non-Dimensional Functions F, G, and K

The functions F, G, and K were introduced in Section 1.2. Given the symmetry of the problem, ν, and specific heat ratio, γ, these functions are fully described. They are particularly useful since they are unique for all possible shock trajectories. The weak and strong series expansions of these functions will be compared to the characteristics results and the Euler solutions. The results will be presented for both the axisymmetric and the spherical shock cases and for each of these cases, two different values of γ will be considered (1.4 and $\frac{5}{3}$). The Euler computation were made using a grid of 10,000 cells. The shock was initially started at the 5,000th cell. The initial shock Mach number was set to 1.2 and 1.15 in the

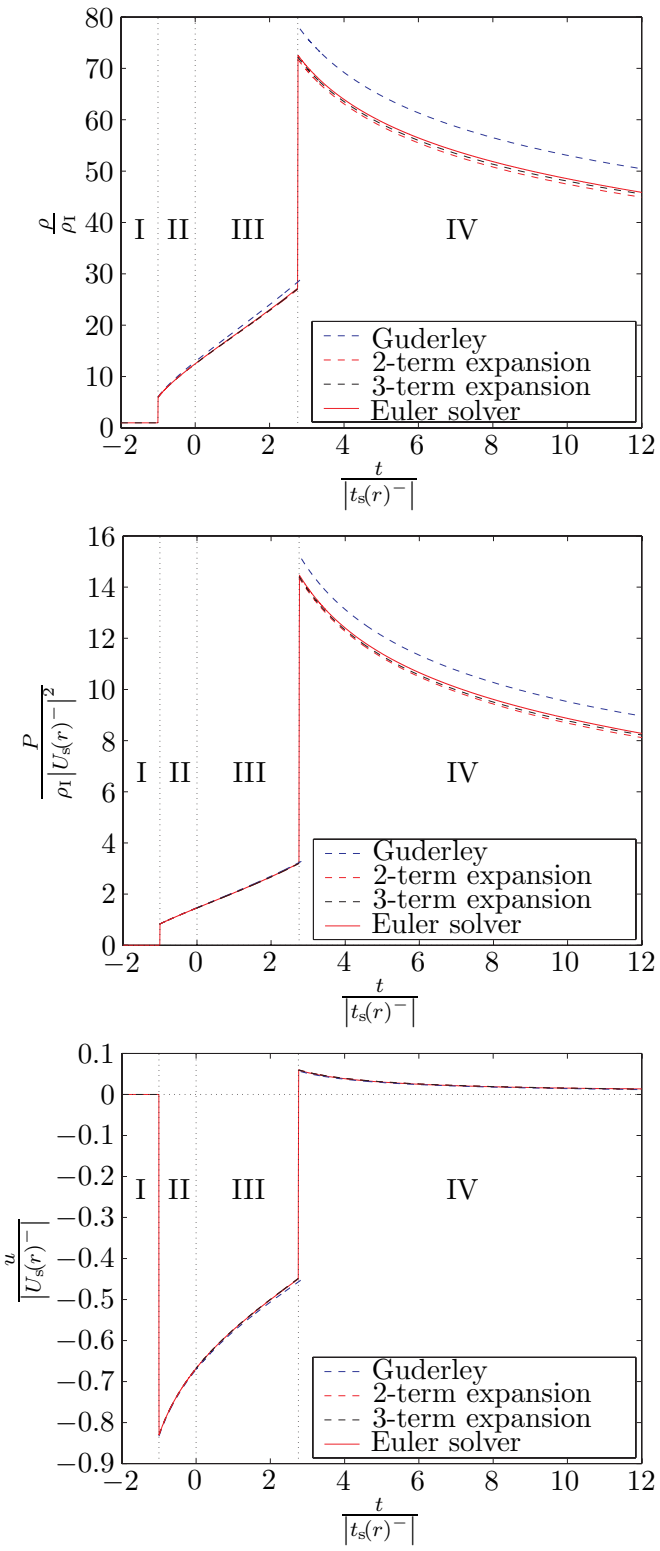

Figure 4.4: Normalized density, pressure, and velocity distributions versus normalized time for a cylindrical imploding shock ($\gamma = 1.4$). The calculations were started with a shock Mach number of 10 and the measurements were taken at a radius 20 times smaller than the initial radius (where the incoming shock Mach number is 18.1).

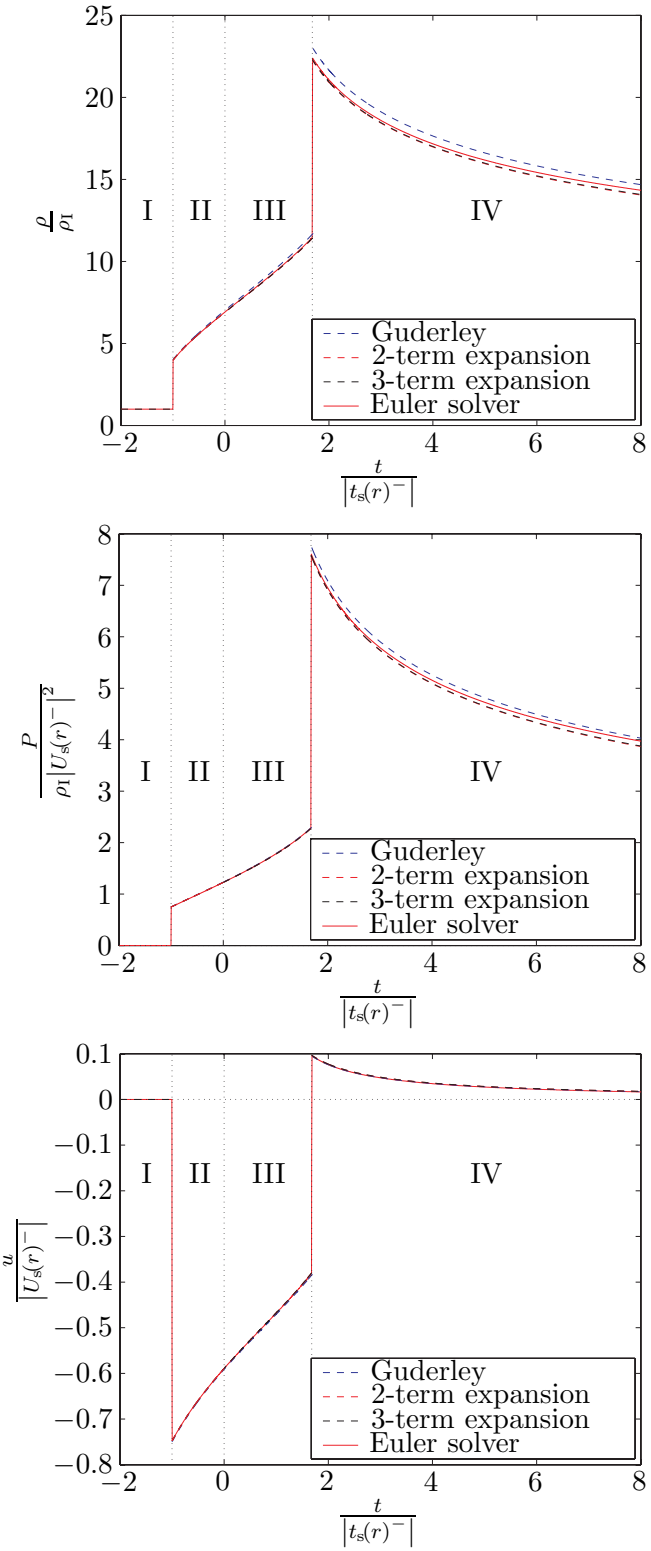

Figure 4.5: Normalized density, pressure, and velocity distributions versus normalized time for a cylindrical imploding shock ($\gamma = \frac{5}{3}$). The calculations were started with a shock Mach number of 10 and the measurements were taken at a radius 20 times smaller than the initial radius (where the incoming shock Mach number is 19.1).

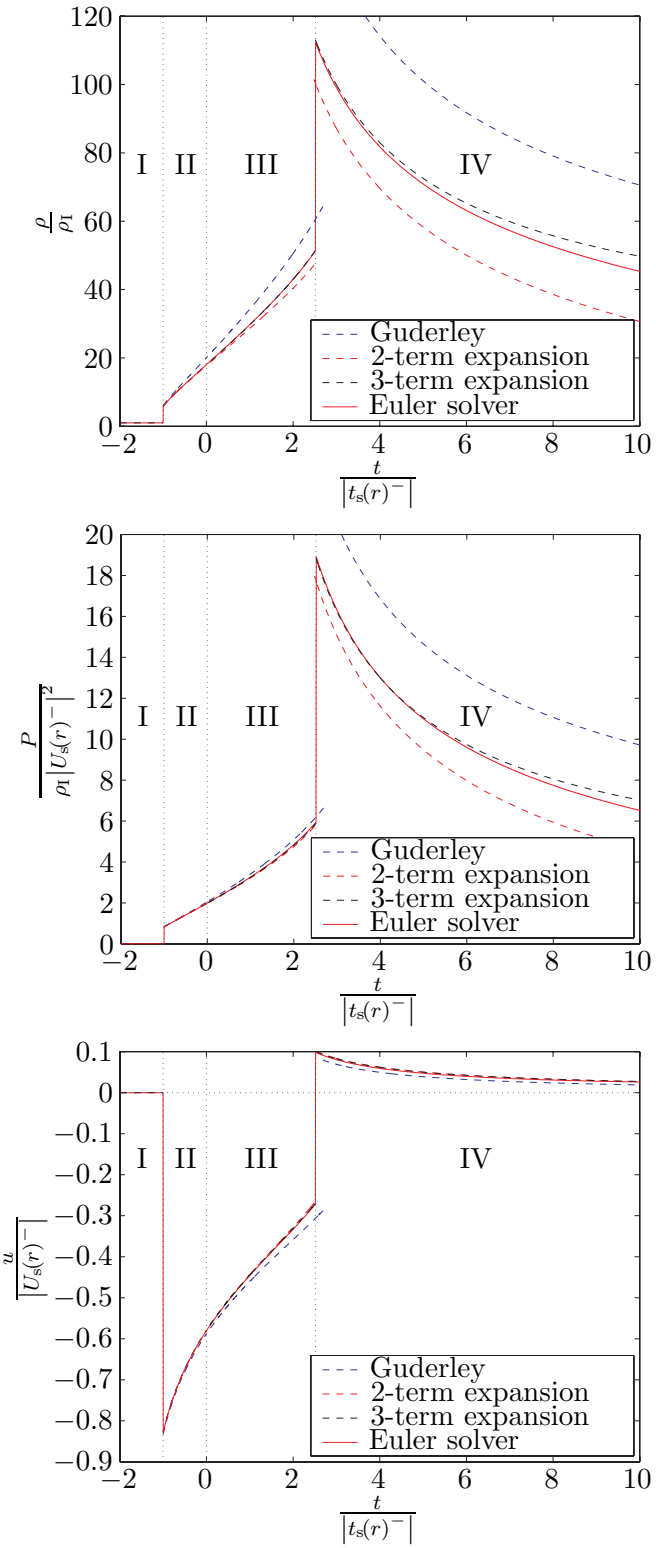

Figure 4.6: Normalized density, pressure, and velocity distributions versus normalized time for a spherical imploding shock ($\gamma = 1.4$). The calculations were started with a shock Mach number of 5 and the measurements were taken at a radius 10 times smaller than the initial radius (where the incoming shock Mach number is $M_s = 12.4$).

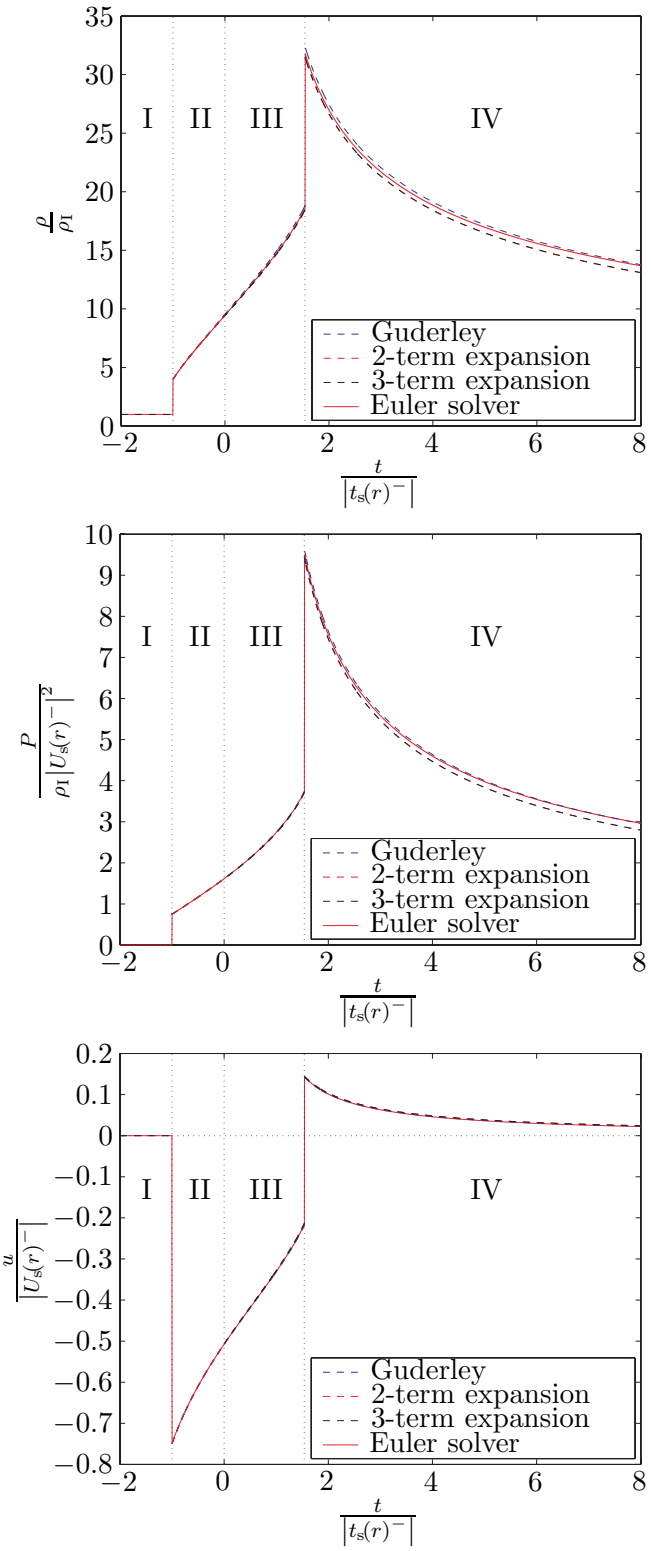

Figure 4.7: Normalized density, pressure, and velocity distributions versus normalized time for a spherical imploding shock ($\gamma = \frac{5}{3}$). The calculations were started with a shock Mach number of 10 and the measurements were taken at a radius 10 times smaller than the initial radius (where the incoming shock Mach number is $M_s = 28.7$).

axisymmetric and spherical cases, respectively.

The function G is defined as

$$\frac{R_\mathrm{s}}{c_\mathrm{I}\tau} = G\left(\nu, \gamma, \frac{t}{\tau}\right), \tag{4.1}$$

where τ depends on the considered shock trajectory. This function can be used to construct the R_s–t diagram. Figures 4.8, 4.11, 4.14, and 4.17 compare the different solutions. Note that in the reflected shock case, we do not have a weak shock series expansion and the characteristics program only computes the incoming shock solution.

The function F is given by

$$\frac{R_\mathrm{s}}{c_\mathrm{I}\tau} = F\left(\nu, \gamma, \frac{U_\mathrm{s}}{c_\mathrm{I}}\right). \tag{4.2}$$

This function links the shock position to its speed and is represented in Figures 4.9, 4.12, 4.15, and 4.18.

Finally, the function K is defined as

$$\theta = \frac{c_\mathrm{I} t}{R_\mathrm{s}} = K\left(\nu, \gamma, \frac{U_\mathrm{s}}{c_\mathrm{I}}\right), \tag{4.3}$$

and is the only function that does not involve the constant τ and is presented in Figures 4.10, 4.13, 4.16, and 4.19.

In all of the figures, the weak shock series expansion shows very good agreement with the characteristics computation for large radii (or for Mach numbers close to 1). The Guderley solution is clearly very good for very strong shocks. The addition of a second and then a third term to the Guderley solution clearly has a positive effect and even though it may not look like it on every single plot, the three term series expansion is always more accurate than the two term series expansion provided that the radius is sufficiently small (or equivalently, that the Mach number is sufficiently large).

Several discrepancies can be identified in the Euler computations. First, due to simplified initial conditions, the Euler curve is sometimes off from the characteristics computation results. In the reflected case, far from the reflection, the solution is also probably off from the exact solution because of the use of a non-infinite domain. Finally, in the spherical

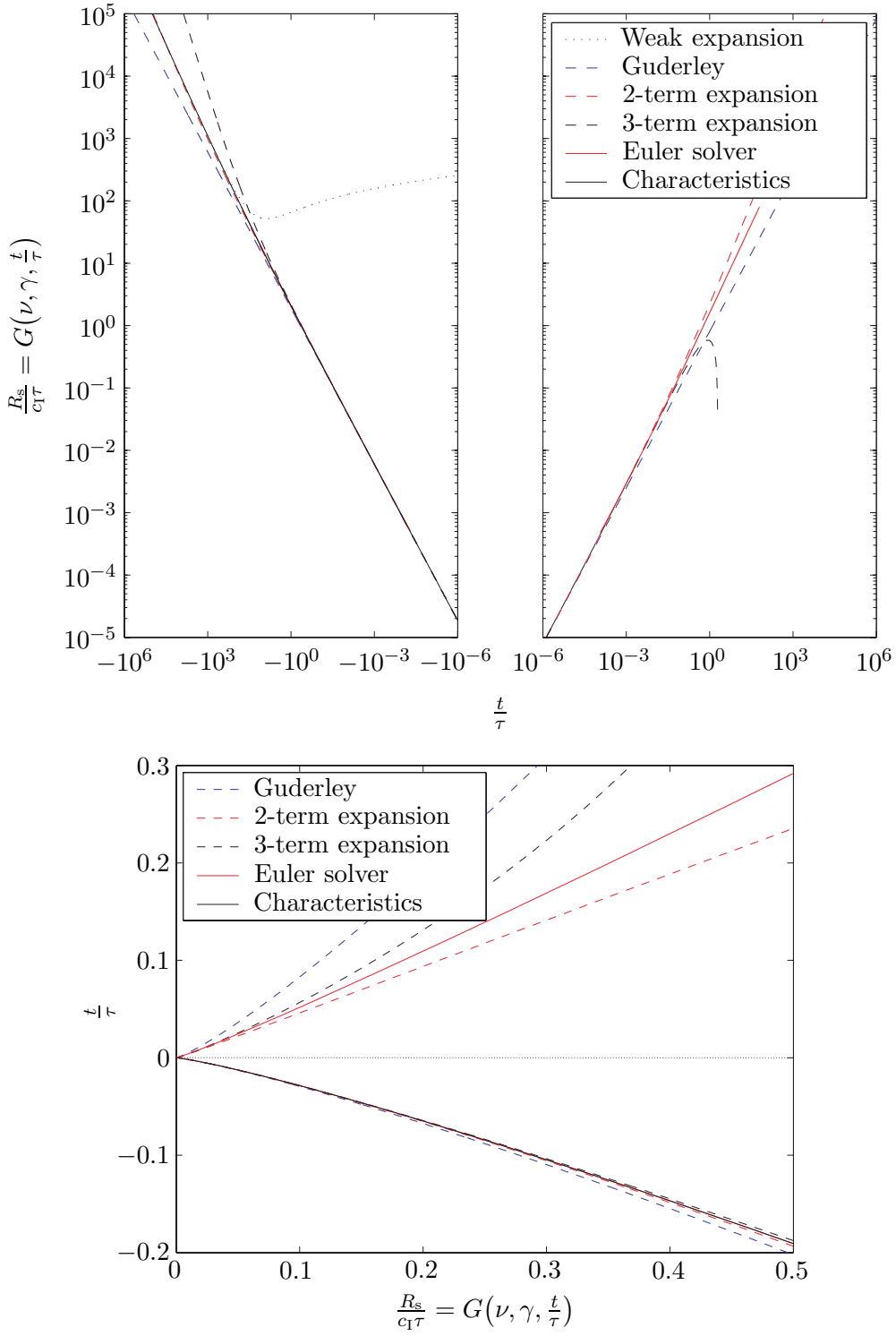

Figure 4.8: Function $\frac{R_s}{c_1\tau} = G(\nu, \gamma, \frac{t}{\tau})$ in the axisymmetric case for $\gamma = 1.4$. Note that in the incoming shock case, the Euler computation is also plotted but it is exactly superimposed onto the characteristics curve.

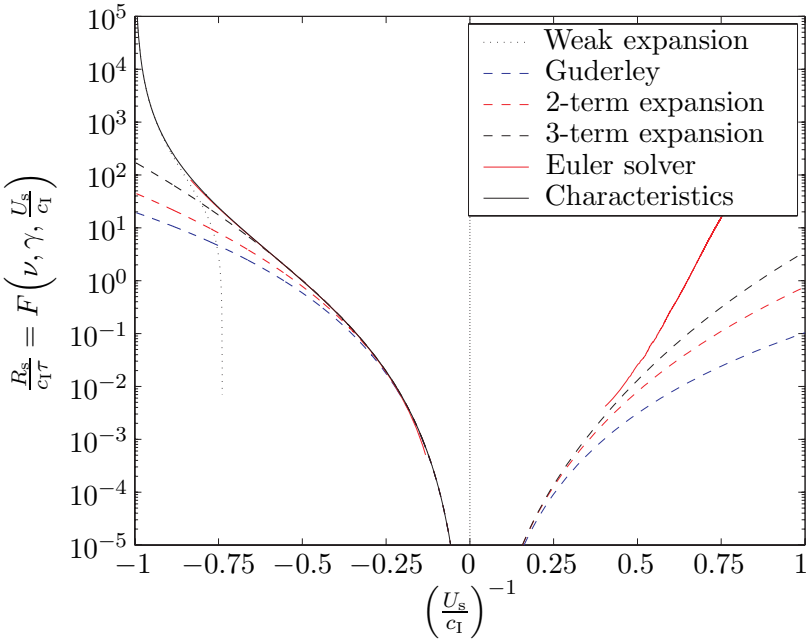

Figure 4.9: Function $\frac{R_s}{c_I \tau} = F\left(\nu, \gamma, \frac{U_s}{c_I}\right)$ in the axisymmetric case for $\gamma = 1.4$. Note that the Euler solver is slightly off in the beginning of the computation due to wrong initial conditions, and close to the origin where the gradients become very high and where the discretization errors become important.

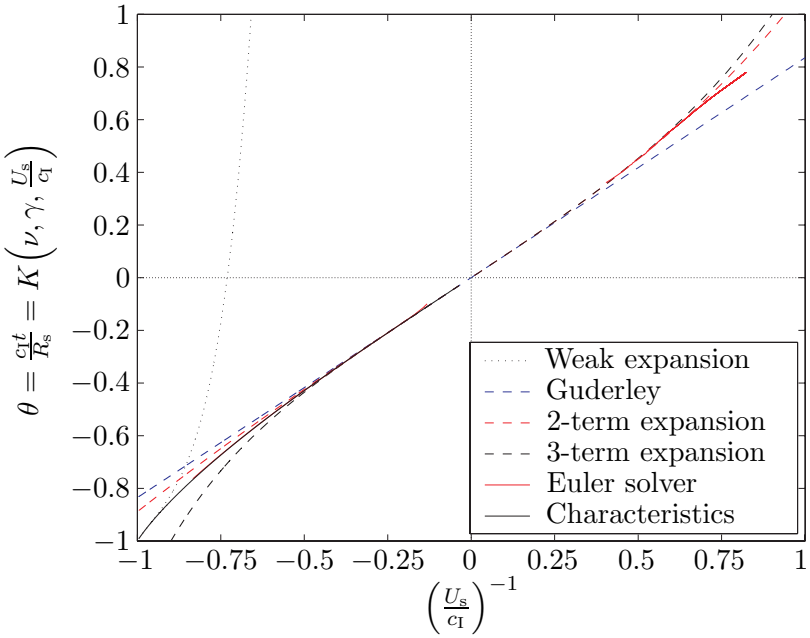

Figure 4.10: Function $\theta = K\left(\nu, \gamma, \frac{U_s}{c_I}\right)$ in the axisymmetric case for $\gamma = 1.4$. Note that the Euler solver is slightly off in the region close to the origin where the gradients become very high and where the discretization errors become important.

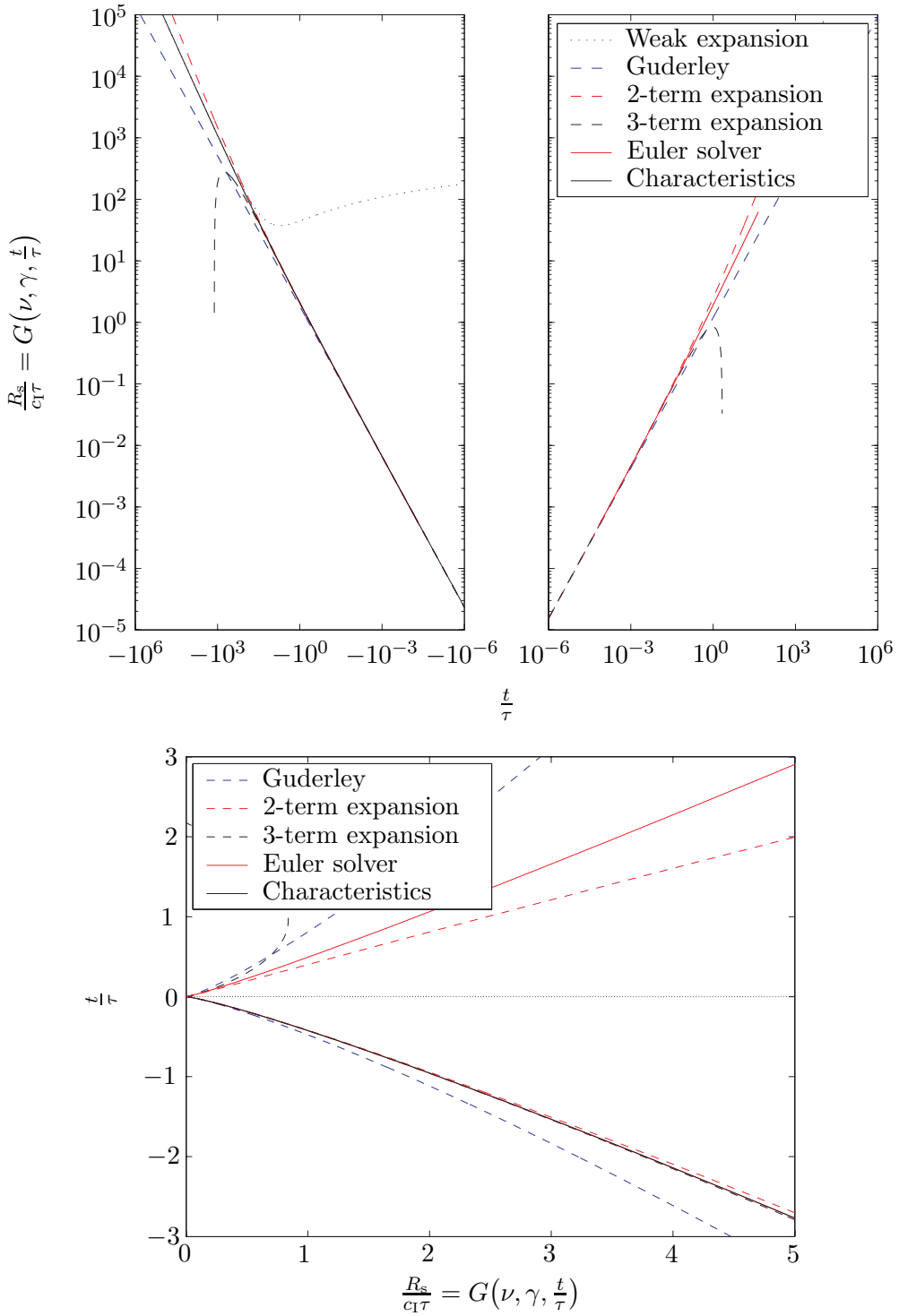

Figure 4.11: Function $\frac{R_s}{c_1\tau} = G(\nu, \gamma, \frac{t}{\tau})$ in the axisymmetric case for $\gamma = \frac{5}{3}$. Note that in the incoming shock case, the Euler computation is also plotted but it is exactly superimposed onto the characteristics curve.

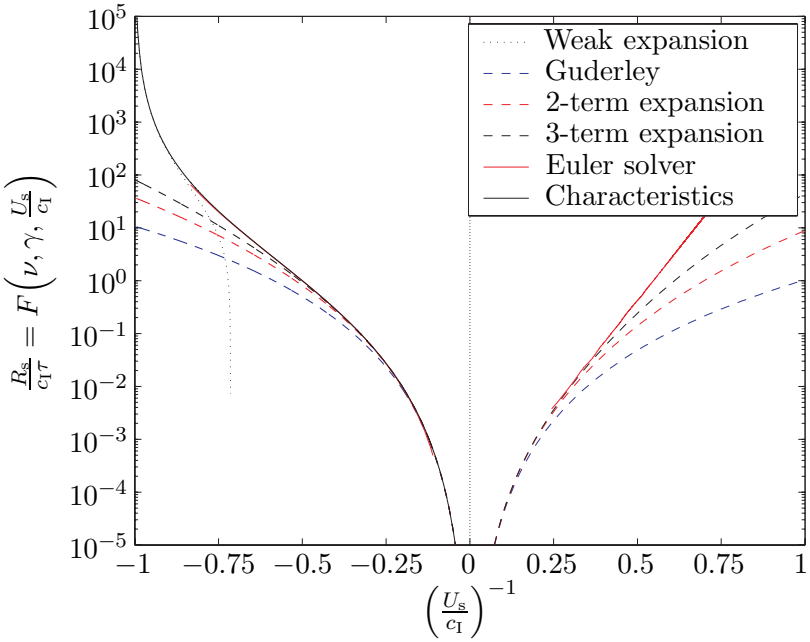

Figure 4.12: Function $\frac{R_s}{c_I \tau} = F\left(\nu, \gamma, \frac{U_s}{c_I}\right)$ in the axisymmetric case for $\gamma = \frac{5}{3}$. Note that the Euler solver is slightly off in the beginning of the computation due to wrong initial conditions, and close to the origin where the gradients become very high and where the discretization errors become important.

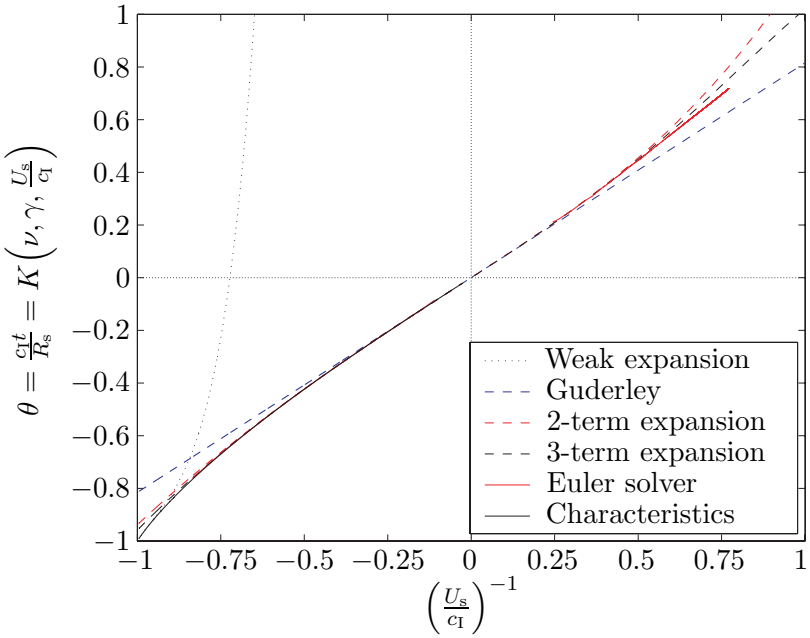

Figure 4.13: Function $\theta = K\left(\nu, \gamma, \frac{U_s}{c_I}\right)$ in the axisymmetric case for $\gamma = \frac{5}{3}$. Note that the Euler solver is slightly off in the region close to the origin where the gradients become very high and where the discretization errors become important.

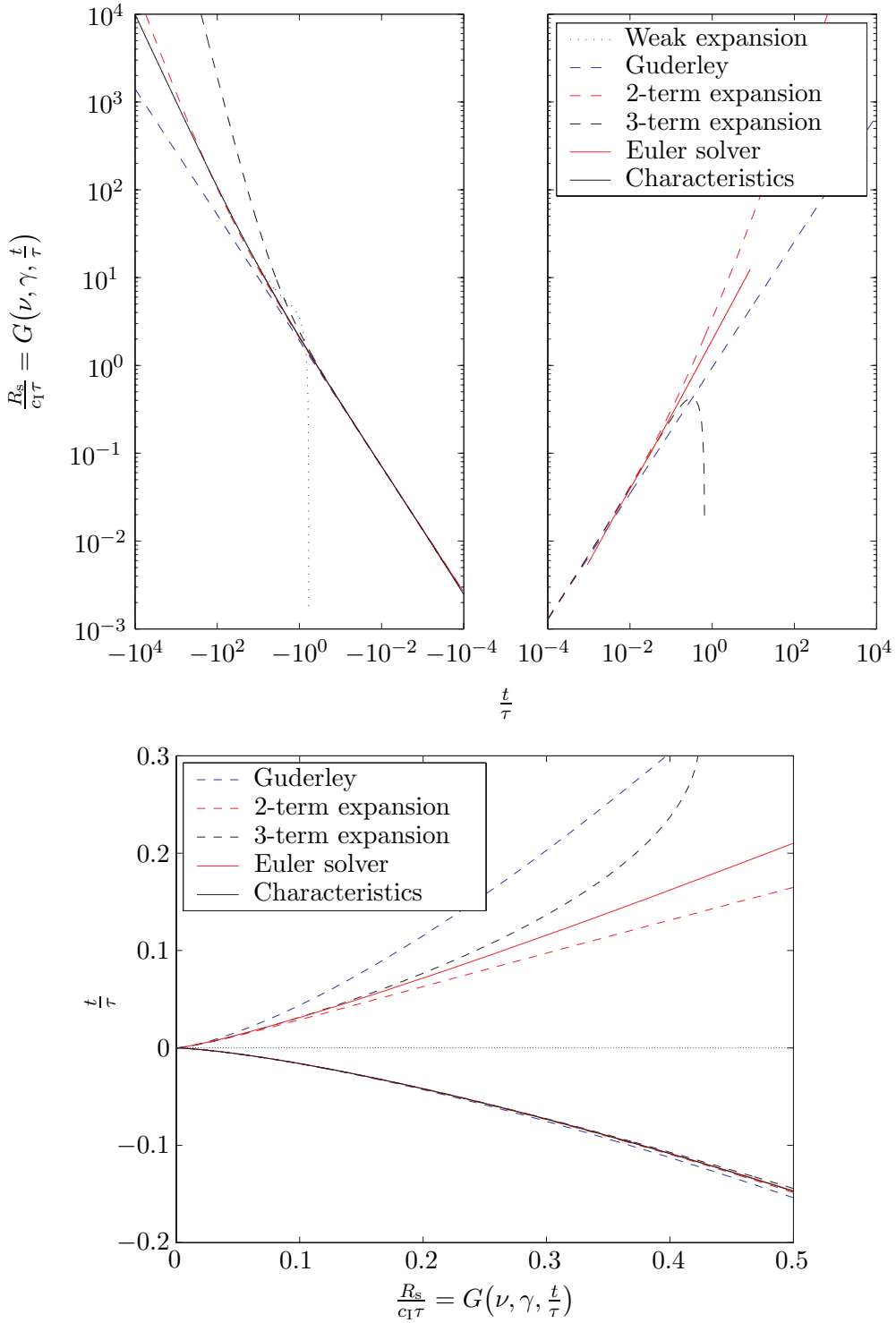

Figure 4.14: Function $\frac{R_s}{c_1\tau} = G\left(\nu, \gamma, \frac{t}{\tau}\right)$ in the spherical case for $\gamma = 1.4$. Note that in the incoming shock case, the Euler computation is also plotted but it is exactly superimposed onto the characteristics curve. The discrepancy for small radii in the reflected shock comes from the solid sphere in the computational domain.

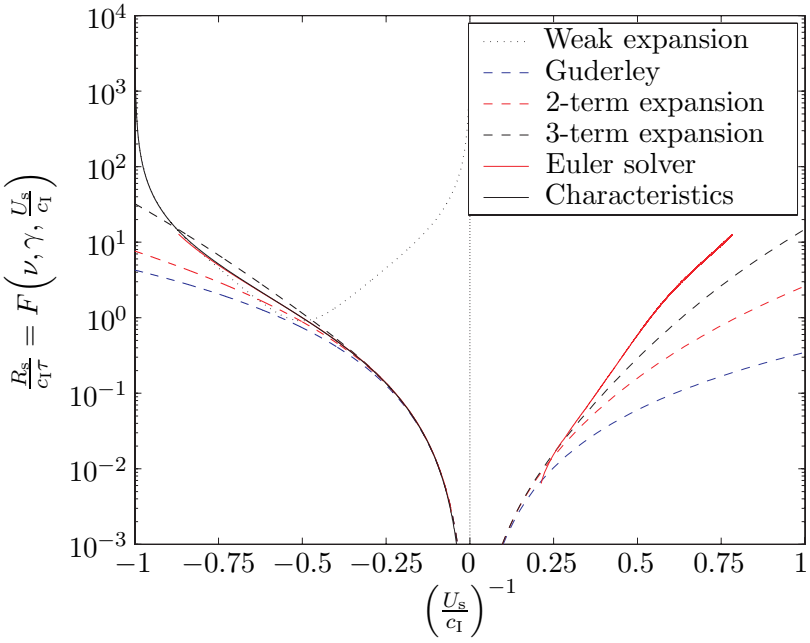

Figure 4.15: Function $\frac{R_s}{c_I \tau} = F\left(\nu, \gamma, \frac{U_s}{c_I}\right)$ in the spherical case for $\gamma = 1.4$. Note that the Euler solver is slightly off in the beginning of the computation due to wrong initial conditions. The discrepancy for small radii in the reflected shock comes from the solid sphere in the computational domain.

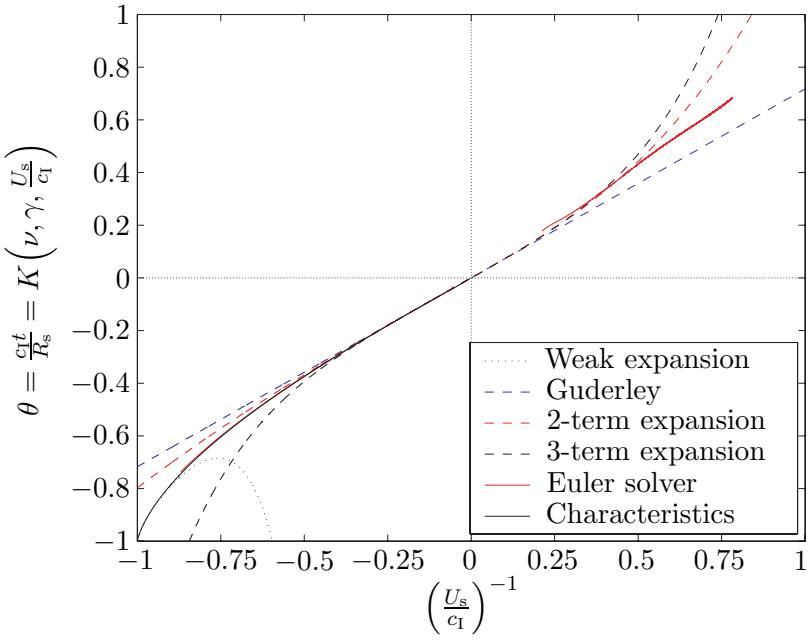

Figure 4.16: Function $\theta = K\left(\nu, \gamma, \frac{U_s}{c_I}\right)$ in the spherical case for $\gamma = 1.4$. The discrepancy for small radii in the reflected shock comes from the solid sphere in the computational domain.

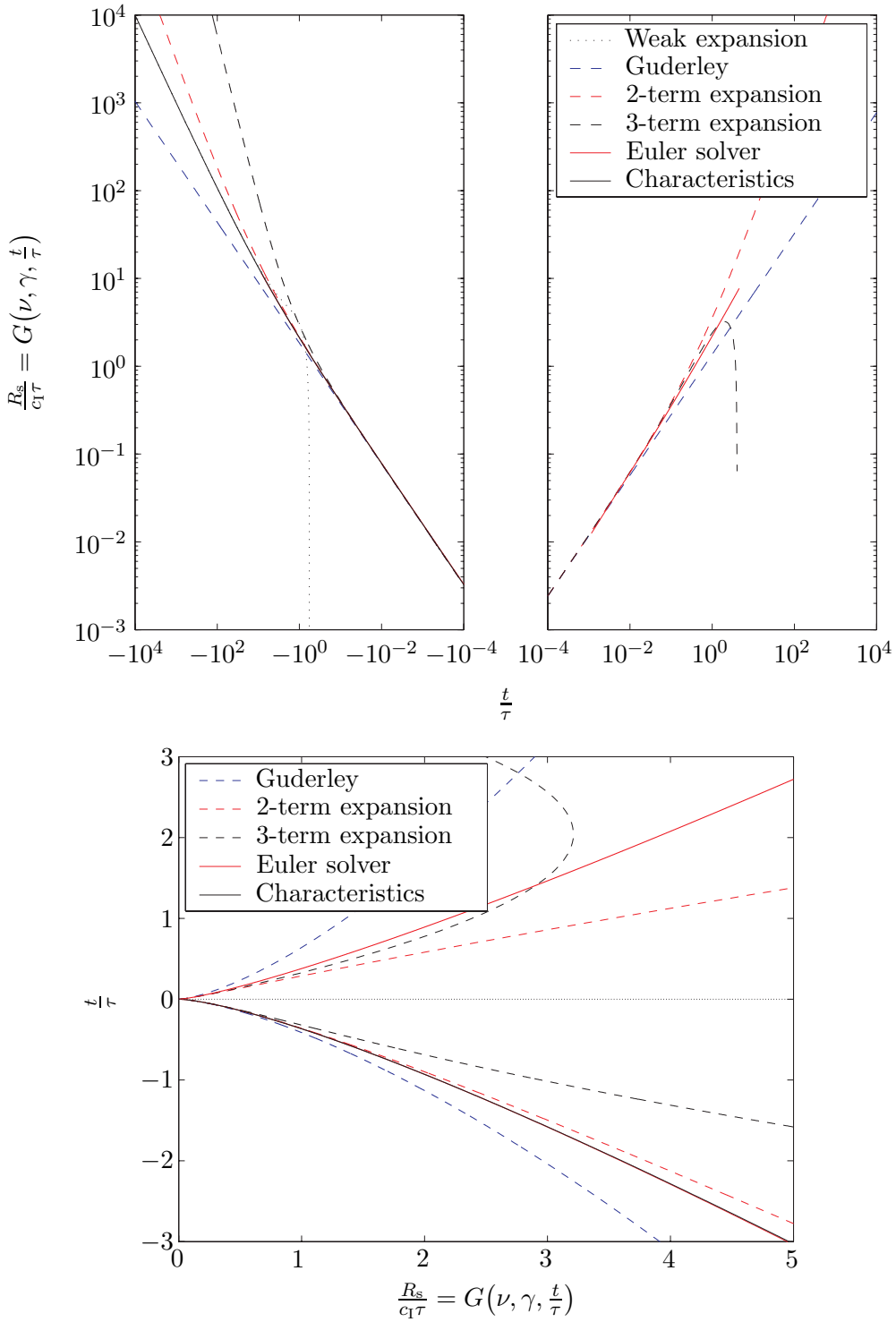

Figure 4.17: Function $\frac{R_s}{c_1\tau} = G(\nu, \gamma, \frac{t}{\tau})$ in the spherical case for $\gamma = \frac{5}{3}$. Note that in the incoming shock case, the Euler computation is also plotted but it is exactly superimposed onto the characteristics curve. The small discrepancy for small radii in the reflected shock comes from the solid sphere in the computational domain.

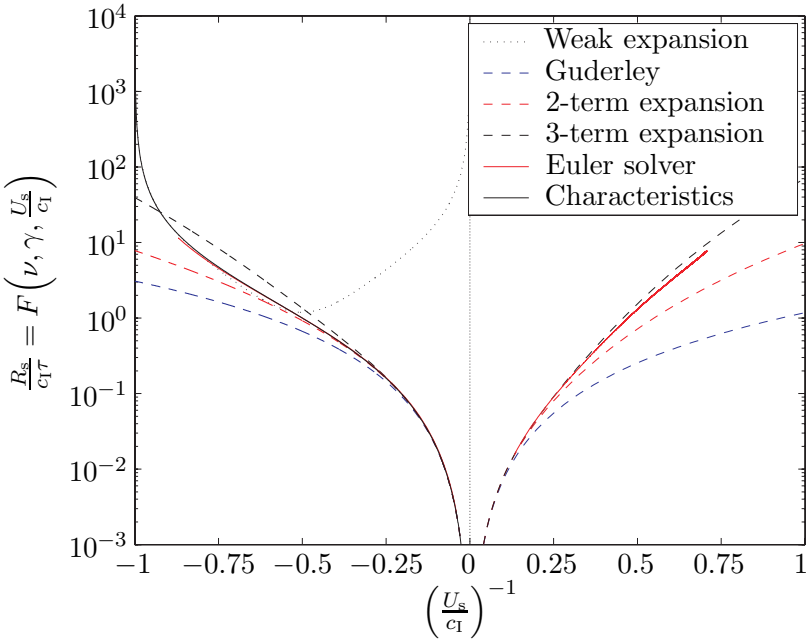

Figure 4.18: Function $\frac{R_s}{c_I\tau} = F\left(\nu, \gamma, \frac{U_s}{c_I}\right)$ in the spherical case for $\gamma = \frac{5}{3}$. Note that the Euler solver is slightly off in the beginning of the computation due to wrong initial conditions. The small discrepancy for small radii in the reflected shock comes from the solid sphere in the computational domain.

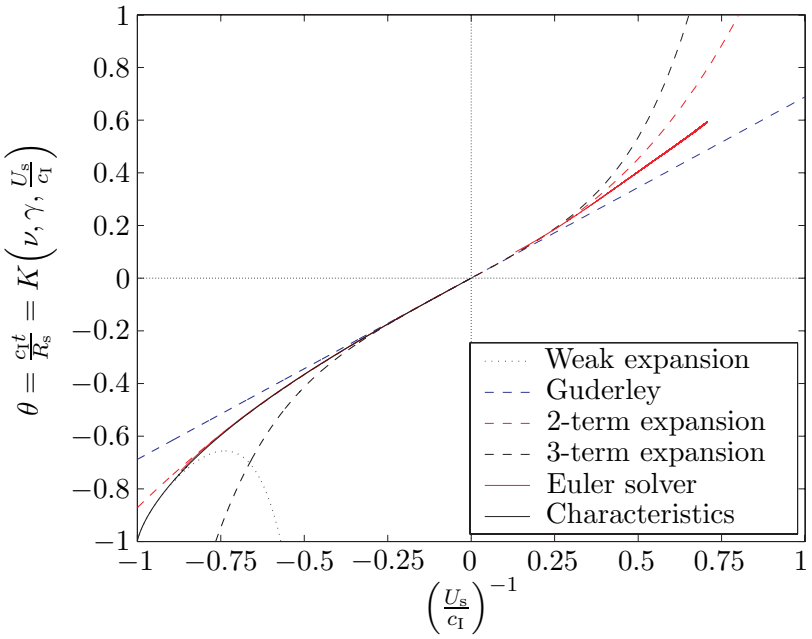

Figure 4.19: Function $\theta = K\left(\nu, \gamma, \frac{U_s}{c_I}\right)$ in the spherical case for $\gamma = \frac{5}{3}$. The small discrepancy for small radii in the reflected shock comes from the solid sphere in the computational domain.

symmetry case, the discrepancies occurring close to the reflection point are due to the solid sphere in the center. That sphere was introduced to avoid the singularities in the variables and in their derivatives.

Conclusions and Future Work

In this work, the imploding-reflecting shock problem was investigated with cylindrical and spherical symmetry. The shock was supposed to come from infinity, to travel through an initially uniform perfect gas at rest, to reflect at the origin, and to travel back towards infinity. Guderley's strong shock solution was expanded using a three term power series to represent the behavior of the shock close to the reflection point. Another series expansion was constructed to represent the behavior of the incoming shock when it is still very far from the origin. Finally, the characteristics method was used to solve the problem where these expansion series are not correct. To be able to go from very large to very small radii, an appropriate change of variables was performed.

Several comparisons between the series expansions, the characteristic results, and some Euler computations were presented. The results show that the weak shock expansion series is very accurate for large radii. In addition, each additional term of the strong shock series expansion seems to more accurately represent the actual solution around the origin.

The next step to complete this work would be to use the characteristics method to compute the reflected shock motion. This problem is more complicated since both regions around the shock have to be calculated (regions III and IV). In addition, the initial conditions are not based on the strong shock series expansion since this series is only valid for small r. If the same type of change of variables as the one used in the incoming characteristics program is used for the reflecting part, the following procedure could be used to obtain an initial condition. First, the incoming shock case should be evaluated up to a moment before the reflection time. Then, the obtained solution at that time has to be transformed back into r–t variables and usual characteristics have to be used to find the evolution of the flow in region II, to cross the boundary between regions II and III, and to

continue the calculation up to a finite positive, but small time. Then, the obtained results are transformed back into the coordinates used in the characteristics program to form the initial conditions in region III where the radius is sufficiently large that the strong shock series expansion is not accurate anymore.

Appendix A

Fourth-Order Integration Scheme

Assume a differential equation of the form

$$\frac{dy(x)}{dx} = F(x, y(x))\,. \tag{A.1}$$

Starting at $(x_0,\ y_0) = (x^*,\ y^*)$, the solution is integrated with a fourth-order accuracy Adam-Bashforth scheme. This scheme was chosen because it doesn't need any predictor-corrector steps for most of the discretized points:

$$y_k = y_{k-1} + \frac{\Delta x}{24}\Big[-9F(x_{k-4}, y_{k-4}) + 37F(x_{k-3}, y_{k-3}) - 59F(x_{k-2}, y_{k-2}) + 55F(x_{k-1}, y_{k-1})\Big], \tag{A.2}$$

with

$$x_k = x^* + k\Delta x, \tag{A.3}$$

$$y_k = y(x^* + k\Delta x)\,, \tag{A.4}$$

and where Δx is the increment step. This scheme can only be used for $k \geq 4$. To be able to start the integration, some predictor-corrector steps have to be performed on the first few

points to obtain fourth order accurate values. These predictor-corrector steps are

$$y_0 = y^*, \tag{A.5}$$

$$k_1''' = y_0 + \Delta x\, F(x_0, y_0)\,, \tag{A.6}$$

$$k_1'' = y_0 + \frac{\Delta x}{2}\left[F(x_0, y_0) + F\big(x_1, k_1'''\big)\right], \tag{A.7}$$

$$k_2'' = k_1'' + \frac{\Delta x}{2}\left[-F(x_0, y_0) + 3F\big(x_1, k_1'''\big)\right], \tag{A.8}$$

$$k_1' = y_0 + \frac{\Delta x}{12}\left[5F(x_0, y_0) + 8F\big(x_1, k_1''\big) - F_2\big(x_1, k_2''\big)\right], \tag{A.9}$$

$$k_2' = k_1' + \frac{\Delta x}{12}\left[-F(x_0, y_0) + 8F\big(x_1, k_1''\big) + 5\big(x_2, k_2''\big)\right], \tag{A.10}$$

$$k_3' = k_2' + \frac{\Delta x}{12}\left[5F(x_0, y_0) - 16F\big(x_1, k_1''\big) + 23F\big(x_2, k_2''\big)\right], \tag{A.11}$$

$$y_1 = y_0 + \frac{\Delta x}{24}\left[9F(x_0, y_0) + 19F\big(x_1, k_1'\big) - 5F\big(x_2, k_2'\big) + F\big(x_3, k_3'\big)\right], \tag{A.12}$$

$$y_2 = y_1 + \frac{\Delta x}{24}\left[-F(x_0, y_0) + 13F\big(x_1, k_1'\big) + 13F\big(x_2, k_2'\big) - F\big(x_3, k_3'\big)\right], \tag{A.13}$$

$$y_3 = y_2 + \frac{\Delta x}{24}\left[F(x_0, y_0) - 5F\big(x_1, k_1'\big) + 19F\big(x_2, k_2'\big) + 9F\big(x_3, k_3'\big)\right]. \tag{A.14}$$

Appendix B

Second Term System of Equations

After all the changes of variables that were made in Section 2.3.2, the equations can be written as

$$\frac{d\sigma_2(\phi_1)}{d\phi_1} = -\left[\frac{1}{1-\phi_1} + \frac{s_1'(\phi_1)}{s_1(\phi_1)} + \frac{2\,(1-n)}{n}\frac{\eta'(\phi_1)}{\eta(\phi_1)}\right]\left[\sigma_2(\phi_1) + \phi_1\overline{a}_2^{\pm}\right] - \overline{a}_2^{\pm}, \tag{B.1}$$

$$\frac{d\xi_2(\phi_1)}{d\phi_1} = \left[\nu\frac{\eta'(\phi_1)}{\eta(\phi_1)} - \frac{\rho_1'(\phi_1)}{\rho_1(\phi_1)}\right]\xi_2(\phi_1) - \frac{1}{n\,(1-\phi_1)}\frac{\eta'(\phi_1)}{\eta(\phi_1)}\omega_2(\phi_1) - \frac{\rho_1'(\phi_1)}{\rho_1(\phi_1)}\overline{a}_2^{\pm}, \tag{B.2}$$

$$\begin{aligned}\frac{d\omega_2(\phi_1)}{d\phi_1} = {} & \frac{[2\,(1-n)+n\nu]\left[\left[1-\nu-3\phi_1-\frac{1-n}{n(1-\phi_1)}\right]\frac{\eta'(\phi_1)}{\eta(\phi_1)}+3\right] - n\gamma\nu\pi_1(\phi_1)\,\frac{\rho_1'(\phi_1)}{\rho_1(\phi_1)}}{\gamma\pi_1(\phi_1)-1+\phi_1}\,\xi_2(\phi_1) + \\ & \frac{\left[\frac{3}{n}-4+\nu+(2+\gamma)\,\phi_1+\gamma\left[\frac{1-n}{n}-\nu\pi_1(\phi_1)\right]\frac{\phi_1}{1-\phi_1}\right]\frac{\eta'(\phi_1)}{\eta(\phi_1)}-\gamma-1}{\gamma\pi_1(\phi_1)-1+\phi_1}\,\omega_2(\phi_1) - \\ & \frac{2\gamma\,(1-n)\,\pi_1(\phi_1)\,\frac{\rho_1'(\phi_1)}{\rho_1(\phi_1)}}{\gamma\pi_1(\phi_1)-1+\phi_1}\,\sigma_2(\phi_1) + \\ & [2\,(1-n)+n\nu]\,\frac{2+\pi_1(\phi_1)\,\frac{s_1'(\phi_1)}{s_1(\phi_1)}-\left(\frac{1}{n}+\nu\right)\phi_1\frac{\eta'(\phi_1)}{\eta(\phi_1)}}{\gamma\pi_1(\phi_1)-1+\phi_1}\,\overline{a}_2^{\pm},\end{aligned} \tag{B.3}$$

with

$$s_1(\phi_1) = \frac{P_1(\phi_1)}{\rho_1(\phi_1)^{\gamma}}, \tag{B.4}$$

and where $\rho_1(\phi_1)$ and $s_1(\phi_1)$ were introduced to simplify the equations. Note that we can also write the following equations if needed:

$$\frac{s_1'(\phi_1)}{s_1(\phi_1)} = \frac{2\,(1-n)}{n}\frac{\phi_1}{1-\phi_1}\frac{\eta'(\phi_1)}{\eta(\phi_1)}, \tag{B.5}$$

$$\frac{\rho_1'(\phi_1)}{\rho_1(\phi_1)} = \frac{1}{1-\phi_1}\left[1-\nu\phi_1\frac{\eta'(\phi_1)}{\eta(\phi_1)}\right]. \tag{B.6}$$

Written in this form, it is very easy to find a first integral for Equation B.1:

$$\sigma_2(\phi_1) = D\frac{1-\phi_1}{s_1(\phi_1)\,\eta(\phi_1)^{\frac{2(1-n)}{n}}} - \phi_1\overline{a}_2^{\pm} = C\frac{\rho_1(\phi_1)^{\gamma-1}\,\eta(\phi_1)^2}{\pi_1(\phi_1)} - \phi_1\overline{a}_2^{\pm}, \tag{B.7}$$

where C and D are constants. In addition to the differential equations, we can write conditions on the boundaries of the regions. First, in region II, we get the following shock jump conditions at $\phi_1 = \phi_{1,\mathrm{II}}^{\mathrm{s}} = \frac{2}{\gamma+1}$,

$$\sigma_{2,\mathrm{II}}^{\mathrm{s}} = \left(\frac{3\gamma-1}{4} + \overline{a}_2^{-}\frac{\gamma-1}{\gamma+1}\right)\left(2+\frac{n\nu}{1-n}\right) - \frac{2\overline{a}_2^{-}}{\gamma+1}, \tag{B.8}$$

$$\xi_{2,\mathrm{II}}^{\mathrm{s}} = -\frac{2\overline{a}_2^{-}}{\gamma+1}, \tag{B.9}$$

$$\omega_{2,\mathrm{II}}^{\mathrm{s}} = -\frac{2\gamma\left(2\left(1-n\right)+n\nu\right)}{\gamma+1}, \tag{B.10}$$

where the superscript s means that the value is taken at the shock location. Once again, the variables ρ, P, and u have to be continuous when going from region II to region III (at $\eta = 0$), which means that $\rho_{2,\mathrm{II}}$, $P_{2,\mathrm{II}}$, and $u_{2,\mathrm{II}}$ are also continuous. Between regions III and IV, we have the following shock jump conditions:

$$\begin{aligned}\sigma_{2,\mathrm{IV}}^{\mathrm{s}} = \sigma_{2,\mathrm{III}}^{\mathrm{s}}\pi_{1,\mathrm{III}}^{\mathrm{s}}&\left[\frac{1+\gamma}{\pi_{1,\mathrm{III}}^{\mathrm{s}}\left(\gamma-1\right)-2\left(1-\phi_{1,\mathrm{III}}^{\mathrm{s}}\right)}+\frac{2\gamma}{1-\phi_{1,\mathrm{III}}^{\mathrm{s}}}\right]- \\ &\left[\frac{2\xi_{2,\mathrm{III}}^{\mathrm{s}}-\frac{\omega_{2,\mathrm{III}}^{\mathrm{s}}(\gamma+1)}{1-n}+2\left(\overline{a}_2^{+}+\xi_{2,\mathrm{III}}^{\mathrm{s}}\right)\left(2+\frac{n\nu}{1-n}\right)}{\pi_{1,\mathrm{III}}^{\mathrm{s}}\left(\gamma-1\right)-2\left(1-\phi_{1,\mathrm{III}}^{\mathrm{s}}\right)}\right]\times \\ &\left(\frac{\gamma-1}{\gamma+1}\right)\frac{\left(1-\phi_{1,\mathrm{III}}^{\mathrm{s}}-\gamma\pi_{1,\mathrm{III}}^{\mathrm{s}}\right)^2}{1-\phi_{1,\mathrm{III}}^{\mathrm{s}}}-\left(\frac{2\overline{a}_2^{+}}{\gamma+1}\right)\left(\frac{1-\phi_{1,\mathrm{III}}^{\mathrm{s}}-\gamma\pi_{1,\mathrm{III}}^{\mathrm{s}}}{1-\phi_{1,\mathrm{III}}^{\mathrm{s}}}\right),\end{aligned} \tag{B.11}$$

$$\xi_{2,\mathrm{IV}}^{\mathrm{s}} = \frac{\gamma\xi_{2,\mathrm{III}}^{\mathrm{s}}\left(1-\phi_{1,\mathrm{III}}^{\mathrm{s}}+\pi_{1,\mathrm{III}}^{\mathrm{s}}\right)-\left(2\overline{a}_2^{+}+\xi_{2,\mathrm{III}}^{\mathrm{s}}\right)\left(1-\phi_{1,\mathrm{III}}^{\mathrm{s}}-\gamma\pi_{1,\mathrm{III}}^{\mathrm{s}}\right)}{\left(\gamma+1\right)\left(1-\phi_{1,\mathrm{III}}^{\mathrm{s}}\right)}, \tag{B.12}$$

$$\begin{aligned}\omega_{2,\mathrm{IV}}^{\mathrm{s}} = \frac{4\gamma\left(1-n\right)\pi_{1,\mathrm{III}}^{\mathrm{s}}}{\left(\gamma+1\right)\left(1-\phi_{1,\mathrm{III}}^{\mathrm{s}}\right)}&\left[\xi_{2,\mathrm{III}}^{\mathrm{s}}-\sigma_{2,\mathrm{III}}^{\mathrm{s}}+\left(2+\frac{n\nu}{1-n}\right)\left(\overline{a}_2^{+}+\xi_{2,\mathrm{III}}^{\mathrm{s}}\right)\right]+ \\ &\frac{\omega_{2,\mathrm{III}}^{\mathrm{s}}}{\gamma+1}\left(\gamma-1-2\gamma^2\frac{\pi_{1,\mathrm{III}}^{\mathrm{s}}}{1-\phi_{1,\mathrm{III}}^{\mathrm{s}}}\right),\end{aligned} \tag{B.13}$$

where $\phi^{\mathrm{s}}_{1,\mathrm{III}}$ and $\phi^{\mathrm{s}}_{1,\mathrm{IV}}$ refer to the values of ϕ_1 in regions III and IV, respectively, at the reflected shock location. Finally, since there should be no velocity at $r = 0$, we impose the condition that $\xi_{2,\mathrm{IV}}$ and $\omega_{2,\mathrm{IV}}$ remain non-singular. The limiting behaviors of these functions as well as the exact formulation of this last condition will be given in Appendix C.

Appendix C

Limiting Behaviors of Strong Shock Expansion Variables

It is useful to examine the limiting behaviors of the functions we are integrating in the expansion problem. In fact, if a function tends to infinity or has an infinite slope at one of its boundaries, an adapted equation needs to be used so that the integration remains accurate.

C.1 First Term Limits

In the case of the first term of the expansions, the important limiting behaviors are

$$\lim_{\phi_1 \to 0} \pi_{1,\mathrm{II}} \propto \phi_1^2, \tag{C.1}$$

$$\lim_{\phi_1 \to 0} \log(\eta_{\mathrm{II}}) \propto \phi_1^n, \tag{C.2}$$

$$\lim_{\phi_1 \to 0} \pi_{1,\mathrm{III}} \propto \phi_1^2, \tag{C.3}$$

$$\lim_{\phi_1 \to 0} \log(\eta_{\mathrm{III}}) \propto (-\phi_1)^n, \tag{C.4}$$

$$\lim_{\phi_1 \to \frac{2(1-n)}{n\nu\gamma}} \pi_{1,\mathrm{IV}} \propto \frac{1}{\phi_1 - \frac{2(1-n)}{n\nu\gamma}}, \tag{C.5}$$

$$\lim_{\phi_1 \to \frac{2(1-n)}{n\nu\gamma}} \log(\eta_{\mathrm{IV}}) \propto \left[\phi_1 - \frac{2\,(1-n)}{n\nu\gamma}\right]^{-\frac{n\nu\gamma-2(1-n)}{2[n\nu\gamma+(\nu-2)(1-n)]}}, \tag{C.6}$$

$$\lim_{\phi_1 \to \frac{2(1-n)}{n\nu\gamma}} \log(P_{1,\mathrm{IV}}) \propto \left[\phi_1 - \frac{2\,(1-n)}{n\nu\gamma}\right]^{\frac{(1-n)[n\nu\gamma-2(1-n)]}{n[n\nu\gamma+(\nu-2)(1-n)]}}, \tag{C.7}$$

$$\lim_{\phi_1 \to \frac{2(1-n)}{n\nu\gamma}} \log(u_{1,\mathrm{IV}}) \propto \left[\phi_1 - \frac{2\,(1-n)}{n\nu\gamma}\right]^{\frac{n\nu\gamma-2(1-n)}{2n[n\nu\gamma+(\nu-2)(1-n)]}}, \tag{C.8}$$

$$\lim_{\phi_1 \to \frac{2(1-n)}{n\nu\gamma}} \log(\rho_{1,\mathrm{IV}}) \propto \left[\phi_1 - \frac{2\,(1-n)}{n\nu\gamma}\right]^{\frac{\nu(1-n)}{n\nu\gamma-2(1-n)+(1-n)}}. \tag{C.9}$$

For these limits, depending on the exponent, an appropriate equation might be needed. For example, if around $\phi_1 = C$, $f(\phi_1)$ behaves like $(\phi_1 - C)^i$, a particular equation is needed if $i < 1$ to avoid derivatives that tend to infinity. In that case, we pose

$$f(\phi_1) = \overline{f}(\phi_1)\,(\phi_1 - C)^i\,, \tag{C.10}$$

and we solve an adapted differential equation to find $\overline{f}(\phi_1)$:

$$\frac{d\overline{f}(\phi_1)}{d\phi_1} = \frac{1}{(\phi_1 - C)^i}\frac{df(\phi_1)}{d\phi_1} - \frac{i}{\phi_1 - C}\overline{f}(\phi_1)\,. \tag{C.11}$$

C.2 Second Term Limits

As ϕ_1 tends to 0 (or for t close to 0), the functions $\sigma_2(\phi_1)$, $\omega_2(\phi_1)$ and $\xi_2(\phi_1)$ are proportional to ϕ_1^{2n-2}. The limits in region IV for η tending to infinity are more complicated and have to be investigated very carefully. First, consider the first integral

$$\sigma_{2,\mathrm{IV}}(\phi_1) = -\phi_1 \overline{a}_2^{+} + C_{2,\mathrm{IV}}\frac{\rho_1(\phi_1)^{\gamma-1}\,\eta(\phi_1)^2}{\pi_1(\phi_1)}. \tag{C.12}$$

The limiting behavior of this integral is made up of two separate parts; the first can be expressed as a regular series, and the second by another series times a term that possesses

an infinite slope:

$$\begin{aligned}\sigma_{2,\mathrm{IV}}(\phi_1) &= \sigma^{\mathrm{a}}_{2,\mathrm{IV}}(\phi_1) + \sigma^{\mathrm{b}}_{2,\mathrm{IV}}(\phi_1) \\ &= \left[-\overline{a}_2^{+}\phi_1^{\mathrm{l}} - \overline{a}_2^{+}\left(\phi_1 - \phi_1^{\mathrm{l}}\right)\right] + \left(\phi_1 - \phi_1^{\mathrm{l}}\right)^{\frac{(1-n)\gamma\nu}{(\nu-2)(1-n)+n\gamma\nu}} \sum_{k=0}^{\infty} A_k \left(\phi_1 - \phi_1^{\mathrm{l}}\right)^k,\end{aligned} \tag{C.13}$$

where $\phi_1^{\mathrm{l}} = \frac{2(1-n)}{n\nu\gamma}$, which corresponds to the limit for η tending to infinity, and where

$$\sigma^{\mathrm{a}}_{2,\mathrm{IV}}(\phi_1) = -\overline{a}_2^{+}\phi_1^{\mathrm{l}} - \overline{a}_2^{+}\left(\phi_1 - \phi_1^{\mathrm{l}}\right) \tag{C.14}$$

$$\sigma^{\mathrm{b}}_{2,\mathrm{IV}}(\phi_1) = \left(\phi_1 - \phi_1^{\mathrm{l}}\right)^{\frac{(1-n)\gamma\nu}{(\nu-2)(1-n)+n\gamma\nu}} \sum_{k=0}^{\infty} A_k \left(\phi_1 - \phi_1^{\mathrm{l}}\right)^k. \tag{C.15}$$

In the following paragraphs, f^{a} and f^{b} refer to the first and the second parts of f. Equation C.13 leads us to expect a similar form for the other two variables ($\xi_{2,\mathrm{IV}}$ and $\omega_{2,\mathrm{IV}}$). To be able to integrate accurately these two variables using our integration scheme, we absolutely need to split the equations and solve each part individually since one of them has an infinite slope.

Consider the first part for now. This part is found using Equations B.2 and B.3, where $\sigma_2(\phi_1)$ is replaced by its second part ($-\phi_1\overline{a}_2^{+}$). In this case, the functions that are integrated are only the second parts of $\xi_{2,\mathrm{IV}}$ and $\omega_{2,\mathrm{IV}}$. When the resulting equations are taken at the limit when ϕ_1 tends to ϕ_1^{l}, we get

$$\frac{d\omega^{\mathrm{a}}_{2,\mathrm{IV}}(\phi_1)}{d\phi_1} = \frac{(1-n)\,\nu\left[\gamma\left[\omega^{\mathrm{a}}_{2,\mathrm{IV}}(\phi_1) - n\gamma\xi^{\mathrm{a}}_{2,\mathrm{IV}}(\phi_1)\right] - 2\overline{a}_2^{+}(1-n)\right]}{\left(\phi_1 - \phi_1^{\mathrm{l}}\right)\gamma\left[(\nu-2)(1-n) + n\gamma\nu\right]} + \mathrm{H.O.T.}, \tag{C.16}$$

$$\frac{d\xi^{\mathrm{a}}_{2,\mathrm{IV}}(\phi_1)}{d\phi_1} = \frac{\nu\left[\gamma\left[\omega^{\mathrm{a}}_{2,\mathrm{IV}}(\phi_1) - n\nu\xi^{\mathrm{a}}_{2,\mathrm{IV}}(\phi_1)\right] - 2\overline{a}_2^{+}(1-n)\right]}{2\left(\phi_1 - \phi_1^{\mathrm{l}}\right)\left[(\nu-2)(1-n) + n\gamma\nu\right]} + \mathrm{H.O.T.}. \tag{C.17}$$

This gives a leading order term that tends to infinity. However, according to our boundary conditions, the variables have to remain bounded everywhere. The only way that this is

possible is if we have

$$\omega^{\mathrm{a}}_{2,\mathrm{IV}}\left(\phi_1^{\mathrm{l}}\right) = n\nu\xi^{\mathrm{a}}_{2,\mathrm{IV}}\left(\phi_1^{\mathrm{l}}\right) + \frac{2\overline{a}_2^{+}\,(1-n)}{\gamma}. \tag{C.18}$$

This is a condition that always has to be satisfied, and it is imposed right away when integrating in region IV. Now, we can investigate what happens with the second part of the variables. This part can be written as

$$f^{\mathrm{b}}(\phi_1) = \left(\phi_1 - \phi_1^{\mathrm{l}}\right)^{\frac{(1-n)\gamma\nu}{(\nu-2)(1-n)+n\gamma\nu}} \overline{f^{\mathrm{b}}}(\phi_1)\,, \tag{C.19}$$

and the equations for $\overline{f^{\mathrm{b}}}$ can be written from Equations B.2 and B.3 by replacing $\overline{a}_2^{+}$ by 0 since it does not influence this part, and by taking only the first part of $\sigma_{2,\mathrm{IV}}$. Once again, looking at what happens close to $r = 0$ we obtain the following equations:

$$\frac{d\overline{\omega^{\mathrm{b}}}_{2,\mathrm{IV}}(\phi_1)}{d\phi_1} = \frac{-(1-n)\,\nu\left[2\,(1-n) + (\gamma-1)\,\overline{\omega^{\mathrm{b}}}_{2,\mathrm{IV}}(\phi_1) + n\nu\overline{\xi^{\mathrm{b}}}_{2,\mathrm{IV}}(\phi_1)\right]}{\left(\phi_1 - \phi_1^{\mathrm{l}}\right)\left[(\nu-2)\,(1-n) + n\gamma\nu\right]} + \text{H.O.T.}, \tag{C.20}$$

$$\frac{d\overline{\xi^{\mathrm{b}}}_{2,\mathrm{IV}}(\phi_1)}{d\phi_1} = \frac{\gamma\nu\left[\overline{\omega^{\mathrm{b}}}_{2,\mathrm{IV}}(\phi_1) - [2\,(1-n) + n\nu]\,\overline{\xi^{\mathrm{b}}}_{2,\mathrm{IV}}(\phi_1)\right]}{2\left(\phi_1 - \phi_1^{\mathrm{l}}\right)\left[(\nu-2)\,(1-n) + n\gamma\nu\right]} + \text{H.O.T.} \tag{C.21}$$

Once again, since we do not want any singular behaviors, this leads to the following conditions:

$$\overline{\omega^{\mathrm{b}}}_{2,\mathrm{IV}}\left(\phi_1^{\mathrm{l}}\right) = \frac{-2\,(1-n)\,[2\,(1-n) + n\nu]}{2\,(1-n)\,(\gamma-1) + n\gamma\nu}, \tag{C.22}$$

$$\overline{\xi^{\mathrm{b}}}_{2,\mathrm{IV}}\left(\phi_1^{\mathrm{l}}\right) = \frac{-2\,(1-n)}{2\,(1-n)\,(\gamma-1) + n\gamma\nu}. \tag{C.23}$$

We now have a method to integrate the functions in region IV. First, given a value for $\sigma_{2,\mathrm{IV}}$ at the shock, find the two parts of the first integral (Equation C.13). Given the value of $\xi^{\mathrm{a}}_{2,\mathrm{IV}}\left(\phi_1^{\mathrm{l}}\right)$, use Equation C.18 to find the initial condition for $\omega^{\mathrm{a}}_{2,\mathrm{IV}}$. Integrate the first parts of $\xi_{2,\mathrm{IV}}$ and $\omega_{2,\mathrm{IV}}$ up to the shock. Then, integrate the second parts using the initial conditions given in Equations C.22 and C.23. Finally, reconstruct the whole solution by

adding the two parts. Note that L'Hôpital's theorem is used to start the integration of the differential equations for each of the parts. Due to their length, these resulting limits are not presented.

C.3 Third Term Limits

The functions $\sigma_3(\phi_1)$, $\omega_3(\phi_1)$, and $\xi_3(\phi_1)$ are proportional to ϕ_1^{4n-4} in the region close to $\phi_1 = 0$ ($t = 0$). The difficulties are once again in region IV, where this time the solutions have to be divided into three parts. In fact, each function can be written as

$$\begin{aligned} f &= f^{\mathrm{a}} + f^{\mathrm{b}} + f^{\mathrm{c}} \\ &= \sum_{k=0}^{\infty} A_k \left(\phi_1 - \phi_1^{\mathrm{l}}\right)^k + \\ &\quad \left(\phi_1 - \phi_1^{\mathrm{l}}\right)^{\frac{(1-n)\gamma\nu}{(\nu-2)(1-n)+n\gamma\nu}} \sum_{k=0}^{\infty} B_k \left(\phi_1 - \phi_1^{\mathrm{l}}\right)^k + \\ &\quad \left(\phi_1 - \phi_1^{\mathrm{l}}\right)^{2\frac{(1-n)\gamma\nu}{(\nu-2)(1-n)+n\gamma\nu}} \sum_{k=0}^{\infty} C_k \left(\phi_1 - \phi_1^{\mathrm{l}}\right)^k, \end{aligned} \tag{C.24}$$

where f^{a}, f^{b}, and f^{c} refer to the first, the second, and the third parts of f. The equations are split such that the different parts are solved separately, as for the second term limit (see Section C.2). This time, the equations are much longer, but the principle is the same. For the first part equations, we keep all the first parts coming from the second term, as well as the terms in $\overline{a}_3^+$ and the first part of the integral of $\sigma_3(\phi_1)$. Writing this first system and taking the limit for ϕ_1 tending to ϕ_1^{l}, we get a condition relating $\xi_{3,\mathrm{IV}}^{\mathrm{a}}(\phi_1^{\mathrm{l}})$ and $\omega_{3,\mathrm{IV}}^{\mathrm{a}}(\phi_1^{\mathrm{l}})$. The second part is formed by removing the $\overline{a}_3^+$ terms, taking the second part of $\sigma_3(\phi_1)$ and the adequate corresponding functions from the second term. The limit of this new system leads to two initial conditions. The last part is also formed by removing the $\overline{a}_3^+$ terms, but taking the third part from $\sigma_3(\phi_1)$ and adequate functions from the second term. Once again, the limit gives two initial conditions for the two unknown functions. Overall, only one value can be chosen and the other initial conditions are fixed by this choice.

To illustrate how the second term affects the different parts, suppose that we have

$$\frac{df_{3,\mathrm{IV}}(\phi_1)}{d\phi_1} = A(\phi_1)\, f_{3,\mathrm{IV}}(\phi_1) + B(\phi_1)\, \overline{a}_3^{+} + C(\phi_1)\left(\overline{a}_2^{+}\right)^2 + D(\phi_1)\, \overline{a}_2^{+} f_{2,\mathrm{IV}}(\phi_1) + E(\phi_1)\left[f_{2,\mathrm{IV}}(\phi_1)\right]^2 . \quad \text{(C.25)}$$

According to the notation introduced earlier, we have

$$f_{2,\mathrm{IV}}(\phi_1) = f^{\mathrm{a}}_{2,\mathrm{IV}}(\phi_1) + f^{\mathrm{b}}_{2,\mathrm{IV}}(\phi_1)\,, \quad \text{(C.26)}$$

$$f_{3,\mathrm{IV}}(\phi_1) = f^{\mathrm{a}}_{3,\mathrm{IV}}(\phi_1) + f^{\mathrm{b}}_{3,\mathrm{IV}}(\phi_1) + f^{\mathrm{c}}_{3,\mathrm{IV}}(\phi_1)\,. \quad \text{(C.27)}$$

Once the differential equation is split into the three different parts, we get

$$\frac{df^{\mathrm{a}}_{3,\mathrm{IV}}(\phi_1)}{d\phi_1} = A(\phi_1)\, f^{\mathrm{a}}_{3,\mathrm{IV}}(\phi_1) + B(\phi_1)\, \overline{a}_3^{+} + C(\phi_1)\left(\overline{a}_2^{+}\right)^2 + D(\phi_1)\, \overline{a}_2^{+} f^{\mathrm{a}}_{2,\mathrm{IV}}(\phi_1) + E(\phi_1)\left[f^{\mathrm{a}}_{2,\mathrm{IV}}(\phi_1)\right]^2, \quad \text{(C.28)}$$

$$\frac{df^{\mathrm{b}}_{3,\mathrm{IV}}(\phi_1)}{d\phi_1} = A(\phi_1)\, f^{\mathrm{b}}_{3,\mathrm{IV}}(\phi_1) + D(\phi_1)\, \overline{a}_2^{+} f^{\mathrm{b}}_{2,\mathrm{IV}}(\phi_1) + 2E(\phi_1)\, f^{\mathrm{a}}_{2,\mathrm{IV}}(\phi_1)\, f^{\mathrm{b}}_{2,\mathrm{IV}}(\phi_1)\,, \quad \text{(C.29)}$$

$$\frac{df^{\mathrm{c}}_{3,\mathrm{IV}}(\phi_1)}{d\phi_1} = A(\phi_1)\, f^{\mathrm{c}}_{3,\mathrm{IV}}(\phi_1) + E(\phi_1)\left[f^{\mathrm{b}}_{2,\mathrm{IV}}(\phi_1)\right]^2 . \quad \text{(C.30)}$$

Note that once again, to avoid infinite slopes, the equations for the last two parts are transformed to remove any singular derivatives (see Equation C.11).

Appendix D

Series Expansion Expressions

To be able to compare the different results, it is useful to express each expansion expression in terms of different variables. All the results presented here can be obtained easily by using the equations presented in previous chapters. First, the functions F, G, and K defined in Section 1.2 will be presented for each of the expansions (Section D.1). Then, the density, the pressure, and the velocity of the flow in the strong shock expansion results, as well as the time, will be normalized to obtain expressions that do not become singular for small r (Section D.2).

D.1 Functions F, G, and K

The function F defines the shock position in terms of the normalized velocity of the shock. This function can be easily found by using Equations 1.19 and 1.18:

$$R_{\rm s} = R_{\rm s}^{\star}\frac{F\left(\nu,\gamma,\overline{U}_{\rm s}\right)}{F\left(\nu,\gamma,\overline{U}_{\rm s}^{\star}\right)} = c_{\rm I}\tau F\left(\nu,\gamma,\overline{U}_{\rm s}\right). \tag{D.1}$$

Using this last expression, we find that F takes the following strong and weak expansion forms,

$$F_{\rm St.} = \frac{\overline{\tau}_{\rm s}}{\tau}\left(\frac{n}{\alpha^{\pm}\overline{U}_{\rm s}}\right)^{\frac{n}{1-n}} \left[1+\frac{\overline{a}_2^{\pm}}{\gamma\left(1-n\right)}\frac{n}{\overline{U}_{\rm s}^2}+\frac{\left(\overline{a}_2^{\pm}\right)^2\left(\frac{3}{2}-n\right)+\overline{a}_3^{\pm}\left(1-n\right)}{\gamma^2\left(1-n\right)^2}\frac{n}{\overline{U}_{\rm s}^4}+\text{H.O.T.}\right], \tag{D.2}$$

$$F_{\text{W., cyl.}} = \frac{\overline{\tau}_{\text{w}}}{\tau}\frac{1}{4\left(1+\overline{U}_{\text{s}}\right)^2}\left[1+\frac{15-\gamma}{2\left(1+\gamma\right)}\left(1+\overline{U}_{\text{s}}\right)+\text{H.O.T.}\right], \tag{D.3}$$

$$F_{\text{W., sph.}} = -\frac{\overline{\tau}_{\text{w}}}{\tau}\frac{1}{1+\overline{U}_{\text{s}}}\left[1+\frac{4}{1+\gamma}\left(1+\overline{U}_{\text{s}}\right)+\left(1+\overline{U}_{\text{s}}\right)^2+\text{H.O.T.}\right], \tag{D.4}$$

where, in the strong shock case, the following normalized coefficients are used:

$$\overline{a}_2^{\pm} = \frac{a_2^{\pm} n\gamma\left(3-2n\right)}{\left(\alpha^{\pm}\right)^2}, \tag{D.5}$$

$$\overline{a}_3^{\pm} = \frac{n^2\gamma^2\left[2a_3^{\pm}n\left(5-4n\right)-\left(a_2^{\pm}\right)^2\left(1-n\right)\left(7-4n\right)\right]}{2\left(\alpha^{\pm}\right)^4}. \tag{D.6}$$

The function G expresses the shock radius in terms of the time ($R_{\text{s}} = c_{\text{I}}\tau G\left(\nu,\gamma,\frac{t}{\tau}\right)$). In the following expansions, $\overline{t} = \frac{t}{\tau}$:

$$G_{\text{St.}} = \left(\frac{\overline{\tau}_{\text{s}}}{\tau}\right)^{1-n}\left(\frac{\overline{t}}{\alpha^{\pm}}\right)^n\left[1+a_2^{\pm}\left(\frac{\overline{t}}{\alpha^{\pm}}\frac{\tau}{\overline{\tau}_{\text{s}}}\right)^{2(1-n)}+a_3^{\pm}\left(\frac{\overline{t}}{\alpha^{\pm}}\frac{\tau}{\overline{\tau}_{\text{s}}}\right)^{4(1-n)}+\text{H.O.T.}\right], \tag{D.7}$$

$$G_{\text{W., cyl.}} = -\overline{t}\left[1+\frac{1}{\sqrt{-\overline{t}\frac{\tau}{\overline{\tau}_{\text{w}}}}}-\frac{19+3\gamma}{16\left(1+\gamma\right)}\frac{\log\left(-\overline{t}\frac{\tau}{\overline{\tau}_{\text{w}}}\right)}{-\overline{t}\frac{\tau}{\overline{\tau}_{\text{w}}}}+\overline{a}_2\frac{1}{-\overline{t}\frac{\tau}{\overline{\tau}_{\text{w}}}}+\text{H.O.T.}\right], \tag{D.8}$$

$$G_{\text{W., sph.}} = -\overline{t}\left[1+\frac{\log\left(-\overline{t}\frac{\tau}{\overline{\tau}_{\text{w}}}\right)}{-\overline{t}\frac{\tau}{\overline{\tau}_{\text{w}}}}+\frac{\overline{a}_1}{-\overline{t}\frac{\tau}{\overline{\tau}_{\text{w}}}}+\frac{\log\left(-\overline{t}\frac{\tau}{\overline{\tau}_{\text{w}}}\right)}{\left(-\overline{t}\frac{\tau}{\overline{\tau}_{\text{w}}}\right)^2}+\frac{\overline{a}_1+\frac{5+\gamma}{1+\gamma}}{\left(-\overline{t}\frac{\tau}{\overline{\tau}_{\text{w}}}\right)^2}+\text{H.O.T.}\right]. \tag{D.9}$$

Finally, the function K relates the normalized speed to the non-dimensional variable θ ($\theta = K\left(\nu,\gamma,\overline{U}_{\text{s}}\right)$):

$$K_{\text{St.}} = \frac{n}{\overline{U}_{\text{s}}}\left[1+\frac{2a_2^{\pm}\left(1-n\right)n}{\left(\alpha^{\pm}\overline{U}_{\text{s}}\right)^2}+\frac{2\left(1-n\right)n^2\left[2a_3^{\pm}n+\left(a_2^{\pm}\right)^2\left(4-3n\right)\right]}{\left(\alpha^{\pm}\overline{U}_{\text{s}}\right)^4}+\text{H.O.T.}\right], \tag{D.10}$$

$$K_{\text{W., cyl.}} = -1 - 2\left(1+\overline{U}_{\text{s}}\right) - \left[4\left(1-\overline{a}_2\right) - \frac{19+3\gamma}{2\left(1+\gamma\right)}\left[1+\log\left(-2\left(1+\overline{U}_{\text{s}}\right)\right)\right]\right]\left(1+\overline{U}_{\text{s}}\right)^2 + \text{H.O.T.}, \quad \text{(D.11)}$$

$$K_{\text{W., sph.}} = -1 + \left[\log\left(-\left(1+\overline{U}_{\text{s}}\right)\right) - \overline{a}_1\right]\left(1+\overline{U}_{\text{s}}\right) + \left[1 - \frac{4}{1+\gamma}\left[\log\left(-\left(1+\overline{U}_{\text{s}}\right)\right) - \overline{a}_1\right]\right]\left(1+\overline{U}_{\text{s}}\right)^2 + \text{H.O.T.} \quad \text{(D.12)}$$

D.2 Normalized Forms of ρ, P, u, and t

Only the strong shock expansion results are considered in this section. First, since the density is not singular when r tends to 0, the density can simply be normalized by ρ_{I}. The pressure and the velocity, however, become singular for r tending to 0. For that reason, following Guderley's normalization [19], we use the non-dimensional variables $\frac{P}{\rho_{\text{I}}\left|U_{\text{s}}(r)^-\right|^2}$ and $\frac{u}{\left|U_{\text{s}}(r)^-\right|}$. Note that this means that the variables at $(r,\, t)$ are normalized using the speed of the incoming shock when it passes through the radius r, and not the speed of the shock at the same time t. We get the following expressions:

$$\frac{\rho}{\rho_{\text{I}}} = \rho_1(\eta)\left[1 + \rho_2(\eta)\left(\frac{r}{c_{\text{I}}\overline{\tau}_{\text{s}}}\right)^{\frac{2(1-n)}{n}} + \rho_3(\eta)\left(\frac{r}{c_{\text{I}}\overline{\tau}_{\text{s}}}\right)^{\frac{4(1-n)}{n}} + \text{H.O.T.}\right], \quad \text{(D.13)}$$

$$\frac{P}{\rho_{\text{I}}\left|U_{\text{s}}(r)^-\right|^2} = \frac{P_1(\eta)}{\left(\alpha^{\pm}\right)^2\gamma}\left[1 + \left(P_2(\eta) - \frac{2\overline{a}_2^-}{n^2\gamma}\right)\left(\frac{r}{c_{\text{I}}\overline{\tau}_{\text{s}}}\right)^{\frac{2(1-n)}{n}} + \left(P_3(\eta) - \frac{2\overline{a}_2^-}{n^2\gamma}P_2(\eta) + \frac{3\left(\overline{a}_2^-\right)^2 - 2\overline{a}_3^-}{n^4\gamma^2}\right)\left(\frac{r}{c_{\text{I}}\overline{\tau}_{\text{s}}}\right)^{\frac{4(1-n)}{n}} + \text{H.O.T.}\right], \quad \text{(D.14)}$$

$$\frac{u}{\left|U_{\text{s}}(r)^-\right|} = \frac{u_1(\eta)}{\alpha^{\pm}}\left[1 + \left(u_2(\eta) - \frac{\overline{a}_2^-}{n^2\gamma}\right)\left(\frac{r}{c_{\text{I}}\overline{\tau}_{\text{s}}}\right)^{\frac{2(1-n)}{n}} + \left(u_3(\eta) - \frac{\overline{a}_2^-}{n^2\gamma}u_2(\eta) + \frac{\left(\overline{a}_2^-\right)^2 - \overline{a}_3^-}{n^4\gamma^2}\right)\left(\frac{r}{c_{\text{I}}\overline{\tau}_{\text{s}}}\right)^{\frac{4(1-n)}{n}} + \text{H.O.T.}\right], \quad \text{(D.15)}$$

with

$$\overline{a}_2^- = a_2^- n\gamma\left(3-2n\right), \tag{D.16}$$

$$\overline{a}_3^- = n^2\gamma^2\left[a_3^- n\left(5-4n\right) - \frac{\left(a_2^-\right)^2}{2}\left(1-n\right)\left(7-4n\right)\right]. \tag{D.17}$$

Finally, if we want to plot the results in terms of time, the time can be normalized by the time at which the incoming shock passes though the radius r. We obtain a normalized time of the form

$$\frac{t}{\left|t_{\mathrm{s}}(r)^-\right|} = \alpha^{\pm}\eta^{\frac{1}{n}}\left[1+\frac{a_2^- - a_2^{\pm}\eta^{\frac{2(1-n)}{n}}}{n}\left(\frac{r}{c_{\mathrm{I}}\overline{\tau}_{\mathrm{s}}}\right)^{\frac{2(1-n)}{n}} + \frac{2a_3^- n - 3\left(a_2^-\right)^2\left(1-n\right) - 2a_2^{\pm}a_2^-\eta^{\frac{2(1-n)}{n}} + \left[\left(a_2^{\pm}\right)^2\left(5-3n\right) - 2a_3^{\pm}n\right]\eta^{\frac{4(1-n)}{n}}}{2n^2}\times \left(\frac{r}{c_{\mathrm{I}}\overline{\tau}_{\mathrm{s}}}\right)^{\frac{4(1-n)}{n}} + \mathrm{H.O.T.}\right], \tag{D.18}$$

with $a_2^{\pm}$ and $a_3^{\pm}$ being a_2^- and a_3^- in the incoming shock case, and a_2^+ and a_3^+ in the reflected shock case. From this expression, it is easy to find the time at which the shock crosses the radius r since it corresponds to $\eta = 1$:

$$\frac{t_{\mathrm{s}}(r)}{\left|t_{\mathrm{s}}(r)^-\right|} = \alpha^{\pm}\left[1+\frac{a_2^- - a_2^{\pm}}{n}\left(\frac{r}{c_{\mathrm{I}}\overline{\tau}_{\mathrm{s}}}\right)^{\frac{2(1-n)}{n}} + \left[\frac{a_3^- - a_3^{\pm}}{n} - \left(\frac{3}{2}\frac{1-n}{n}\left(a_2^- + a_2^{\pm}\right) + \frac{a_2^{\pm}}{n}\right)\frac{a_2^- - a_2^{\pm}}{n}\right]\left(\frac{r}{c_{\mathrm{I}}\overline{\tau}_{\mathrm{s}}}\right)^{\frac{4(1-n)}{n}} + \mathrm{H.O.T.}\right], \tag{D.19}$$

which gives, of course, -1 for the incoming shock case. It is important to see that there is a direct relationship between the incoming shock Mach number and the ratio $\frac{r}{c_{\mathrm{I}}\overline{\tau}_{\mathrm{s}}}$, since we have

$$\left|\frac{U_{\mathrm{s}}}{c_{\mathrm{I}}}\right| = n\left(\frac{r}{c_{\mathrm{I}}\overline{\tau}_{\mathrm{s}}}\right)^{\frac{n-1}{n}}\left[1+\frac{\overline{a}_2^-}{\gamma n^2}\left(\frac{r}{c_{\mathrm{I}}\overline{\tau}_{\mathrm{s}}}\right)^{\frac{2(1-n)}{n}} + \frac{\overline{a}_3^-}{\gamma^2 n^4}\left(\frac{r}{c_{\mathrm{I}}\overline{\tau}_{\mathrm{s}}}\right)^{\frac{4(1-n)}{n}} + \mathrm{H.O.T.}\right]. \tag{D.20}$$

This means that if we measure the flow property evolution at a particular radius, r, we can

find the appropriate value of $\frac{r}{c_1 \bar{\tau}_s}$ that has to be used in the strong shock expansions, simply by measuring the incoming shock Mach number when it crosses r.

Appendix E

Expansion Results

Some of the expansion results are presented here. The constants n, α^+, a_2^-, a_2^+, a_3^-, a_3^+, and η^* are presented with an estimated number of significant digits. The strong shock series expansion calculations were made using 2,000, 2,000, and 1,000 points in regions II, III, and IV, respectively. The same calculations were then made using twice as many points. The discrepancy between the two gives an estimation of the error and the number of significant digits in each of the values.

The characteristic program described in Section 3.2 was used to obtain the values of $\frac{\overline{\tau}_{\mathrm{w}}}{\tau}$, $\frac{\overline{\tau}_{\mathrm{s}}}{\tau}$, and $\overline{a}_2$ (axisymmetric case) or $\overline{a}_1$ (spherical case). As explained earlier, the accuracy of these constants is not very high. This is the reason why only 4 significant digits are displayed.

Note that the coefficients a_3^- and a_3^+ become infinite in the spherical case for a γ around 1.6. Although it was not verified, it is possible that in that particular case, the shock displacement can be rewritten as

$$R_{\mathrm{s}}(t) = c_1 \overline{\tau}_{\mathrm{s}} \left(\frac{t}{\alpha^{\pm} \overline{\tau}_{\mathrm{s}}} \right)^n \left[1 + a_2^{\pm} \left(\frac{t}{\alpha^{\pm} \overline{\tau}_{\mathrm{s}}} \right)^{2(1-n)} + a_3^{\pm} \left(\frac{t}{\alpha^{\pm} \overline{\tau}_{\mathrm{s}}} \right)^{4(1-n)} \log\left(\frac{t}{\alpha^{\pm} \overline{\tau}_{\mathrm{s}}} \right) + \mathrm{H.O.T.} \right]. \quad \text{(E.1)}$$

The log expression does not really change the order of the third term since, like what was done in the weak series expansion case (Section 2.4), a log expression can be considered as being of 0th order.

Table E.1 — Series expansion values for a cylindrical shock ($\nu = 2$)

γ	n	α^+	a_2^-	a_2^+	a_3^-	a_3^+	η^*	$\overline{a}_2$	$\frac{\overline{\tau}_s}{\tau}$	$\frac{\overline{\tau}_w}{\tau}$
1.050	0.907120601	29.0640633	–6.4746125	76.60	60.6051	1654	0.928040014	0.7881	7517	39.91
1.055	0.9042592225	26.2393001	–5.7129245	71.44	51.8923	1293	0.925240208	0.7857	6228	39.51
1.060	0.9016047352	23.8816201	–5.0842156	66.93	45.0081	1016	0.922612632	0.7833	5266	39.13
1.065	0.8991278783	21.8854015	–4.5570891	62.934	39.4614	800	0.920135253	0.7809	4526	38.75
1.070	0.8968053224	20.1746363	–4.1092441	59.364	34.9179	629	0.9177902806	0.7785	3897	38.38
1.075	0.8946181467	18.69321324	–3.72441491	56.152	31.1431	492.6	0.9155631060	0.7761	3365	38.01
1.080	0.8925507798	17.39879704	–3.39046603	53.241	27.9682	382.7	0.9134415661	0.7738	2894	37.66
1.085	0.8905902433	16.25883991	–3.09816425	50.589	25.2691	293.4	0.9114154071	0.7715	2483	37.30
1.090	0.8887255994	15.24790492	–2.84036346	48.161	22.9526	220.6	0.9094758924	0.7691	2127	36.96
1.095	0.8869475396	14.34582347	–2.61144904	45.928	20.9478	160.8	0.9076155071	0.7668	1820	36.62
1.100	0.8852480723	13.53639823	–2.40695020	43.867	19.1994	111.6	0.9058277329	0.7645	1562	36.28
1.105	0.8836202835	12.80647168	–2.22326423	41.959	17.6645	71.0	0.9041068735	0.7623	1345	35.96
1.110	0.8820581488	12.14524540	–2.05745657	40.186	16.3085	37.4	0.9024479176	0.7600	1161	35.63
1.115	0.8805563860	11.54377460	–1.90711361	38.534	15.1040	9.6	0.9008464290	0.7577	1008	35.32
1.120	0.8791103364	10.99458734	–1.77023256	36.993	14.0285	–13.4	0.8992984594	0.7555	880.2	35.01
1.125	0.8777158696	10.49139398	–1.64513814	35.550	13.0638	–32.5	0.8978004766	0.7533	772.2	34.70
1.130	0.8763693058	10.02886286	–1.53041862	34.197	12.1946	–48.2	0.8963493064	0.7510	681.5	34.40
1.135	0.87506735224	9.60244509	–1.42487628	32.926	11.4084	–61.1	0.8949420838	0.7488	605.0	34.10
1.140	0.87380704973	9.208236566	–1.32748858	31.730	10.6947	–71.7	0.8935762128	0.7466	540.0	33.81
1.145	0.87258572920	8.842868069	–1.23737746	30.603	10.0446	–80.4	0.8922493328	0.7444	484.5	33.53
1.150	0.87140097447	8.503417129	–1.15378486	29.539	9.4504	–87.4	0.8909592901	0.7423	437.0	33.24
1.155	0.87025059103	8.187336746	–1.07605302	28.5327	8.9058	–92.98	0.8897041130	0.7401	396.0	32.97
1.160	0.86913257957	7.892397312	–1.00360857	27.5806	8.4053	–97.39	0.8884819918	0.7380	360.6	32.69
1.165	0.86804511332	7.616638978	–0.93594948	26.6784	7.9440	–100.79	0.8872912608	0.7358	329.8	32.43
1.170	0.86698651859	7.358332335	–0.87263440	25.8225	7.5179	–103.35	0.8861303827	0.7337	302.8	32.16

Continued on next page

Table E.1 — Series expansion values for a cylindrical shock ($\nu = 2$) — Continued from previous page

γ	n	α^+	a_2^-	a_2^+	a_3^-	a_3^+	η^*	$\overline{a}_2$	$\frac{\overline{\tau}_s}{\tau}$	$\frac{\overline{\tau}_w}{\tau}$
1.175	0.86595525803	7.115945760	–0.81327381	25.0095	7.1233	–105.19	0.8849979353	0.7316	279.2	31.90
1.180	0.86494991611	6.888118156	–0.75752270	24.2366	6.7571	–106.43	0.8838926003	0.7295	258.3	31.65
1.185	0.86396918649	6.673636058	–0.70507444	23.5011	6.4166	–107.15	0.8828131527	0.7274	239.8	31.39
1.190	0.86301186102	6.471414329	–0.65565561	22.8005	6.0994	–107.43	0.8817584520	0.7253	223.4	31.15
1.195	0.86207682003	6.280479791	–0.60902168	22.1326	5.8033	–107.35	0.8807274344	0.7232	208.7	30.90
1.200	0.86116302390	6.099957294	–0.56495331	21.4953	5.5264	–106.97	0.8797191058	0.7212	195.6	30.66
1.205	0.86026950553	5.929057802	–0.52325323	20.8867	5.2671	–106.32	0.87873253602	0.7191	183.7	30.42
1.210	0.85939536368	5.767068177	–0.48374354	20.3050	5.0238	–105.46	0.87776685254	0.7171	173.0	30.19
1.215	0.85853975716	5.6133423631	–0.44626341	19.7487	4.7952	–104.43	0.87682123631	0.7151	163.4	29.96
1.220	0.85770189949	5.4672937803	–0.41066711	19.2163	4.5801	–103.24	0.87589491707	0.7131	154.6	29.74
1.225	0.85688105431	5.3283887122	–0.37682229	18.7064	4.3775	–101.94	0.87498716949	0.7111	146.6	29.51
1.230	0.85607653111	5.1961405594	–0.34460849	18.2178	4.1863	–100.53	0.87409730962	0.7091	139.3	29.29
1.235	0.85528768154	5.0701048192	–0.31391585	17.7491	4.0057	–99.06	0.87322469173	0.7071	132.6	29.08
1.240	0.85451389599	4.9498746904	–0.28464397	17.2994	3.8349	–97.52	0.87236870540	0.7051	126.4	28.86
1.245	0.85375460055	4.8350772136	–0.25670095	16.8676	3.6732	–95.93	0.87152877297	0.7031	120.8	28.65
1.250	0.85300925426	4.7253698730	–0.23000247	16.4528	3.5199	–94.31	0.87070434711	0.7012	115.6	28.45
1.255	0.85227734662	4.6204375970	–0.20447110	16.0541	3.3744	–92.67	0.86989490873	0.6992	110.8	28.24
1.260	0.85155839536	4.51999010318	–0.18003553	15.6705	3.2361	–91.02	0.86909996495	0.6973	106.3	28.04
1.265	0.85085194430	4.423759544215	–0.15663008	15.3015	3.1047	–89.36	0.86831904741	0.6954	102.1	27.84
1.270	0.85015756160	4.33149841393	–0.13419408	14.9462	2.9796	–87.70	0.86755171052	0.6935	98.29	27.65
1.275	0.84947483795	4.24297768229	–0.11267144	14.6039	2.8605	–86.05	0.86679753006	0.6916	94.70	27.45
1.280	0.84880338508	4.1579851299	–0.09201025	14.2740	2.7468	–84.40	0.86605610174	0.6897	91.34	27.26
1.285	0.84814283430	4.0763238579	–0.07216236	13.9559	2.6384	–82.78	0.86532703997	0.6878	88.21	27.08
1.290	0.84749283522	3.9978109522	–0.05308307	13.6491	2.5348	–81.169	0.86460997668	0.6859	85.27	26.89
1.295	0.84685305452	3.9222762836	–0.03473085	13.3530	2.4358	–79.581	0.86390456026	0.6841	82.52	26.71

Continued on next page

Table E.1 — Series expansion values for a cylindrical shock ($\nu = 2$) — Continued from previous page

γ	n	α^+	a_2^-	a_2^+	a_3^-	a_3^+	η^*	$\overline{a}_2$	$\frac{\overline{\tau}_s}{\tau}$	$\frac{\overline{\tau}_w}{\tau}$
1.300	0.846223174891	3.8495614287	–0.01706703	13.06710	2.3411	–78.016	0.86321045456	0.6822	79.93	26.53
1.305	0.845602893970	3.7795186965	–0.00005557	12.79093	2.2504	–76.477	0.86252733797	0.6804	77.50	26.35
1.310	0.844991923446	3.7120102502	0.01633713	12.52406	2.1636	–74.963	0.86185490259	0.6785	75.21	26.18
1.315	0.844389988181	3.6469073125	0.03214246	12.26607	2.0803	–73.478	0.86119285343	0.6767	73.04	26.00
1.320	0.843796825411	3.5840894462	0.0473898	12.01656	2.0004	–72.020	0.86054090768	0.6749	71.00	25.83
1.325	0.843212184014	3.5234439015	0.0621065	11.77515	1.9237	–70.592	0.85989879407	0.6731	69.07	25.67
1.330	0.842635823825	3.4648650224	0.0763185	11.54151	1.8500	–69.193	0.85926625216	0.6713	67.24	25.50
1.335	0.842067514997	3.4082537077	0.0900497	11.31528	1.7791	–67.824	0.85864303185	0.6695	65.51	25.34
1.340	0.841507037422	3.3535169191	0.1033230	11.09616	1.7110	–66.484	0.85802889274	0.6677	63.87	25.17
1.345	0.840954180173	3.3005672325	0.1161594	10.88384	1.6454	–65.175	0.85742360372	0.6659	62.31	25.01
1.350	0.840408741004	3.2493224285	0.1285791	10.67805	1.5823	–63.894	0.85682694239	0.6642	60.82	24.86
1.355	0.839870525869	3.1997051177	0.1406010	10.47851	1.5215	–62.644	0.85623869468	0.6624	59.41	24.70
1.360	0.839339348486	3.1516423972	0.1522426	10.28497	1.4628	–61.422	0.85565865442	0.6607	58.07	24.55
1.365	0.838815029917	3.1050655359	0.1635208	10.09718	1.4063	–60.229	0.85508662295	0.6589	56.78	24.40
1.370	0.838297398189	3.0599096861	0.1744514	9.91492	1.3517	–59.065	0.85452240874	0.6572	55.56	24.25
1.375	0.837786287929	3.0161136173	0.1850492	9.73797	1.2990	–57.928	0.85396582704	0.6555	54.39	24.10
1.380	0.837281540030	2.9736194724	0.1953283	9.56612	1.2481	–56.819	0.85341669960	0.6537	53.27	23.95
1.385	0.836783001331	2.9323725427	0.2053021	9.39917	1.1989	–55.737	0.85287485431	0.6520	52.20	23.81
1.390	0.836290524323	2.8923210601	0.2149831	9.23693	1.1513	–54.681	0.85234012495	0.6503	51.18	23.67
1.395	0.835803966871	2.8534160062	0.2243833	9.07922	1.1053	–53.651	0.85181235092	0.6487	50.20	23.53
1.400	0.835323191953	2.8156109349	0.2335140	8.92588	1.0608	–52.646	0.85129137696	0.6470	49.26	23.39
1.405	0.834848067412	2.7788618095	0.2423860	8.77674	1.0177	–51.666	0.85077705295	0.6453	48.35	23.25
1.410	0.834378465729	2.7431268504	0.2510093	8.63164	0.9760	–50.710	0.85026923363	0.6436	47.49	23.12
1.415	0.833914263803	2.7083663960	0.2593937	8.49044	0.9355	–49.777	0.84976777846	0.6420	46.65	22.98
1.420	0.833455342747	2.6745427715	0.2675483	8.35300	0.8963	–48.867	0.84927255133	0.6403	45.85	22.85

Continued on next page

Table E.1 — Series expansion values for a cylindrical shock ($\nu = 2$) — Continued from previous page

γ	n	α^+	a_2^-	a_2^+	a_3^-	a_3^+	η^*	$\overline{a}_2$	$\frac{\overline{\tau}_s}{\tau}$	$\frac{\overline{\tau}_w}{\tau}$
1.425	0.833001587695	2.6416201690	0.2754819	8.21918	0.8583	–47.980	0.84878342046	0.6387	45.08	22.72
1.430	0.832552887621	2.6095645352	0.2832028	8.08885	0.8214	–47.115	0.84830025813	0.6371	44.34	22.59
1.435	0.832109135166	2.5783434667	0.2907189	7.96188	0.7856	–46.270	0.84782294060	0.6354	43.63	22.46
1.440	0.831670226476	2.5479261138	0.2980376	7.83817	0.7508	–45.446	0.84735134788	0.6338	42.94	22.34
1.445	0.831236061049	2.5182830895	0.3051662	7.71760	0.7170	–44.643	0.84688536358	0.6322	42.27	22.21
1.450	0.830806541592	2.4893863857	0.3121115	7.60005	0.6842	–43.859	0.84642487481	0.6306	41.63	22.09
1.455	0.830381573878	2.4612092946	0.3188801	7.48544	0.6524	–43.094	0.84596977201	0.6290	41.01	21.97
1.460	0.829961066624	2.4337263356	0.3254780	7.37365	0.6214	–42.347	0.84551994881	0.6274	40.42	21.85
1.465	0.829544931360	2.4069131864	0.3319114	7.26459	0.5912	–41.619	0.84507530192	0.6259	39.84	21.73
1.470	0.829133082320	2.3807466196	0.3381858	7.15818	0.5619	–40.907	0.84463573103	0.6243	39.28	21.61
1.475	0.828725436324	2.3552044427	0.3443067	7.05433	0.5334	–40.213	0.84420113864	0.6227	38.74	21.49
1.480	0.828321912678	2.3302654420	0.3502792	6.95295	0.5056	–39.536	0.84377143001	0.6212	38.22	21.38
1.485	0.827922433072	2.3059093302	0.3561084	6.85396	0.4786	–38.875	0.84334651303	0.6196	37.71	21.27
1.490	0.827526921487	2.2821166973	0.3617989	6.75728	0.4522	–38.229	0.84292629813	0.6181	37.22	21.15
1.495	0.827135304104	2.2588689645	0.3673554	6.66285	0.4266	–37.598	0.84251069817	0.6165	36.75	21.04
1.500	0.826747509216	2.2361483410	0.3727821	6.57059	0.4015	–36.982	0.84209962840	0.6150	36.29	20.93
1.505	0.826363467150	2.2139377833	0.3780832	6.48043	0.3771	–36.381	0.84169300630	0.6135	35.84	20.83
1.510	0.825983110188	2.1922209570	0.3832628	6.392317	0.3533	–35.794	0.84129075156	0.6120	35.41	20.72
1.515	0.825606372495	2.1709822011	0.3883247	6.306175	0.3301	–35.220	0.84089278597	0.6105	34.99	20.61
1.520	0.825233190042	2.1502064941	0.3932725	6.221949	0.3075	–34.659	0.84049903338	0.6090	34.58	20.51
1.525	0.824863500548	2.1298794224	0.3981099	6.139580	0.2854	–34.111	0.84010941959	0.6075	34.18	20.40
1.530	0.824497243410	2.1099871501	0.4028400	6.059013	0.2638	–33.575	0.83972387229	0.6060	33.80	20.30
1.535	0.824134359643	2.0905163911	0.4074664	5.980193	0.2428	–33.052	0.83934232103	0.6045	33.42	20.20
1.540	0.823774791821	2.0714543824	0.4119920	5.903070	0.2222	–32.540	0.83896469712	0.6030	33.06	20.10
1.545	0.823418484026	2.0527888592	0.4164198	5.827592	0.2021	–32.040	0.83859093358	0.6016	32.70	20.00

Continued on next page

Table E.1 — Series expansion values for a cylindrical shock ($\nu = 2$) — Continued from previous page

γ	n	α^+	a_2^-	a_2^+	a_3^-	a_3^+	η^*	$\overline{a}_2$	$\frac{\overline{\tau}_s}{\tau}$	$\frac{\overline{\tau}_w}{\tau}$
1.550	0.823065381787	2.0345080309	0.4207529	5.753714	0.1824	–31.551	0.83822096508	0.6001	32.36	19.90
1.555	0.8227154320358	2.0166005591	0.4249939	5.681387	0.1632	–31.073	0.83785472792	0.5986	32.02	19.80
1.560	0.8223685830545	1.9990555364	0.4291455	5.610568	0.1444	–30.605	0.83749215993	0.5972	31.70	19.71
1.565	0.8220247844309	1.9818624662	0.4332103	5.541214	0.1261	–30.148	0.83713320043	0.5958	31.38	19.61
1.570	0.8216839870129	1.9650112444	0.4371909	5.473283	0.1081	–29.700	0.83677779021	0.5943	31.07	19.52
1.575	0.8213461428665	1.9484921410	0.4410895	5.406736	0.0905	–29.263	0.83642587146	0.5929	30.77	19.42
1.580	0.8210112052344	1.9322957834	0.4449085	5.341534	0.0733	–28.834	0.83607738774	0.5915	30.47	19.33
1.585	0.8206791284974	1.9164131406	0.4486501	5.277639	0.0565	–28.415	0.835732283910	0.5901	30.18	19.24
1.590	0.8203498681365	1.9008355077	0.4523165	5.215016	0.0400	–28.005	0.835390506118	0.5887	29.90	19.15
1.595	0.8200233806972	1.8855544919	0.4559097	5.153630	0.0239	–27.603	0.835052001752	0.5873	29.63	19.06
1.600	0.8196996237550	1.8705619985	0.4594317	5.093448	0.0080	–27.210	0.834716719399	0.5859	29.36	18.97
1.605	0.8193785558819	1.8558502182	0.4628844	5.034438	–0.0074	–26.825	0.834384608811	0.5845	29.10	18.88
1.610	0.8190601366154	1.8414116149	0.4662698	4.976568	–0.0226	–26.448	0.834055620868	0.5831	28.85	18.80
1.615	0.8187443264273	1.8272389140	0.4695895	4.919807	–0.0375	–26.078	0.833729707548	0.5817	28.60	18.71
1.620	0.8184310866947	1.8133250910	0.4728453	4.864128	–0.0521	–25.717	0.833406821890	0.5803	28.36	18.63
1.625	0.8181203796719	1.7996633616	0.4760389	4.809501	–0.0664	–25.362	0.833086917967	0.5790	28.12	18.54
1.630	0.8178121684633	1.7862471713	0.4791719	4.755900	–0.0804	–25.015	0.832769950853	0.5776	27.89	18.46
1.635	0.8175064169976	1.7730701858	0.4822459	4.703297	–0.0942	–24.675	0.832455876597	0.5763	27.66	18.38
1.640	0.8172030900023	1.7601262823	0.4852623	4.651668	–0.1077	–24.342	0.832144652191	0.5749	27.44	18.30
1.645	0.8169021529802	1.7474095409	0.4882227	4.600988	–0.1209	–24.015	0.831836235547	0.5736	27.22	18.21
1.650	0.8166035721860	1.7349142359	0.4911284	4.551233	–0.1339	–23.695	0.831530585468	0.5722	27.01	18.13
1.655	0.8163073146039	1.7226348286	0.4939809	4.502379	–0.1467	–23.381	0.831227661626	0.5709	26.81	18.06
1.660	0.8160133479266	1.7105659594	0.4967813	4.454405	–0.1592	–23.073	0.830927424536	0.5696	26.60	17.98
1.665	0.8157216405340	1.6987024411	0.4995311	4.407288	–0.1715	–22.771	0.830629835532	0.5683	26.40	17.90
1.667	0.8156229691667	1.6947147269	0.5004547	4.391459	–0.1756	–22.670	0.830529251753	0.5678	26.34	17.87

Table E.2 — Series expansion values for a spherical shock ($\nu = 3$)

γ	n	α^+	a_2^-	a_2^+	a_3^-	a_3^+	η^*	$\overline{a}_1$	$\frac{\overline{\tau}_s}{\tau}$	$\frac{\overline{\tau}_w}{\tau}$
1.050	0.832246954	38.173922	–6.7285492	239.28	74.66	12490	0.948196501	–0.8100	197.0	3.556
1.055	0.827448722	34.119424	–5.95498480	222.59	64.56	9640	0.9460971417	–0.8082	182.0	3.539
1.060	0.823011662	30.7415845	–5.315173030	207.59	56.56	7420	0.9441182743	–0.8065	166.5	3.521
1.065	0.8188837704	27.8896924	–4.77763341	194.04	50.08	5680	0.9422446210	–0.8048	149.7	3.504
1.070	0.8150237279	25.4545150	–4.31999217	181.74	44.76	4312	0.9404638471	–0.8031	133.7	3.488
1.075	0.8113981248	23.3549010	–3.92592023	170.51	40.31	3226	0.9387658272	–0.8014	119.1	3.471
1.080	0.8079795432	21.5292811	–3.58322698	160.24	36.56	2363	0.9371421298	–0.7997	105.7	3.455
1.085	0.8047451908	19.9300899	–3.28263135	150.81	33.36	1679	0.9355856470	–0.7981	94.32	3.439
1.090	0.8016759051	18.5199986	–3.01694550	142.13	30.60	1135	0.9340903221	–0.7964	84.21	3.423
1.095	0.7987554143	17.2693055	–2.78051824	134.135	28.20	703	0.9326509443	–0.7947	75.92	3.407
1.100	0.7959697783	16.1540883	–2.568846674	126.747	26.10	362	0.9312629934	–0.7931	68.47	3.392
1.105	0.7933069591	15.1548700	–2.378299757	119.912	24.25	92	0.9299225178	–0.7914	62.33	3.376
1.110	0.7907564872	14.25563833	–2.20591785	113.578	22.60	–119	0.9286260402	–0.7898	56.96	3.361
1.115	0.7883091979	13.44311437	–2.04926502	107.700	21.14	–283	0.9273704816	–0.7881	52.41	3.346
1.120	0.7859570212	12.70619877	–1.90631859	102.237	19.82	–410	0.9261531002	–0.7865	48.22	3.332
1.125	0.7836928128	12.03554728	–1.77538548	97.155	18.64	–507	0.9249714424	–0.7849	44.72	3.317
1.130	0.7815102167	11.42324154	–1.6550379	92.421	17.57	–579	0.9238233022	–0.7833	41.65	3.303
1.135	0.7794035522	10.86253114	–1.5440639	88.006	16.60	–632	0.9227066876	–0.7817	39.02	3.289
1.140	0.7773677209	10.34762941	–1.4414276	83.883	15.71	–669	0.9216197927	–0.7801	36.50	3.275
1.145	0.7753981293	9.87355047	–1.3462394	80.030	14.90	–693	0.9205609746	–0.7785	34.36	3.261
1.150	0.7734906235	9.43597794	–1.2577303	76.424	14.15	–708.1	0.9195287331	–0.7769	32.46	3.247
1.155	0.7716414343	9.03115856	–1.1752329	73.047	13.47	–714.9	0.9185216946	–0.7753	30.76	3.234
1.160	0.76984713148	8.65581527	–1.0981649	69.8806	12.83	–715.4	0.9175385972	–0.7737	29.20	3.220
1.165	0.76810458317	8.30707568	–1.0260159	66.9087	12.25	–711.0	0.91657827860	–0.7722	27.82	3.207
1.170	0.76641092256	7.98241300	–0.9583371	64.1166	11.71	–702.8	0.91563966557	–0.7706	26.54	3.194

Continued on next page

Table E.2 — Series expansion values for a spherical shock ($\nu = 3$) — Continued from previous page

γ	n	α^+	a_2^-	a_2^+	a_3^-	a_3^+	η^*	$\overline{a}_1$	$\frac{\overline{\tau}_s}{\tau}$	$\frac{\overline{\tau}_w}{\tau}$
1.175	0.76476351841	7.67959689	–0.8947322	61.4909	11.20	–691.8	0.91472176457	–0.7689	25.39	3.181
1.180	0.76315994973	7.396652279	–0.8348497	59.0195	10.73	–678.5	0.91382365382	–0.7673	24.33	3.169
1.185	0.76159798386	7.131824858	–0.7783770	56.6910	10.29	–663.7	0.91294447623	–0.7658	23.38	3.156
1.190	0.76007555727	6.883551897	–0.7250354	54.4952	9.88	–647.7	0.91208343327	–0.7643	22.49	3.144
1.195	0.75859075876	6.650437503	–0.6745753	52.4228	9.49	–630.9	0.91123977951	–0.7628	21.67	3.131
1.200	0.75714181478	6.431231558	–0.6267725	50.4650	9.13	–613.7	0.91041281789	–0.7612	20.93	3.119
1.205	0.75572707635	6.224811709	–0.5814255	48.6138	8.78	–596.2	0.90960189536	–0.7597	20.23	3.107
1.210	0.75434500764	6.030167929	–0.5383524	46.8621	8.46	–578.7	0.90880639918	–0.7582	19.60	3.095
1.215	0.75299417577	5.846389204	–0.4973884	45.2031	8.16	–561.3	0.90802575351	–0.7567	18.99	3.083
1.220	0.75167324171	5.672652052	–0.4583844	43.6306	7.87	–544.2	0.90725941635	–0.7552	18.43	3.072
1.225	0.75038095224	5.508210562	–0.4212047	42.1388	7.60	–527.3	0.90650687690	–0.7537	17.90	3.060
1.230	0.74911613267	5.352387739	–0.3857256	40.7226	7.34	–510.8	0.90576765306	–0.7522	17.43	3.049
1.235	0.74787768042	5.204567961	–0.3518345	39.3771	7.09	–494.7	0.90504128925	–0.7508	16.96	3.038
1.240	0.74666455916	5.064190383	–0.3194282	38.0978	6.86	–479.1	0.90432735442	–0.7493	16.53	3.027
1.245	0.74547579357	4.9307431577	–0.2884122	36.8804	6.64	–464.0	0.90362544024	–0.7478	16.13	3.016
1.250	0.74431046461	4.8037583570	–0.2586998	35.7213	6.42	–449.4	0.90293515949	–0.7464	15.75	3.005
1.255	0.74316770524	4.6828075002	–0.2302113	34.61679	6.22	–435.3	0.90225614453	–0.7449	15.39	2.994
1.260	0.74204669652	4.5674976045	–0.2028732	33.56358	6.03	–421.7	0.90158804600	–0.7435	15.05	2.984
1.265	0.74094666412	4.4574676915	–0.1766178	32.55861	5.84	–408.6	0.90093053154	–0.7421	14.73	2.973
1.270	0.73986687509	4.35238568970	–0.1513826	31.59903	5.66	–396.0	0.90028328465	–0.7406	14.43	2.963
1.275	0.73880663494	4.25194568187	–0.1271096	30.68220	5.49	–383.9	0.89964600371	–0.7392	14.14	2.953
1.280	0.73776528498	4.1558654543	–0.103745	29.80566	5.33	–372.2	0.89901840096	–0.7378	13.87	2.942
1.285	0.73674219987	4.0638843109	–0.081239	28.96709	5.17	–361.0	0.89840020168	–0.7364	13.61	2.932
1.290	0.73573678538	3.9757611195	–0.059546	28.16438	5.02	–350.3	0.89779114335	–0.7349	13.36	2.922
1.295	0.73474847638	3.8912725626	–0.038623	27.39552	4.87	–340.0	0.89719097492	–0.7335	13.13	2.912

Continued on next page

Table E.2 — Series expansion values for a spherical shock ($\nu = 3$) — Continued from previous page

γ	n	α^+	a_2^-	a_2^+	a_3^-	a_3^+	η^*	$\overline{a}_1$	$\frac{\overline{\tau}_s}{\tau}$	$\frac{\overline{\tau}_w}{\tau}$
1.300	0.73377673489	3.8102115685	–0.018429	26.65866	4.73	–330.2	0.89659945612	–0.7321	12.90	2.903
1.305	0.73282104843	3.7323859022	0.001073	25.95205	4.60	–320.7	0.89601635686	–0.7307	12.69	2.893
1.310	0.73188092833	3.6576168966	0.019918	25.27407	4.47	–311.6	0.89544145656	–0.7293	12.48	2.883
1.315	0.73095590835	3.5857383094	0.038138	24.62322	4.34	–302.9	0.89487454370	–0.7279	12.29	2.874
1.320	0.73004554323	3.5165952917	0.055763	23.99805	4.21	–294.6	0.89431541526	–0.7266	12.10	2.865
1.325	0.72914940751	3.4500434543	0.072823	23.39725	4.09	–286.6	0.89376387627	–0.7252	11.92	2.855
1.330	0.728267094330	3.3859480236	0.089345	22.81956	3.98	–279.0	0.89321973936	–0.7238	11.75	2.846
1.335	0.727398214332	3.3241830753	0.105352	22.26382	3.87	–271.6	0.89268282436	–0.7225	11.59	2.837
1.340	0.726542394693	3.2646308396	0.120870	21.72892	3.75	–264.6	0.89215295794	–0.7211	11.43	2.828
1.345	0.725699278171	3.2071810689	0.135919	21.21384	3.65	–257.9	0.89162997323	–0.7198	11.28	2.819
1.350	0.724868522246	3.1517304621	0.150521	20.71760	3.54	–251.4	0.89111370947	–0.7184	11.13	2.810
1.355	0.724049798312	3.0981821407	0.164696	20.239294	3.44	–245.2	0.89060401178	–0.7171	10.99	2.802
1.360	0.723242790923	3.0464451697	0.178463	19.778062	3.34	–239.3	0.89010073078	–0.7157	10.86	2.793
1.365	0.722447197094	2.996434121	0.191838	19.333097	3.24	–233.6	0.88960372237	–0.7144	10.73	2.784
1.370	0.721662725643	2.948068671	0.204838	18.903636	3.14	–228.2	0.88911284745	–0.7131	10.60	2.776
1.375	0.720889096578	2.901273239	0.217478	18.488964	3.05	–223.0	0.88862797173	–0.7118	10.48	2.768
1.380	0.720126040527	2.855976647	0.229775	18.088401	2.96	–218.0	0.88814896542	–0.7105	10.36	2.759
1.385	0.719373298198	2.812111812	0.241740	17.701309	2.86	–213.3	0.88767570310	–0.7091	10.25	2.751
1.390	0.718630619878	2.769615466	0.253389	17.327084	2.77	–208.7	0.88720806349	–0.7078	10.14	2.743
1.395	0.717897764957	2.728427890	0.264733	16.965156	2.68	–204.3	0.88674592925	–0.7065	10.04	2.735
1.400	0.717174501488	2.688492680	0.275784	16.614985	2.59	–200.2	0.88628918681	–0.7052	9.933	2.727
1.405	0.716460605773	2.649756523	0.286553	16.276061	2.51	–196.2	0.88583772622	–0.7039	9.833	2.719
1.410	0.715755861966	2.612168992	0.297052	15.947899	2.42	–192.4	0.88539144098	–0.7027	9.737	2.711
1.415	0.715060061705	2.575682360	0.307289	15.630044	2.33	–188.7	0.88495022790	–0.7014	9.645	2.703
1.420	0.714373003771	2.540251425	0.317276	15.322060	2.24	–185.3	0.88451398693	–0.7001	9.556	2.696

Continued on next page

Table E.2 — Series expansion values for a spherical shock ($\nu = 3$) — Continued from previous page

γ	n	α^+	a_2^-	a_2^+	a_3^-	a_3^+	η^*	$\overline{a}_1$	$\frac{\overline{r}_s}{r}$	$\frac{\overline{r}_w}{r}$
1.425	0.713694493754	2.5058333498	0.327021	15.023537	2.15	–182.0	0.88408262107	–0.6988	9.469	2.688
1.430	0.713024343748	2.4723875110	0.336533	14.734085	2.06	–178.9	0.88365603621	–0.6976	9.385	2.680
1.435	0.712362372059	2.4398753632	0.345820	14.453333	1.98	–175.9	0.88323414105	–0.6963	9.304	2.673
1.440	0.711708402933	2.4082603097	0.354891	14.180929	1.89	–173.1	0.88281684692	–0.6950	9.225	2.665
1.445	0.711062266289	2.3775075838	0.363752	13.916540	1.79	–170.4	0.88240406776	–0.6938	9.148	2.658
1.450	0.710423797483	2.3475841385	0.372412	13.659847	1.70	–167.9	0.88199571994	–0.6925	9.072	2.651
1.455	0.709792837067	2.3184585437	0.380876	13.410550	1.61	–165.6	0.88159172220	–0.6913	9.000	2.644
1.460	0.709169230575	2.2901008906	0.389152	13.168360	1.51	–163.4	0.88119199557	–0.6901	8.930	2.636
1.465	0.708552828312	2.2624827030	0.397246	12.933004	1.41	–161.4	0.88079646326	–0.6888	8.860	2.629
1.470	0.707943485155	2.2355768541	0.405163	12.704222	1.31	–159.6	0.88040505057	–0.6876	8.795	2.622
1.475	0.707341060370	2.2093574895	0.412911	12.481764	1.20	–157.9	0.88001768485	–0.6864	8.729	2.615
1.480	0.706745417430	2.1837999546	0.420493	12.265396	1.09	–156.4	0.87963429538	–0.6851	8.667	2.608
1.485	0.706156423848	2.1588807280	0.427916	12.054891	0.98	–155.1	0.87925481333	–0.6839	8.607	2.601
1.490	0.705573951015	2.1345773575	0.435185	11.850034	0.86	–153.9	0.87887917166	–0.6827	8.546	2.595
1.495	0.704997874052	2.1108684021	0.442303	11.650619	0.73	–153.0	0.87850730510	–0.6815	8.489	2.588
1.500	0.704428071660	2.0877333768	0.449277	11.456451	0.60	–152.3	0.87813915006	–0.6803	8.432	2.581
1.505	0.703864425983	2.0651527003	0.456110	11.267342	0.45	–151.9	0.87777464454	–0.6791	8.378	2.575
1.510	0.703306822480	2.0431076477	0.462807	11.083113	0.30	–151.7	0.87741372815	–0.6779	8.325	2.568
1.515	0.702755149796	2.0215803043	0.469372	10.903593	0.13	–151.8	0.87705634198	–0.6767	8.273	2.561
1.520	0.702209299644	2.0005535237	0.475808	10.728618	–0.06	–152.3	0.87670242860	–0.6756	8.223	2.555
1.525	0.701669166695	1.9800108874	0.482120	10.558032	–0.27	–153.1	0.876351931973	–0.6744	8.172	2.549
1.530	0.701134648462	1.9599366678	0.488311	10.391685	–0.49	–154.5	0.876004797439	–0.6732	8.126	2.542
1.535	0.700605645204	1.9403157926	0.494385	10.229434	–0.75	–156.4	0.875660971648	–0.6720	8.081	2.536
1.540	0.700082059824	1.9211338119	0.500345	10.071140	–1.05	–159.0	0.875320402528	–0.6709	8.036	2.530
1.545	0.699563797774	1.9023768669	0.506194	9.916673	–1.39	–162.5	0.874983039237	–0.6697	7.993	2.524

Continued on next page

Table E.2 — Series expansion values for a spherical shock ($\nu = 3$) — Continued from previous page

γ	n	α^+	a_2^-	a_2^+	a_3^-	a_3^+	η^*	$\overline{a}_1$	$\frac{\overline{r}_s}{r}$	$\frac{\overline{r}_w}{r}$
1.550	0.699050766968	1.8840316604	0.511935	9.765906	–1.80	–167.1	0.874648832126	–0.6685	7.952	2.517
1.555	0.698542877693	1.8660854297	0.517572	9.618719	–2.29	–173.2	0.874317732701	–0.6674	7.913	2.511
1.560	0.698040042527	1.8485259200	0.523106	9.474994	–2.90	–181.3	0.873989693584	–0.6662	7.876	2.505
1.565	0.697542176262	1.8313413601	0.528542	9.334622	–3.67	–192.2	0.873664668480	–0.6651	7.842	2.499
1.570	0.697049195827	1.8145204392	0.533881	9.197494	–4.70	–207.5	0.873342612144	–0.6639	7.813	2.493
1.575	0.696561020217	1.7980522850	0.539127	9.063508	–6.13	–229.6	0.873023480343	–0.6628	7.790	2.487
1.580	0.696077570422	1.7819264430	0.544281	8.932567	–8.27	–264	0.872707229833	–0.6617	7.775	2.482
1.585	0.695598769363	1.7661328571	0.549347	8.804575	–11.9	–323	0.872393818320	–0.6605	7.778	2.476
1.590	0.695124541829	1.7506618512	0.554326	8.679440	–19.2	–445	0.872083204441	–0.6594	7.829	2.470
1.595	0.694654814413	1.7355041114	0.559220	8.557077	–42.8	–840	0.871775347728	–0.6583	8.086	2.464
1.600	0.694189515456	1.7206506699	0.564033	8.437400	∞	∞	0.871470208584	–0.6572	4.340	2.459
1.605	0.693728574991	1.7060928893	0.568765	8.320329	39.3	547	0.871167748261	–0.6561	7.056	2.453
1.610	0.6932719246886	1.6918224476	0.573419	8.205785	21.44	248.1	0.870867928827	–0.6549	7.212	2.448
1.615	0.6928194978045	1.6778313242	0.577997	8.093695	15.1222	143.23	0.870570713153	–0.6538	7.247	2.442
1.620	0.6923712291321	1.6641117871	0.582501	7.983985	11.884	90.2	0.870276064882	–0.6527	7.249	2.437
1.625	0.6919270549536	1.6506563793	0.586932	7.876586	9.909	58.4	0.869983948407	–0.6516	7.238	2.431
1.630	0.6914869129943	1.6374579081	0.591292	7.771432	8.575	37.4	0.869694328857	–0.6506	7.220	2.426
1.635	0.6910507423786	1.6245094326	0.595584	7.668458	7.612	22.7	0.869407172067	–0.6495	7.199	2.420
1.640	0.6906184835879	1.6118042538	0.599808	7.56760	6.881	11.8	0.869122444566	–0.6484	7.177	2.415
1.645	0.6901900784197	1.5993359036	0.603967	7.46880	6.307	3.5	0.868840113553	–0.6473	7.152	2.410
1.650	0.6897654699484	1.5870981359	0.608061	7.37200	5.843	–2.9	0.868560146882	–0.6462	7.126	2.404
1.655	0.6893446024878	1.5750849167	0.612092	7.27715	5.4596	–8.0	0.868282513041	–0.6451	7.101	2.399
1.660	0.6889274215546	1.5632904154	0.616063	7.18418	5.1363	–12.1	0.868007181137	–0.6441	7.076	2.394
1.665	0.6885138738334	1.5517089968	0.619973	7.09306	4.8597	–15.5	0.867734120880	–0.6430	7.049	2.389
1.667	0.6883740859496	1.5478188813	0.621289	7.06248	4.774	–16.5	0.867641792579	–0.6426	7.042	2.387

Bibliography

[1] C. E. Willert and M. Gharib. Three-dimensional particle imaging with a single camera. *Experiments in Fluids*, 12:353–358, 1992.

[2] H.-G. Maas, A. Gruen, and D. Papantoniou. Particle tracking velocimetry in three-dimensional flows. *Experiments in Fluids*, 15:133–146, 1993.

[3] F. Pereira, M. Gharib, D. Dabiri, and D. Modarress. Defocusing digital particle image velocimetry: a 3-component 3-dimensional DPIV measurement technique. application to bubbly flows. *Experiments in Fluids*, Supplement:S78–S84, 2000.

[4] R. N. Kieft, K. R. A. M. Schreel, G. A. J. van der Plas, and C. C. M. Rindt. The application of a 3D PTV algorithm to a mixed convection flow. *Experiments in Fluids*, 33:603–611, 2002.

[5] N. F. Ponchaut, C. A. Mouton, and H. G. Hornung. Development of three-dimensional particle tracking velocimetry for supersonic flow. In *42nd AIAA Aerospace Sciences Meeting*, Reno, NV, 2004.

[6] N. Nishino, N. Kasagi, and M. Hirata. Three-dimensional particle tracking velocimetry based on automated digital image processing. *ASME, Journal of Fluids Engineering*, 111:384–391, 1989.

[7] Y. Suzuki and N. Kasagi. Turbulent air-flow measurement with the aid of 3-D particle tracking velocimetry in a curved square bend. *Flow, Turbulence and Combustion*, 63:415–442, 1999.

[8] Y. Pu, X. Song, and H. Meng. Off-axis holographic particle image velocimetry for diagnosing particulate flows. *Experiments in Fluids*, Suppl.:S117–S128, 2000.

[9] H. Meng, G. Pan, and S. H. Woodward. Holographic particle image velocimetry: from film to digital recording. *Measurement Science and Technology*, 15:673–685, 2004.

[10] F. Pereira and M. Gharib. Defocusing digital particle image velocimetry and the three-dimensional characterization of two-phase flows. *Measurement Science and Technology*, 13:683–694, 2002.

[11] N. F. Ponchaut, C. A. Mouton, H. G. Hornung, and D. Dabiri. 3D particle tracking velocimetry method: Advances and error analysis. *Measurement Science and Technology*, 2005.

[12] H. Stüer, H.-G. Maas, M. Virant, and J. Becker. A volumetric 3D measurement tool for velocity field diagnostics in microgravity experiments. *Measurement Science and Technology*, 10:904–913, 1999.

[13] S. Murai, H. Nakamura, and Y. Suzuki. Analytical orientation for non-metric camera in the application to terrestrial photogrammetry. In *International Archives of Photogrammetry XXIII, Commision V*, pages 516–525, 1980.

[14] H.-B. Kim and S.-J. Lee. Performance improvement of two-frame particle tracking velocimetry using a hybrid scheme. *Measurement Science and Technology*, 13:573–582, 2002.

[15] N. A. Malik, T. Dracos, and D. A. Papantoniou. Particle tracking velocimetry in three-dimensional flows. Part II: particle tracking. *Experiments in Fluids*, 15:279–294, 1993.

[16] J. Willneff. 3D particle tracking velocimetry based on image and object space information. In *ISPRS Commission V Symposium*, Korfu, Greece, 2002.

[17] L. Kajitani and D. Dabiri. A full three-dimensional characterization of defocusing digital particle image velocimetry. *Measurement Science and Technology*, 16:790–804, 2005.

[18] D. C. Lay. *Linear Algebra and its Applications*. Addison Wesley, second edition, 1997.

[19] G. Guderley. Starke kugelige und zylindrische verdichtungsstöße in der nähe des kugelmittelpunktes bzw. der zylinderachse. *Luftfahrtforschung*, 19:302–312, 1942.

[20] P. Hafner. Strong convergent shock waves near the center of convergence: a power series solution. *Siam Journal of Applied Mathematics*, 48(6):1244–1261, 1988.

[21] W. Chester. The quasi-cylindrical shock tube. *Philosophical Magazine*, 45:1293–1301, 1954.

[22] R. F. Chisnell. The normal motion of a shock wave through a nonuniform one-dimensional medium. *Proceedings of the Royal Society (London)*, 232:350–370, 1955.

[23] G. B. Whitham. On the propagation of shock waves through regions of non-uniform area or flow. *Journal of Fluid Mechanics*, 4:337–360, 1958.

[24] R. F. Chisnell. An analytic description of converging shock waves. *Journal of Fluid Mechanics*, 354:357–375, 1998.

[25] B. H. K. Lee. Nonuniform propagation of imploding shocks and detonations. *AIAA Journal*, 5(11):1997–2003, 1997.

[26] J. J. Quirk. Amrita – a computational facility (for CFD modeling). In *VKI 29th CFD Lecture Series ISSN 0377-8312*, 1998.

[27] R. B. Payne. A numerical method for a converging cylindrical shock. *Journal of Fluid Mechanics*, 2:185–200, 1957.